2013

THE DESIGN AND VALIDATION OF A COMPUTATIONAL MODEL OF THE HUMAN WRIST JOINT

Afsarul Mir
Virginia Commonwealth University

THE DESIGN AND VALIDATION OF A COMPUTATIONAL MODEL OF THE HUMAN WRIST JOINT

A Thesis submitted in partial fulfillment of the requirements for the degree of Master of Science at Virginia Commonwealth University.

by

AFSARUL QUDDUS MIR
B.S., Virginia Commonwealth University, 2009

Director: Jennifer S. Wayne, Ph.D.
Departments of Biomedical Engineering and Orthopaedic Surgery

Virginia Commonwealth University
Richmond, Virginia
May, 2013

Acknowledgement

Looking back at my academic career at VCU, there a number of people that I would like to acknowledge and thank for all their help and support.

First and foremost, I would like to express my sincerest gratitude to my advisor and mentor, Dr. Jennifer Wayne. Starting from my undergraduate years at VCU and all through my graduate work, you have provided the support and guidance that has been critical in my academic and professional success. Your guidance has always forced me to reach above and beyond in everything that I do. Your input and insight has been invaluable for all the work that I have conducted in the Orthopaedics Research Laboratory. Working for you in various manners over the past six years has been an honor and I am very grateful for all the opportunities you have provided. Much of my professional growth has occurred under your care and I will carry those lessons with me through the rest of my life.

I would also like to thank Dr. Gerald Miller and Dr. Jonathan Isaacs for taking the time to serve on my thesis advisory committee. I greatly appreciate all the comments and feedback you have provided throughout the various stages of my work.

Next, I would like to extend my thanks to all my friends and peers that I have worked with while completing my graduate work. Meade, Sean, Ruchi, Johnny, Erika and Casey, thank you for all your support. You have made my time in the lab much more memorable. And a very special thanks to Meade and Ruchi, for all your help, advice and support throughout my thesis work. Without the two of you, things would have been much more difficult.

And finally, I would like to thank my family, without them I would not be here today. To my little brother, Sayem, it has been a privilege being your older brother and you have brought great joy to me with all your quirky ways. To my older brother, Ceasar, you have been beside me every step of my life. Thank you for always “having my back” and supporting me every single day. And to my mother, Mohsina, you have been the source of my drive. Even from afar, you have been my inspiration and reassurance when things got tough. Thank you for all your love and support.

Table of Contents

Page

LIST OF TABLES

Page

LIST OF FIGURES

Page

LIST OF ABBREVIATIONS

2D	Two-Dimensional
3D	Three-Dimensional
APL	Abductor Pollicis Longus
CAD	Computer-Aided Design
CH	Capitohamate Interosseous Ligament
CT	Capitotrapezoidal Interosseous Ligament
CT	Computed Topography
DIC	Dorsal Intercarpal Ligament
DICOM	Digital Imaging and Communications in Medicine
DRC	Dorsal Radiocarpal Ligament
ECRB	Extensor Carpi Radialis Brevis
ECRL	Extensor Carpi Radialis Longus
ECU	Extensor Carpi Ulnaris
ER	Extensor Retinaculum
FCR	Flexor Carpi Radialis
FCU	Flexor Carpi Ulnaris
FEA	Finite Element Analysis
FR	Flexor Retinaculum
HU	Hounsfield Units
ISB	International Society of Biomechanics
LRL	Long Radiolunate Ligament

LT	Lunotriquetral Interosseous Ligament
PH	Pisohamate Ligament
PRC	Proximal Row Carpectomy
PT	Pisotriquetral Interosseous Ligament
RBM	Rigid Body Modeling
RC	Radiocapitate Ligament
RS	Radioscaphoid Ligament
RSC	Radioscaphocapitate Ligament
RSL	Radioscapholunate
SC	Scaphocapitate Ligament
SL	Schapholunate Interosseous Ligament
SRL	Short Radiolunate Ligament
STL	Stereolithographic
STT	Scaphotrapeziotrapezoidal Ligament
TC	Triquetrocapitate Ligament
TCL	Transverse Carpal Ligament
TFCC	Triangular Fibrocartilage Complex
TH	Triquetrohamate Ligament
TT	Trapeziotrapezoidal Interosseous Ligament
UC	Ulnocapitate Ligament
UL	Ulnolunate Ligament
UT	Ulnotriquetrum Ligament

Abstract

THE DESIGN, DEVELOPMENT AND VALIDATION OF A COMPUTATIONAL MODEL OF THE HUMAN WRIST JOINT

By Afsarul Quddus Mir, B.S.

A Thesis submitted in partial fulfillment of the requirements for the degree of Master of Science in Biomedical Engineering at Virginia Commonwealth University

Virginia Commonwealth University, 2013

Major Director: Jennifer S. Wayne, Ph.D.
Professor, Biomedical Engineering & Orthopaedic Surgery
Director, Orthopaedic Research Laboratory

Advancements in computational capabilities have allowed researchers to turn towards modeling as an efficient tool to replicate and predict outcomes of complex systems. Computational models of the musculoskeletal system have gone through various iterations with early versions employing dramatic simplifications. In this work, a three-dimensional computational model of the wrist joint was developed. It accurately recreated the skeletal structures of the hand and wrist and represented the constraints imposed by soft tissue structures like ligaments, tendons, and other surrounding tissues. It was developed to function as a tool to

investigate the biomechanical contributions of structures and the kinematic response of the wrist joint.

The model was created with the use of a commercially available computer-aided design software employing the rigid body modeling methodology. It was validated against three different cadaveric experimental studies which investigated changes in biomechanical response following radioscapholunate fusion and proximal row carpectomy procedures. The kinematic simulations performed by the model demonstrated quantitatively accurate responses for the range of motions for both surgical procedures. It also provided some understanding to the trends in carpal bone contact force changes observed in surgically altered specimens. The model provided additional insight into the importance of structures like the triangular fibrocartilage and the capsular retinacular structures, both of which are currently not very well understood. As better understanding of components of the wrist joint is achieved, this model could function as an important tool in preoperative planning and generating individualized treatment regiments.

CHAPTER 1: INTRODUCTION

1.1 OVERVIEW OF MUSCULOSKELETAL TESTING

1.1.1 Musculoskeletal Testing Methods

The musculoskeletal system is a complex system of different anatomical structures working together to allow locomotion, support and stability of the human body. The main structures involved are the bones, cartilage, muscles, ligaments, tendons and other soft connective tissues. Diarthrodial joints allow for large range controlled motion and are responsible for the body's mobility and dexterity. Injuries and degenerative diseases to the musculoskeletal system can have a great effect on the quality of life of an individual. Thus, numerous studies have been conducted to understand the function of a normal, healthy joint and the effect of injuries or diseases on its function.

Researchers employ three main methods to study and understand the function and behavior of musculoskeletal joints. The first method is through clinical studies, which involves patients undergoing interventions or corrective procedures to determine the ultimate effect and benefits. This method has the advantage of testing on native living tissue, accounting for healing, and providing the true outcome. Among disadvantages, the main issue lies in the difficulty to determine the changes occurring in individual components of the joint. Additionally, patient response is highly varied, there is very limited control over parameters, tends to be very expensive, and it only allows for a very superficial understanding of the outcome.

The second method of investigation is experimental studies. In this method, researchers aim to replicate living tissue by testing cadaveric specimens and/or implementing mechanical

simulators. Testing can be conducted under controlled conditions with the application of improvements and restrictions on the specimen to determine the outcome. This method has the advantage of permitting control over forces, motions as well as other parameters. However, this method has similar disadvantages as clinical studies. Not all parameters can be accurately measured or controlled and the process tends to be quite expensive and time consuming. Furthermore, the degradation of the tissue may lead to inaccurate results. During experimental studies, mechanical instruments are sometimes implemented to measure parameters. Hardware like transducers or pressure sensitive films may further disrupt the integrity and natural response of the joint.

With the advances in computational technology in the last several decades, researchers are employing modeling to study the complexities of human musculoskeletal joints. Computational modeling allows for an efficient means to replicate a complex system. This can be done by utilizing known properties of tissue, conducting tests under very controlled parameters, accurately measuring results, and efficiently replicating tests on identically modeled tissue. Modeling can also help identify effects resulting from changes to specific parameters or structures. Overall, computational modeling can be a cost effective means of conducting a study without a large sample as required for clinical trials. The main drawback lies in the formulation of the model itself. This is highly reliant on our knowledge of native tissue behavior and the modelers' ability to recreate this in silico. Additionally, due to computational limitations, every functional component of a joint may not be incorporated. Thus simplifications and assumptions are implemented that may potentially affect accuracy.

Once computational models have been validated, these have a great potential to be used as a tool to understand the function and components of a joint. Models can also be used to

understand the functional effects of pathologies and trauma and to determine the outcomes of new surgical techniques. This tool can also potentially be used for pre-operative planning for complex surgeries to determine the optimum procedure. As a post operatively analysis tool, it can also help with rehabilitation for uncommon and unique surgical techniques.

1.2 COMPUTATIONAL MODELING OF MUSCULOSKELETAL SYSTEMS

1.2.1 Types of Modeling

In the study of musculoskeletal joints, computational modeling methods have generally fallen under two categories: finite element analysis (FEA) and rigid body modeling (RBM). Both of these techniques result in different types of information. Traditionally, FEA is conducted to determine the stress and strain distribution of materials under static loading conditions. On the other hand, RBM is more effective in studying dynamic multi-body systems to determine responses due to perturbations.

1.2.2 Finite Element Analysis

FEA is an efficient numerical technique for approximating solutions to a variety of engineering and physics problems in one, two, three or four-dimensions. It is a powerful tool to evaluate stresses in structures with highly irregular shapes, materials and loading behavior. Within the literature, a large number of FEA studies exist that examine the function and pathologies in a variety of joints like the shoulder, knee, spine, wrist, foot, elbow and hip, as well as in individual bones. Due to the nature and complexity of the wrist joint, FEA can be challenging to conduct. However, researchers have used FEA to look at stress distribution and

load transmission through the normal wrist, [1–4] traumatized wrist [3], [5–9], and wrists with corrective surgical procedures [10], [11].

During FEA modeling, a complex domain is subdivided into smaller elements. These elements have defined physical properties and dimensions. The reaction of each individual element to an applied load or perturbation can be used to approximate the overall behavior of the entire domain. In orthopaedics, FEA has been used to study and understand normal bones, joints and the effects of degeneration and trauma. It has also been used to design and enhance implants and other medical devices. This technique has permitted researchers to determine the stress and strain distributions, load transfers, fractures and failures from forces experienced by musculoskeletal structures.

Even with its strengths and advantages, FEA does have limitations. This method is highly reliant on the material properties (density, Young's modulus, shear modulus, Poisson's ratio, etc) that are defined by the user. For biological tissue, such properties can be difficult to determine and are highly variable between structures as well as regions within the same structure. In most cases, artificial constraints must be imposed to allow the system to solve. Additionally, this method of analysis may also take extensive time to compute due to the fine meshes formed by replicating complex structures. Thus, FEA is not as useful of a tool to study kinematics or dynamic function in biomechanics.

1.2.3 Rigid Body Modeling

RBM consists of representing a body as a solid, inelastic, incompressible structure. Such an assumption can be made in cases where the material being studied has a high stiffness and would require very high stresses to cause more than 1% total strain. [12] This method of

modeling is governed by the assumption that the structures are undeformable and impenetrable at the contact interfaces and are only bound by the constraining forces or defined boundary conditions.

In RBM modeling, the bones are modeled as solid bodies, while ligaments, tendons, cartilage and other soft tissues are modeled as spring elements. These spring elements can be defined as linear/nonlinear, tension/compression only, or both depending on the native tissue characteristics or function being replicated. With these models, the kinematic response of the joint is primarily dependent on the contact surfaces between the bodies and the restrictions imposed by the spring elements.

Numerous studies have been conducted that apply the RBM method to musculoskeletal joints. This method's strength lies in determining kinematics and effects of perturbations in a dynamic multi-body system in a time efficient manner.

One of the first weaknesses arises from the manner in which the user defines the soft tissues represented by the spring elements. While RBM requires fewer tissue mechanical properties, many of which can be obtained from simple mechanical testing, there is little consensus on the measured properties within the literature. In many cases, as with the wrist, some structures may be too small and difficult to test and determine its mechanical properties.

An additional issue with existing RBM methods is the accurate representation of the lines of action of soft tissue structures. Muscles and tendons have traditionally been represented as straight line force vectors between the anatomical origin and insertion point. With dynamic joints, this may not create an accurate representation of the tissue. As the bones in the joint move through their motion arc, the tendon may wrap around the bones and have a different moment arm for the muscle. In most modeling methods, a straight line vector would not be able

to accurately replicate wrapping or the muscular moment arm. In fact, the vector would most likely interfere and overlap the bones and be anatomically incorrect. This same effect can be seen in larger ligaments and capsular structures, which physiologically have both a tension and "wrapping" stabilization function on a joint. To mimic anatomically correct lines of action, additional measures may have to be implemented. These may include defining points to redirect lines of action or utilizing spherical/ cylindrical elements to recalculate moment arms through joint motion. [13] The use of the latter method can be difficult, time consuming, and may not always be effective for the purpose of a study.

For many existing musculoskeletal RBM models, complex joints have been oversimplified and modeled as ideal mechanical joints. For example, the elbow and knee joints have been modeled as hinges, and the shoulder has been modeled as a ball and socket joint [14] or as a three hinge joint. [15] These types of simplifications and assumptions do not realistically mimic true human joint function and may not lead to an effective predictive tool.

The first RBM for the musculoskeletal system was developed by Wismans et al for the human knee joint. [16] In this model, the bony articular surfaces were assumed to be rigid and force vectors represented the soft tissue structures. Subsequently, researchers began developing models embracing a similar methodology. Further development of the theory led to the capabilities such as measuring contact surface area and contact force generation. [17] These improvements have allowed for the formation of dynamic models, which have given researchers a tool for investigations.

For computational models to become an effective predictive tool for musculoskeletal joints, simulations should be solved in forward dynamic manner. This should entail minimal artificial limitations in the degrees of freedom of the joint. But primarily, kinematics and

function should be dictated by the contact surfaces between the bones and the soft tissue restraints.

1.2.4 Existing Wrist Rigid Body Models

The wrist is a complex structure comprised of multiple small bones and a large network of soft tissue structures. Due to this complexity, it has been difficult to create an effective model for this joint. There are a plethora of different studies that have employed wrist RBMs over the years. These were developed in an iterative manner with early studies employing very dramatic simplifications. More effective models were developed as computational capabilities become more sophisticated.

Early studies that have modeled the wrist were two-dimensional (2D) reductions for simplification purposes. These studies employed a similar methodology of modeling bones as rigid structures and soft tissues as spring elements. The first RBM modeling of the wrist was conducted by Horii et al. [10] This study analyzed a simplified 2D articulating wrist model to look at changes in force transmission through the carpus with different surgical procedures to treat Kienbock's disease. For this test, a simulated grip loading maneuver was imposed on the carpus. This involved application of an axial load along the long axis of the metacarpal bones. Similar studies have been conducted by Schuind et al [18] and Manal et al [19] with 2D wrist models. In the study by Schuind et al, force and pressure transmission through normal healthy adult wrists were examined during simulated static grip loading. In addition, to the elimination of the third dimension, these models were further simplified by representing the trapezium and trapezoid bones as one unit and with the exclusion of the pisiform.

Manal et al designed a model with similar methodology and simplifications, but improved the 2D approach by employing a unique method of representing cartilage. Cartilage tissue was represented as spring elements, which were repositioned during simulations such that fewer elements failed due to off-center loading. [19] This model examined the force transmission through juvenile idiopathic arthritic wrists. A similar 2D RBM model validation study was conducted by Ide on the metacarpophalangeal joint.

The first three-dimensional (3D) RBM wrist model was developed by Iwasaki et al [20] to explore the biomechanical effects of different limited intercarpal fusions for the treatment of Kienbock's disease. This study looked at three different operative procedures and examined the post-operative unloading on the lunate bone and changes in carpus force transmission. The model employed the same methodology discussed in the 2D models above to represent bones, ligaments and cartilage. A similar grip loading maneuver was also applied to the model. A similar 3D RBM study conducted by Genda et al [21] examined two different positions of healthy wrists: the neutral position and a patient selected functional grasping position. Models were formulated from these two positions and the force transmission changes through the carpus were determined from a grip loading maneuver. Additional studies looked at force transmission changes within the carpus between neutral position and full extension of the wrist, [22] and with scaphoid non-union and distal fragment resection. [23]

Fischli et al developed a 3D RBM model designed to predict carpal bone motion and wrist kinematics. [24] The model was used to simulate motions in wrist extension, radial and ulnar deviation; however wrist flexion was not reported. While this model did provide kinematic data on the wrist and carpal bones, some significant simplifications were implemented that affected the results of the study. The five metacarpal bones were fused to the distal carpal row

and the pisiform was fused to the triquetrum. Functionally, it has been shown that there is little to no motion between the third metacarpal and the capitate, [25] and thus fusion of these two bones may be justified. However, there is significant motion observed between the remaining bones in the carpometacarpal joint. [26] Additionally, the pisiform has been described as a sesamoid bone that transmits forces from the FCU to the triquetrum, hamate and the fifth metacarpal bone. [27–29] Fusion of the piso-triquetral joint will predictably have a significant impact in this force transmission. This study was also modeled in an inverse dynamic fashion, such that muscular forces were prescribed to match end point positions obtained from radiographic scans. While this may provide some information regarding individual components in different wrist positions, this cannot be used as a predictive tool to determine joint response.

The 3D RBM developed by Majors et al [30] does not constrain the wrist's degrees of freedom, nor restrict the model to testing in a static or neutral position. It also does not impose any sort of bone fusion for simplification purposes. Following the standard RBM methodology, all the bones were modeled as rigid bodies, the ligaments were represented as tension only spring elements and muscles as force vectors. The study examined the changes in wrist kinematics after a carpal fusion procedure and carpal bone excision. In this case, a forward dynamic solution method was employed.

Even though this model did not employ any of the simplifications implemented by previous wrist models, it still had some shortcomings. The model itself did not incorporate some essential soft tissue structures that are part of this complex joint system. The triangular fibrocartilaginous complex (TFCC) is a structure that contributes to ulnar side stability and force transmission. [31] The retinacular structures that encompass the entire joint also play an

important role of stabilization. Since these structures are important in normal wrist function, their incorporation may be quite important in accurately replicating wrist kinematics.

1.3 OBJECTIVES

It is the objective of this thesis to design, develop and validate a three-dimensional computational model of the human wrist joint. The model will allow the investigation of the joint's overall biomechanical function and the individual contributions of structures in the kinematic response of the wrist. A rigid body model will be created through the use of SolidWorks, a commercially available computer-aided design (CAD) program. Rigid body modeling simulation will be conducted within SolidWorks Motion, a native SolidWorks add-in, which implements the ADAMS modeling package. The model will be created by accurately rendering the bony structures in the wrist, replicating bony contact, and applying constraints via ligamentous and other soft tissue structures. Kinematic motion will be achieved by applying forces to relevant muscle tendons. This model will overcome simplifications reported by previous models where multiple bones were considered to function as one unit or were eliminated from the design space. It will also be able to achieve motions in all three dimensions. Additionally, the human wrist joint is comprised of a large number of soft tissue structures that have been previously disregarded. These soft tissue structures will be further investigated and incorporated during the development of this model. The model will be validated against the results of two cadaveric studies looking at the effect of surgical techniques on wrist kinematics. [32–34] This work expands on the wrist joint model developed by B. Majors and J. Wayne. [30] Ultimately, this model is being developed in an effort to be used as a clinical and experimental tool to predict and analyze the outcome of wrist pathology and surgery.

CHAPTER 2: WRIST ANATOMY

The wrist is one of the most complex joints in the human body. Traditionally, it has been discussed as a single joint, yet in actuality it is a compound structure that consists of four different joints. This multi-jointed structure gives the hand its high degrees of freedom, large range of motions, decreases structural pinch experienced at extremes and its ability to form a flat joint surface. [35] Overall, the wrist is a highly dexterous structure essential in everyday activities and in leading a healthy and regular lifestyle.

The wrist is considered a biaxial joint with the major motions occurring in flexion and extension around the coronal axis, and radial and ulnar deviation around the anteroposterior axis (Figure 2-1). Some pronation and supination may also be observed at the radiocarpal joint. However, most of the pronation and supination positions of the hand come from forearm rotation. In some extreme cases, it has been observed that joint incongruence and ligamentous laxity may allow up to 45^{o} of combined passive pronation and supination at the radiocarpal and midcarpal joints. [35] However, this motion is not usually considered to be an additional degree of freedom for the wrist complex.

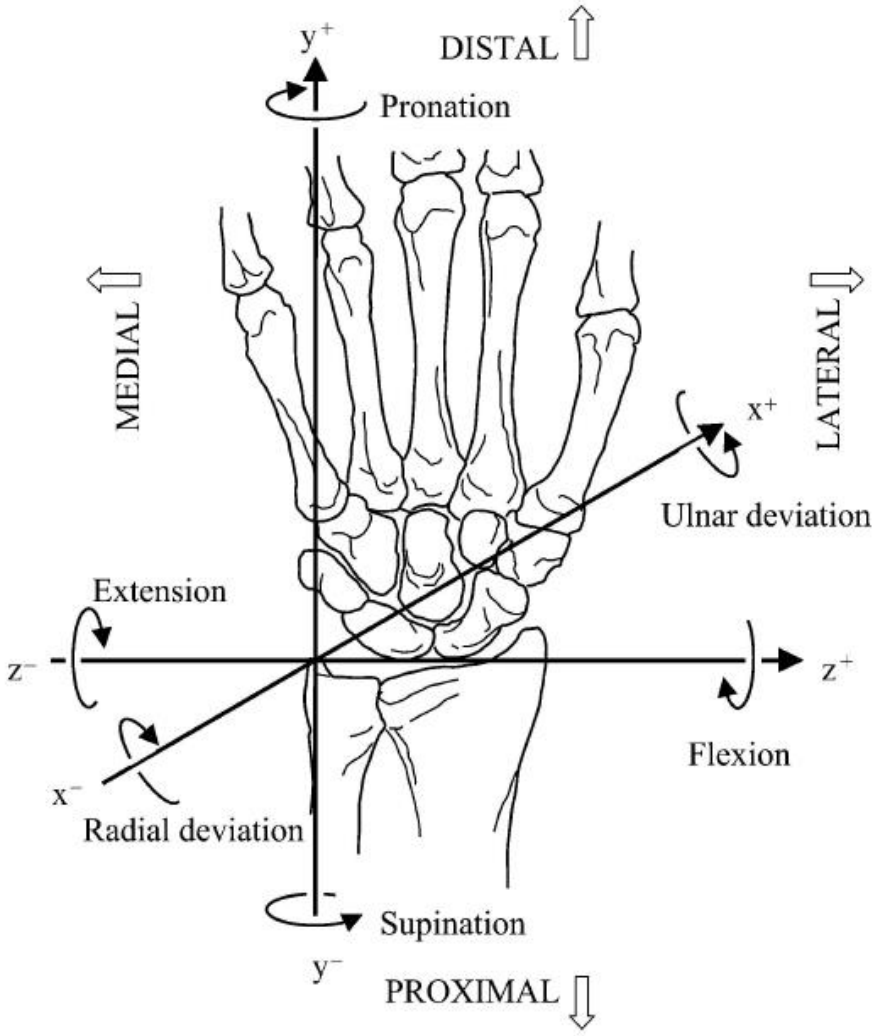

Figure 2-1: Anatomical regions and wrist motions around the indicated axes (palmar view of the right wrist). [36]

2.1 SKELETAL ANATOMY

The wrist and hand are made up of the two long bones of the forearm, the eight carpal bones of the wrist and the five metacarpal bones of the hand (Figure 2.1-1). The eight carpal bones are arranged into two carpal rows: the proximal carpal row and the distal carpal row. The proximal carpal row is comprised of the scaphoid, lunate, triquetrum and pisiform. The distal carpal row is formed by the trapezium, trapezoid, capitate and hamate. Functionally, the distal carpal row is a strongly bound group of bones. The proximal carpal row bones are found to be much less constrained and allow significant motion between the individual bones. [35], [37]

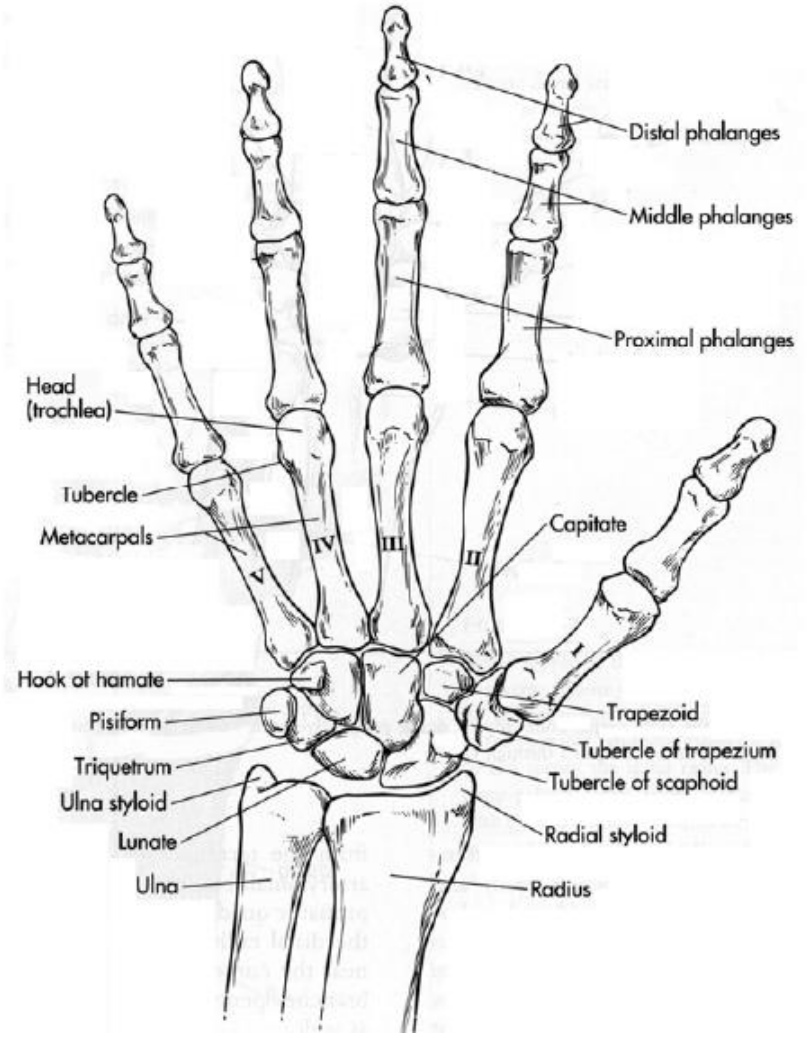

Figure 2.1-1: Skeletal anatomy of the wrist and hand (palmar view of the right wrist). [38]

As previously mentioned, the wrist is made up of four joints: radio-ulnar joint, radiocarpal joint, midcarpal joint, and carpometacarpal joint (Figure 2.1-2). In combination, these four joints provide the full range of motions of this versatile structure. Starting from the proximal end, the radioulnar joint is formed by the distal interaction between the radius and ulna. The radiocarpal joint is formed by the articulations of the radius and ulna with the proximal carpal row. The midcarpal joint is created between the proximal carpal row and the distal carpal row. And most distally, the carpometacarpal joint forms from the articulations between the distal carpal row and the five metacarpals of the hand.

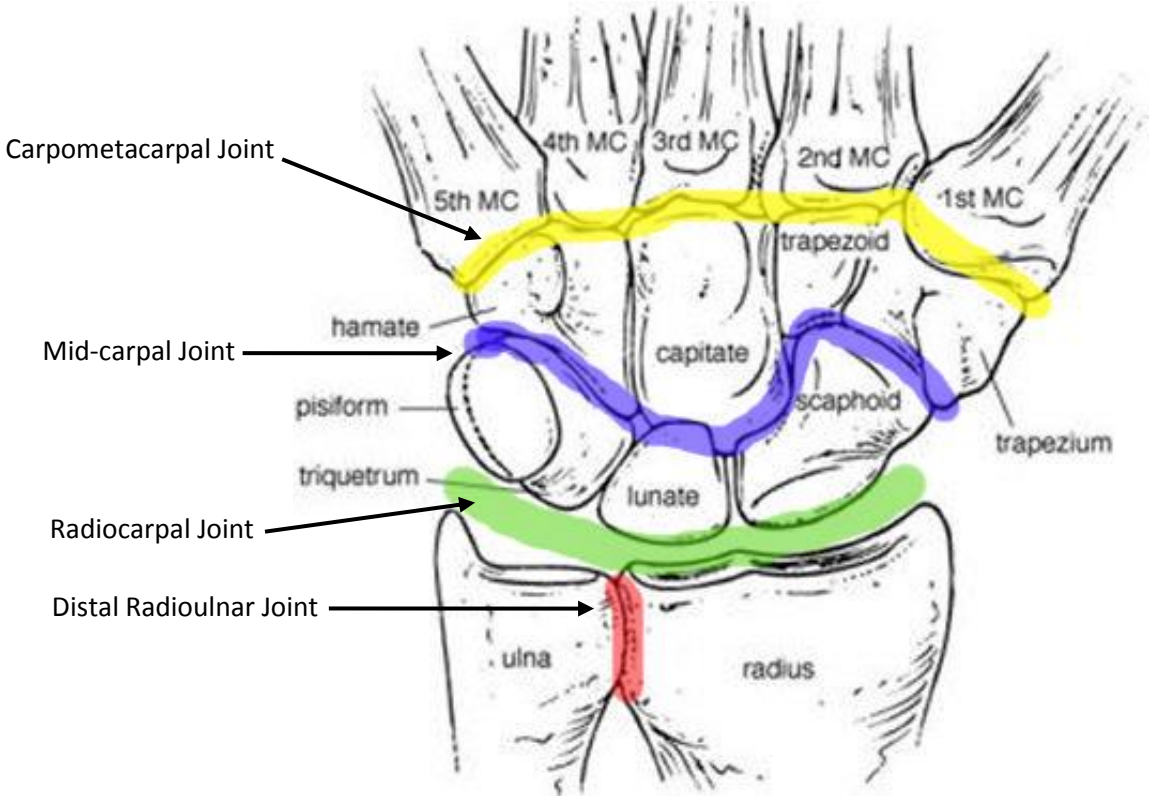

<u>Figure 2.1-2</u>: The joints of the wrist (palmar view of the right wrist).

At the distal radioulnar joint, the ulnar head articulates with the radius at the radial ulnar notch. The triangular fibrocartilage complex (TFCC) is a soft tissue structure that sits atop the

ulnar head and is attached to the radius via the dorsal and palmar radioulnar ligaments. Along with these ligaments, the TFCC is a critical structure in providing distal radioulnar joint stability. [39], [40]

At the radiocarpal joint, the scaphoid exclusively articulates with the lateral radial facet, the lunate primarily articulates with the medial radial facet having some interactions with the TFCC and the triquetrum predominantly articulates with the TFCC. [35] A large portion of the total range of motion experienced by the wrist occurs at the radiocarpal joint. This is due to the bony articulations and the ligamentous structures that secure the scaphoid and the lunate. Due to a larger dynamic role, the bones of the radiocarpal joint experience large forces and are more prone to trauma and fractures.

As a part of the proximal row, the pisiform does not have any major articulating surfaces other than the relatively flat contact face with the triquetrum. The pisiform functions entirely as a sesamoid bone, presumably to increase the moment arm of the flexor carpi ulnaris (FCU) tendon. [35] It is also the only carpal bone with a tendinous insertion. The pisiform is embedded within the FCU tendon, but it also has ligamentous attachments with the triquetrum, hook of hamate and fifth metacarpal. Through these soft tissue attachments, it transmits muscular force from the FCU to the rest of the carpus. [28] Additionally, the pisiform acts as an attachment site for part of the flexor retinaculum and integrates with part of the TFCC and the extensor retinaculum. While there has been some early controversy regarding the attachment of the extensor retinaculum to the pisiform, it is now accepted that the soft tissue structure wraps around the medial aspect of the wrist and attaches to the ulnar styloid process, the triquetrum and the posterior medial margin of the pisiform. [28], [41] Thus, this small bone is a soft tissue attachment focal point on the ulnar aspect of the wrist. [28]

The midcarpal joint is formed by articulations of the proximal row and the distal carpal row. The bones of the distal carpal row (the trapezium, trapezoid, capitate and hamate) are tightly bound together through ligamentous structures. The hamate is a pyramidal shaped bone at the medial end of the distal row. From the palmar surface arises a hook like protrusion which acts as the medial wall of the carpal tunnel and as the attachment point for a few carpal ligaments. The capitate is the largest carpal bone and has been described as the center of the wrist. It articulates with three metacarpal bones and four carpal bones. Its proximal pole sits within the curved facets formed between the scaphoid and lunate and acts as the pivot point between the two carpal rows. The trapezoid and the trapezium line up on the lateral end of the distal row. Since the midcarpal joint does not form a continuous articular surface, it has been described as a functional joint rather than an anatomical joint. Additionally, the strong union between the bones within this row results in an almost equal load distribution across the three articulating surfaces between the joint. [35]

2.2 SOFT TISSUE ANATOMY

The kinematics and range of motion of the wrist joint complex is fully dependent on the interactions of the respective bones and the stabilizing soft tissue structures. It is dependent on the manner in which the ligaments secure the bones together, the motions permitted by the laxity of the ligaments, the articulating surfaces of the bones, the stabilizing effects of the capsular structures surrounding the joint and the constraining effects of the wrist muscles. [35]

2.2.1 Ligamentous Anatomy

The ligamentous structures are the most crucial elements in all joints, responsible for maintaining articular stability of the bones as well as guiding their motions. The wrist is composed of an elaborate network of ligaments. Many of these ligaments have been extensively studied and reported on within the literature. In early studies, there was much confusion with the definitions and nomenclature of the individual wrist ligaments. Currently there is a general consensus in the literature regarding the wrist ligaments' structure and function [29], [36], [42–45] some differences can still be seen which arise from anatomical variations within the population. The more numerous palmar ligaments are usually thicker and stronger. By comparison the dorsal ligaments are fewer and usually tend to be structurally thinner. [35]

Wrist ligaments can be classified into two groups: extrinsic and intrinsic ligaments. This classification is based upon two things: the attachment points of the ligament and the joint that the structure crosses. Extrinsic ligaments connect carpal bones to the radius, ulna or metacarpals while intrinsic ligaments interconnect the eight carpal bones.

Biomechanically, researchers have found that intrinsic ligaments tend to be stronger and less stiff as compared to extrinsic ligaments. [46] This makes intrinsic ligaments less prone to injuries. As the major stabilizers of the carpal bones, this ability better protects the integrity of the complete carpus as a functional unit. It is theorized that one of the main reasons the intrinsic ligaments are able to prevent injury is due to their positioning within a synovial capsule. Thus, it seems that the extrinsic ligaments protect the intrinsic ligaments by being the primary receiver of loads and forces that lead to injury. [46] The intrinsic ligaments tend to heal slower since they rely upon the synovial fluid for nutrition rather than vascularized tissues as in extrinsic

ligaments. [35], [46] Thus, even though extrinsic ligaments are more likely to experience failure, they tend to have a better potential for overall healing.

Extrinsic Ligaments

Extrinsic ligaments are ligaments that have an attachment point outside of the carpus and can span across the radiocarpal joint or both the radiocarpal joint and mid carpal joint. On the palmar aspect, the ligaments can be further subdivided into palmar radiocarpal ligaments and ulnocarpal ligaments.

The palmar radiocarpal ligaments are composed of three distinct soft tissue structures that attach somewhat continuously along the palmar rim of the radius. Starting radially, these bands are the radioscaphocapitate ligament (RSC), inserting partially on the scaphoid and ending on the front notch of the capitate, the long radiolunate (LRL) ligament and the short radiolunate (SRL) ligament, both of which have attachment points along the lunate bone (Figure 2.2-1). A fourth band, the radioscapholunate ligament, used to be considered part of this group of ligaments. However, both anatomical and histological studies have shown that it is not a true ligament. This structure has been found to contain neurovascular structures originating from the palmar carpal branch of the radial artery and anterior interosseous artery and nerve. [47] Biomechanical studies have also found that the radioscapholunate structure has minimal supporting contributions to the carpal bones. [48]

The ulnocarpal ligaments are comprised of the ulnolunate (UL) ligament, the ulnotriquetral (UT) ligament, the ulnocapitate (UC) ligament, and the ulnar collateral ligament which includes parts of the meniscus homologue of the TFCC. On the dorsal aspect, there is only one extrinsic ligament, the dorsal radiocarpal (DRC) ligament. This is a wide ligament

arising from the dorsal rim of the radius and inserts into the dorsal rim of the triquetrum (Figure 2.2-2).

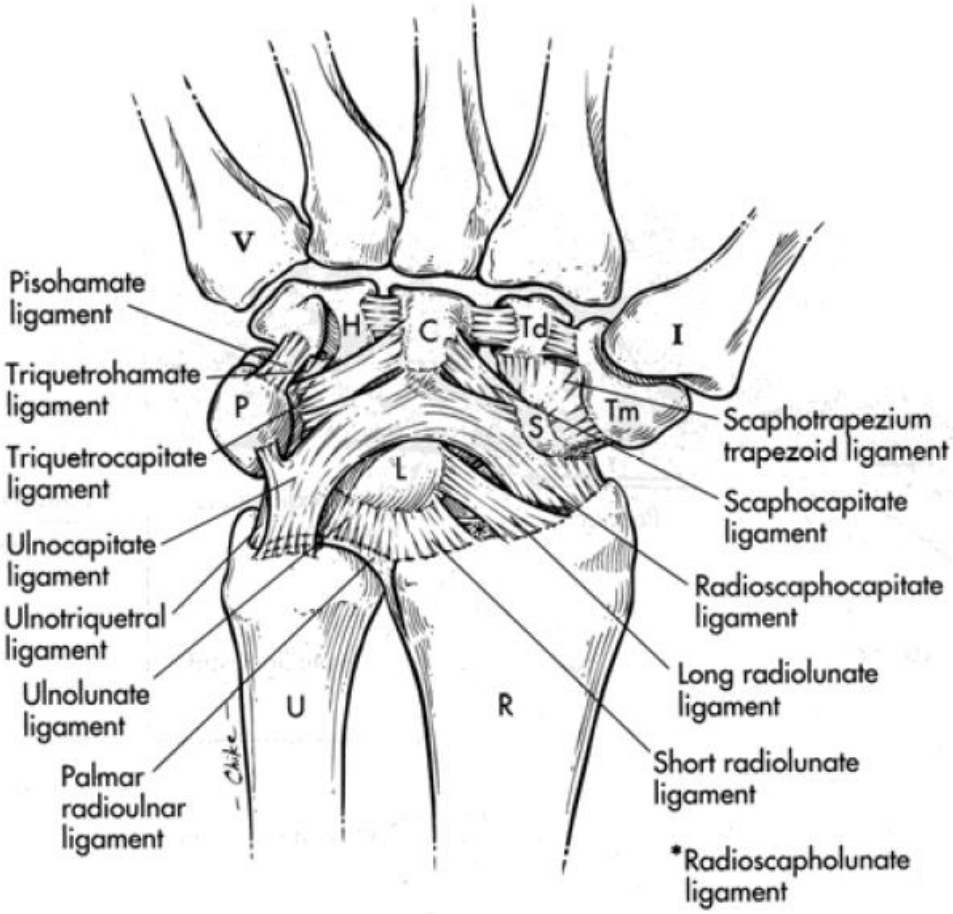

<u>Figure 2.2-1</u>: Palmar ligaments of the wrist. [38]

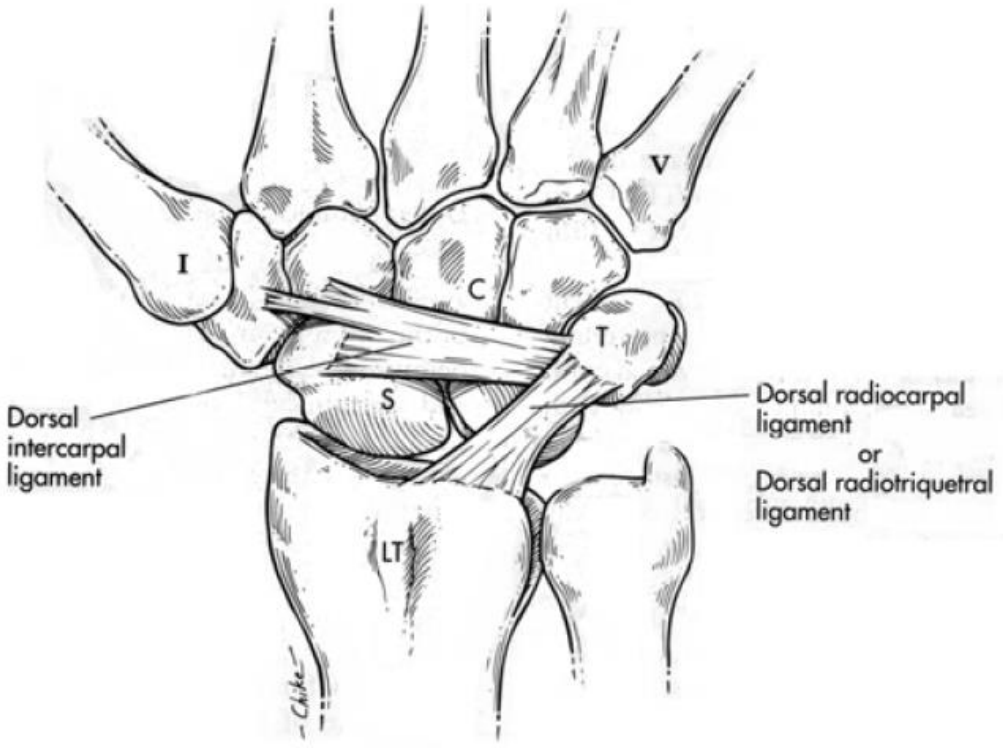

Figure 2.2-2: Dorsal ligaments of the wrist. [38]

Intrinsic Ligaments

The intrinsic ligaments are considered to be the most important stabilizers of the carpal bones. The interosseous ligaments do not span the mid-carpal joint, but attach to carpal bones within each row. The most highly studied of these is the scapholunate (SL) interosseous ligament. This ligament has been attributed to being a key factor in scaphoid stability. It is comprised of three bands that wrap around in a C shaped manner along the articulating surfaces of the scaphoid and lunate. The proximal row also contains the lunotriquetral (LT) ligament and the pisotriquetral ligament (PT). In the distal row, there are three interosseous ligaments; the trapeziotrapezoidal (TT) ligament, the capitotrapezoid (CT) ligament and the capitohamate (CH)

ligament (Figure 2.2-3 and Figure 2.2-4). All three of these ligaments have dorsal and palmar regions. The interosseous ligaments of the distal row play a major role in strongly binding these bones together, ensuring minimal motion between them and thus functionally acting as one unit.

Apart from the interosseous ligaments, the wrist joint also contains a few intrinsic ligaments that span across the midcarpal joint. On the palmar aspect, from the radial side, there is the scaphotrapiziotrapezoid (STT) ligament, the scaphocapitate (SC) ligament, the triquetrocapitate (TC) ligament, the triquetrohamate (TH) ligament and the pisohamate (PH) ligament (Figure 2.2-3 and Figure 2.2-4).

The dorsal intercarpal (DIC) ligament (Figure 2.2-2) is the only intrinsic ligament on the dorsal aspect of the wrist. This structure originates on the triquetrum from same attachment point as the DRC and courses horizontally to the trapezium. Some anatomical studies have also shown some fibers of the DIC not only attach laterally to the trapezium, but also to the scaphoid and the trapezoid and capitate. [49]

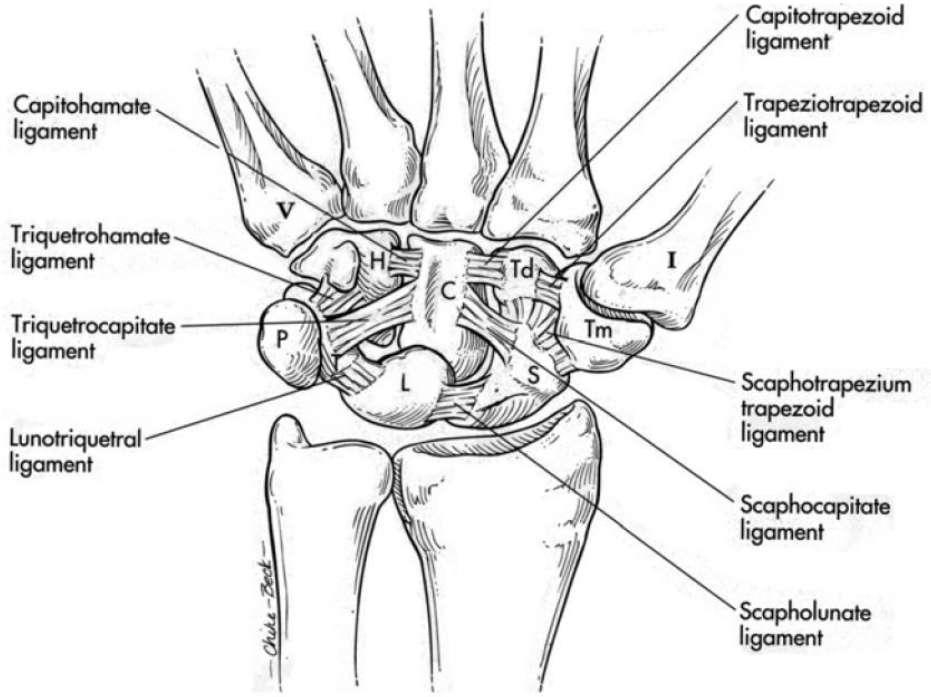

Figure 2.2-3: Palmar intrinsic ligaments of the wrist. [38]

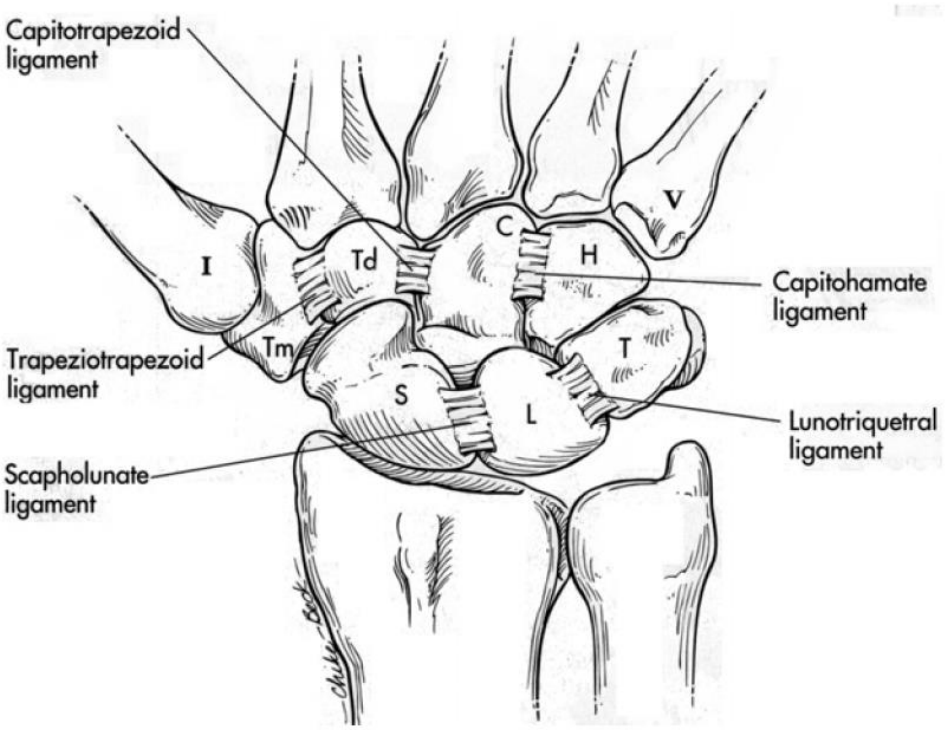

Figure 2.2-4: Dorsal intrinsic ligaments of the wrist. [38]

2.2.2 Triangular Fibrocartilage Complex

The triangular fibrocartilage complex (TFCC) is a structure formed from the combination of the dorsal and palmar radioulnar ligaments, ulnocarpal meniscus homologue, the triangular fibrocartilage, the sheath of the ECU, and ulnar collateral ligament (Figure 2.2-5 – Figure 2.2-7). [40], [50] The fibrocartilaginous articular disc of the TFCC can be considered as an extension of the articulating surface of the distal radius. This provides a smooth semi-continuous articulating surface for the proximal carpal row. However, the disc itself does not have a strong attachment to the radius. It is connected directly to the radial surface via weak soft tissue fibers. The structure's main support arises from its dorsal and palmar integration with the radioulnar ligaments. [50] Anatomically, the outer edges of the articular disc are thickened due to this integration with these thick and strong ligaments. Conversely, the central region of the articular disc tends to be shallow. [51], [52]

From the ulnar aspect, the disc is secured via two dense, fibrous connective tissue layers: the upper and lower lamina. The upper lamina, along with the radioulnar ligaments, attach to the ulnar head and styloid process. The lower lamina connects, through its fibers, with the ECU sheath as well as the triquetrum, hamate and the fifth metacarpal, forming part of the ulnar collateral ligament. The meniscus homologue is a region of irregular connective tissue that is part of the lower lamina and traverses palmarly and ulnarly to attach to the triquetrum. Overall, the triangular fibrocartilage complex should be considered to function as a medial extension of the distal radial surface, providing an even and continuous articulating surface for the carpal bones of the joint. [35], [52]

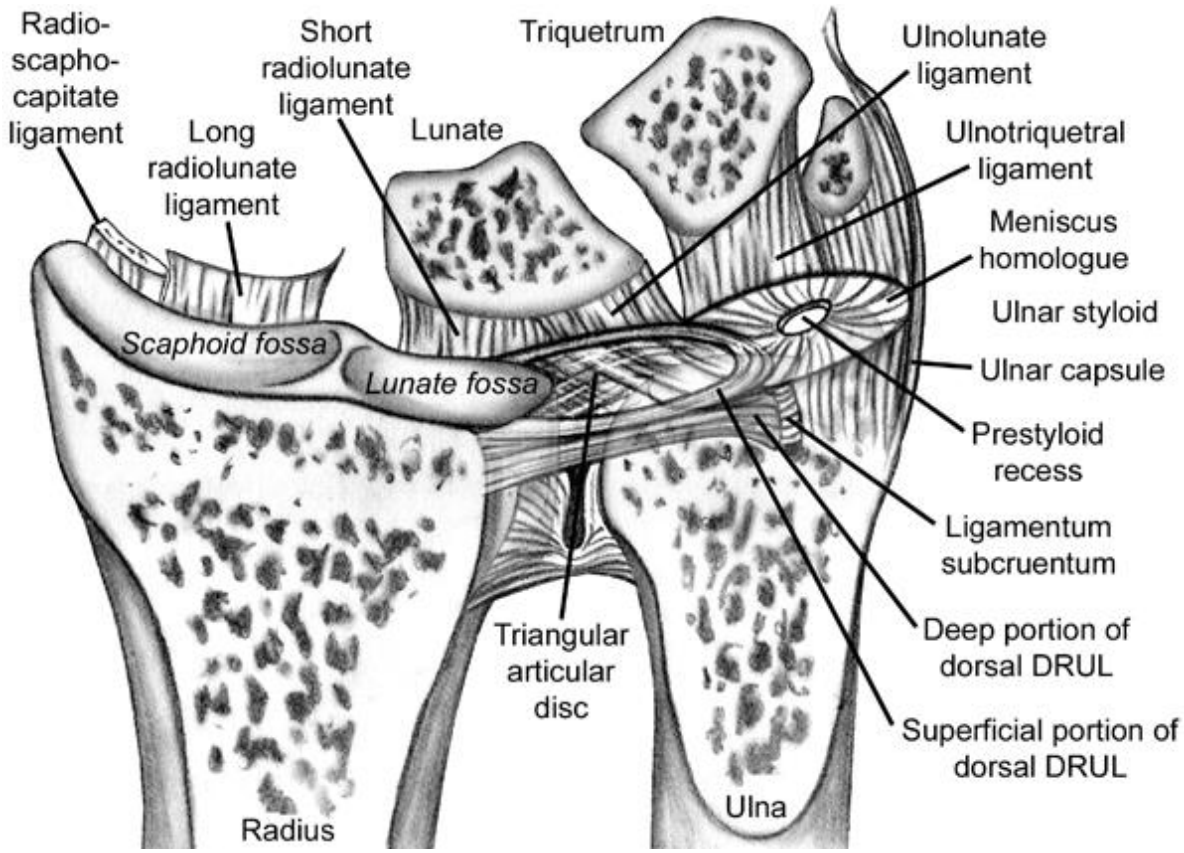

Figure 2.2-5: Cross-sectional view of the proximal wrist highlighting soft tissue components of the TFCC. [53]

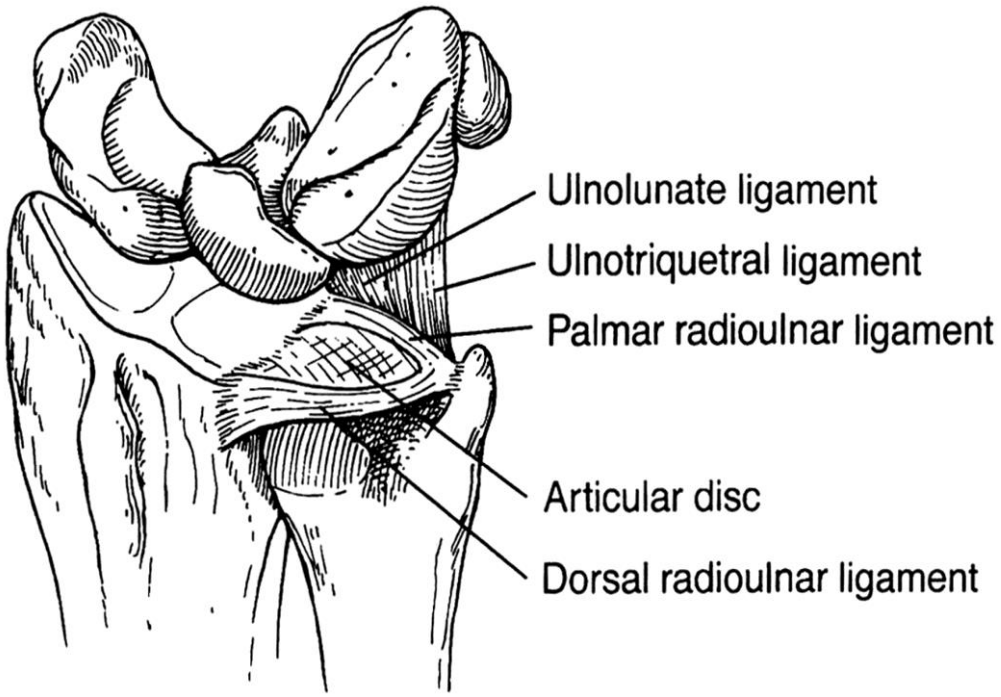

Figure 2.2-6: Ligaments of the forearm and wrist integrated with the TFCC. [54]

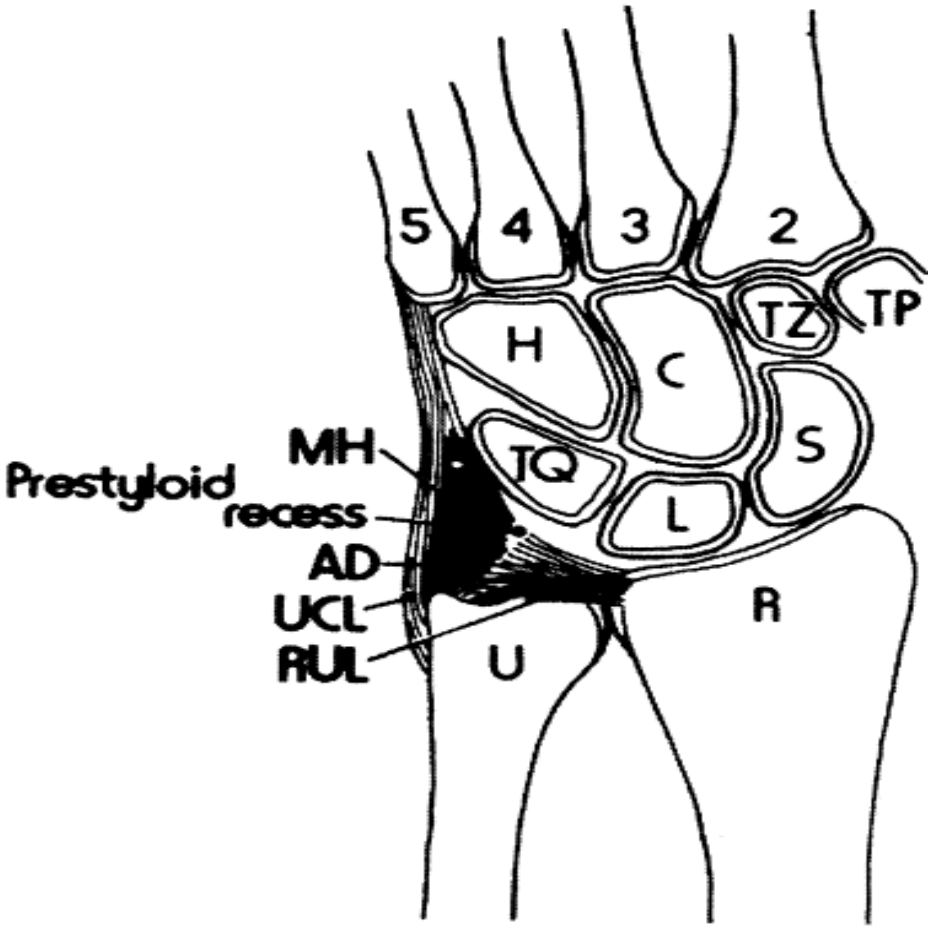

Figure2.2-7: Schematic of the structural components of the TFCC. [40]
MH- meniscus homologue
AD- articular disc
UCL-ulnar collateral ligament
RUL-radioulnar ligaments
ECU not shown

The TFCC is an important component for stability of the distal radioulnar joint. This structure also acts as a supporting cushion for load transfers from the lunate and triquetrum. [40] Due to the larger articulating surface, the radiocarpal articulating region supports about 80%while the TFCC supports about 20% of the load during compressive perturbations and transfers the force to the forearm. [40] The complete excision or degeneration of the TFCC may significantly reduce the forces transmitted through to the distal ulna. [40], [55] Although ulnar variance may cause healthy individuals to have a structurally different sized TFCC, this

anatomical variation has still been found to lead to the same proportional (80-20) load distribution through the radiocarpal joint.

The TFCC has a broad connection with the ECU sheath. This causes the TFCC to act as a pulley to the extensor tendon. With complete excision of the TFCC, a 30% increase in excursion of the tendon has been experimentally observed. [55] This increased tendon excursion may lead to unnatural application of forces being applied to the carpus during ECU activation.

The TFCC is a complex soft tissue structure made up of multiple types of tissue. Starting from the meniscus homologue and the fibrocartilage articulating disc, to the integrated fibers from all the surrounding soft tissue structure, the complexes role is not very well understood. Overall, it is thought to provide stability to the ulnar aspect of the wrist during kinematic motions. First, the proximal region places a cradling role and provides an even and smooth articulating surface for the lunate and triquetrum. Secondly, the more distal region is a combination of soft tissue connections which wrap around the medial aspect of the wrist. While the TFCC may not directly connect to the carpal bones, by wrapping around them it most likely provides some stability in ulnar motions of the wrist.

2.2.3 Muscular Anatomy

There are six main muscles responsible for overall wrist motion. The wrist flexors are the flexor carpi ulnaris (FCU), the flexor carpi radialis (FCR) and the abductor pollicis longus (APL). On the wrist, the FCU inserts into the pisiform and acts to flex and adduct the wrist. The FCR tendon's insertion point is at the anterior base of the second metacarpal. The FCR usually acts to flex and abduct the wrist (Figure 2.2-8). With an insertion site at the base of the first metacarpal, the APL's primary function is not for wrist movement, but rather to abduct the

thumb at the carpometacarpal joint. However, this muscle does have a secondary function that assists with flexion and abduction of the wrist. The wrist joint extensors are the extensor carpi radialis longus (ECRL), extensor carpi radialis brevis (ECRB), and the extensor carpi ulnaris (ECU). The ECRL has an insertion point at the dorsal base of the second metacarpal while the ECRB inserts at the base of the third metacarpal. These two muscles act to extend and abduct the wrist. Conversely, the ECU inserts at the dorsal base of the fifth metacarpal and tends to extend and adduct the wrist (Figure 2.2-9).

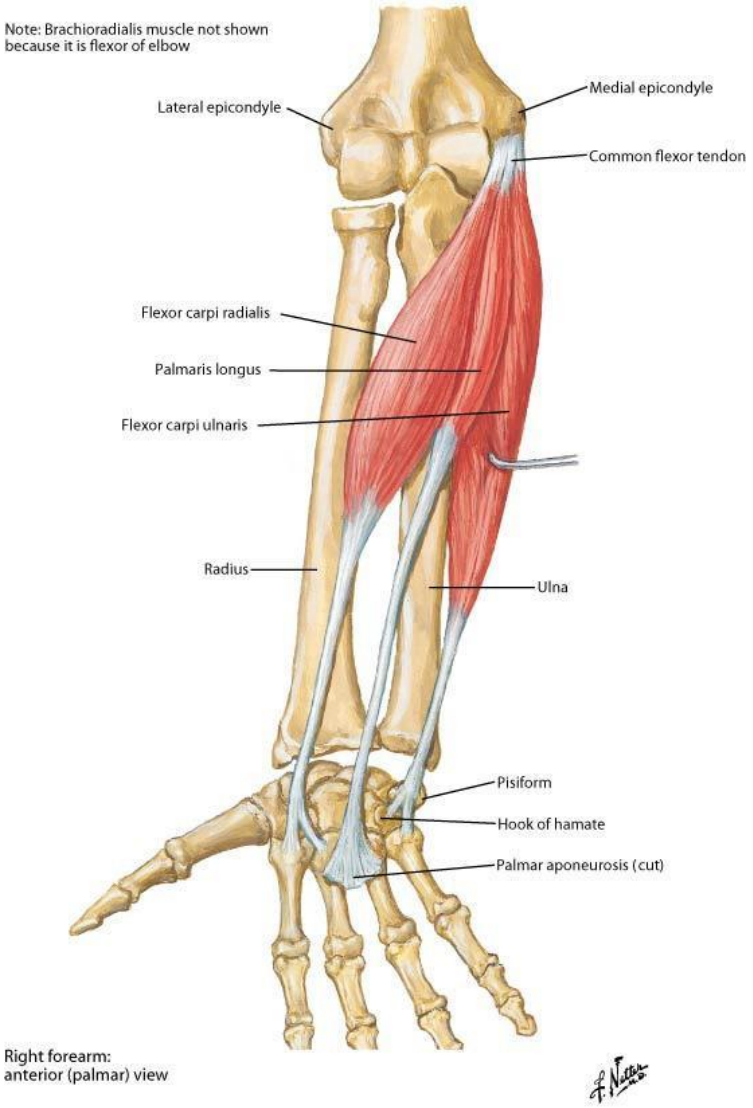

<u>Figure 2.2-8:</u> Flexor Muscles of the wrist joint. [56]

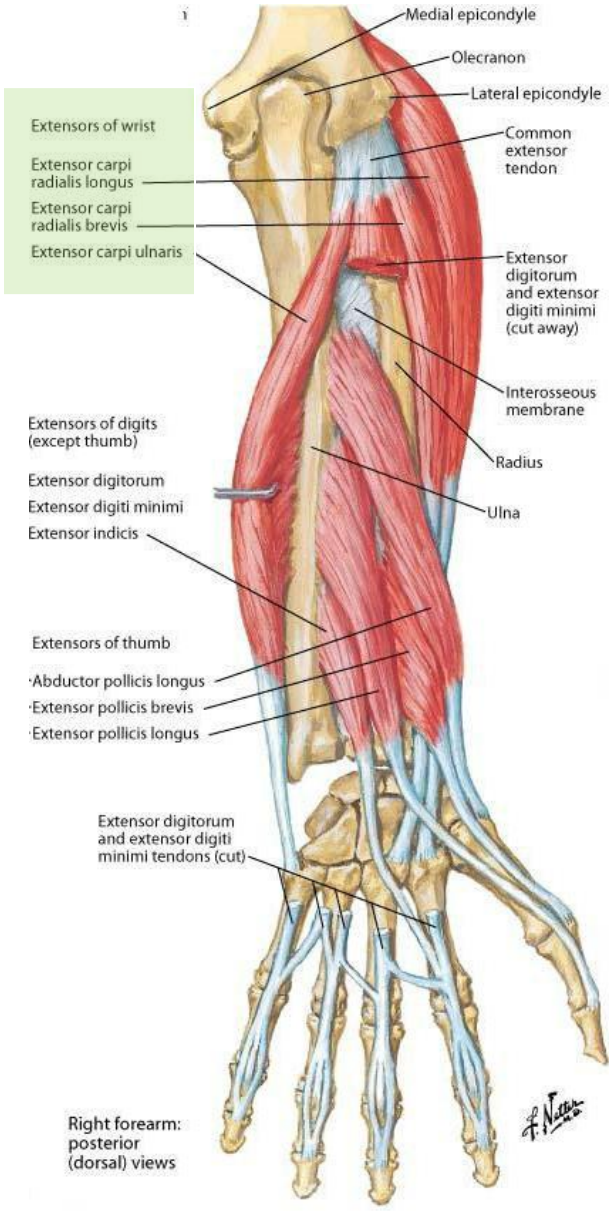

<u>Figure 2.2-9:</u> Extensor Muscles (highlighted green) of the wrist joint. [56]

2.2.4 Retinacular Anatomy

The wrist has a complex retinacular system which assists in maintaining normal relationships for all the tendons that cross the wrist joint. This system acts as pulleys to redirect the line of action of each tendon through the joint's range of motions. The retinacular system is a fibrous connective supporting system with three main functions; maintain mobile components in their defined compartment, protect and retain the elements it surrounds, and to redirect the tendinous muscular forces to maintain normal lines of action. [57], [58]

Anatomical studies have shown that the hand's retinacular system is essentially a distal extension of the antebrachial fascia of the arm. This fibrous structure courses distally up to the base of the metacarpals where it thins out and blends in with the fibers of the palmar aponeurosis. Based on the aspect of the hand, the retinacular system can be divided into two parts: the flexor retinaculum (FR) and the extensor retinaculum (ER).

Flexor Retinaculum

There is some controversy within the literature regarding the nomenclature and terms used to identify the different regions of the palmar retinacular structure. The most accepted description of the of the FR has been put forward by Cobb et al [59], in which the FR was divided up into three regions. The first is the proximal region, which is continuous with the forearm antebrachial fascia. The second is the intermediate region which has been identified as the transverse carpal ligament (TCL), (traditionally identified as the flexor retinaculum) a thick fibrous structure attaching and spanning between the carpal bones. The third is the distal region, a fibrous structure between the bases of the thenar and hypothenar muscles with some fusion with the fibers from the longitudinal layer of the palmar aponeurosis (Figure 2.2-10). In many

existing anatomical texts, the terms flexor retinaculum and transverse carpal ligament are used synonymously to describe the same structure, while others use the terms to describe separate structures.

On the palmar aspect of the forearm, the deep layer of the antebrachial fascia thickens and forms the proximal region of the flexor retinaculum at the radioulnar joint. This band of tissue spans across the radius to the ulna. This thick layer of tissue is formed from two layers of fibrous tissue which become re-apposed as they attach at the medial and lateral borders of the radius and ulna. [59] At the proximal and mid carpal row, the fibers of the proximal part of the TCL attach laterally to the scaphoid tuberosity and medially to the pisiform. The TCL continues to extend distally and at the distal carpal row the structure connects medially to the hook of hamate and laterally to the ridge of the trapezium.[57] This structure also forms the closure of the carpal tunnel of the wrist. The carpal tunnel is a fibrous compartment through which all the palmar tendons and some nerves travel through to the distal hand. On the distal end of the FR structure, the FR extends up to the base of the third metacarpal. At this point the distal portion forms the origin of the thenar and hypothenar muscles. [59] In this region, the fibers from the palmar fascia overlap and fuse with the distal region of the FR. [57], [59]

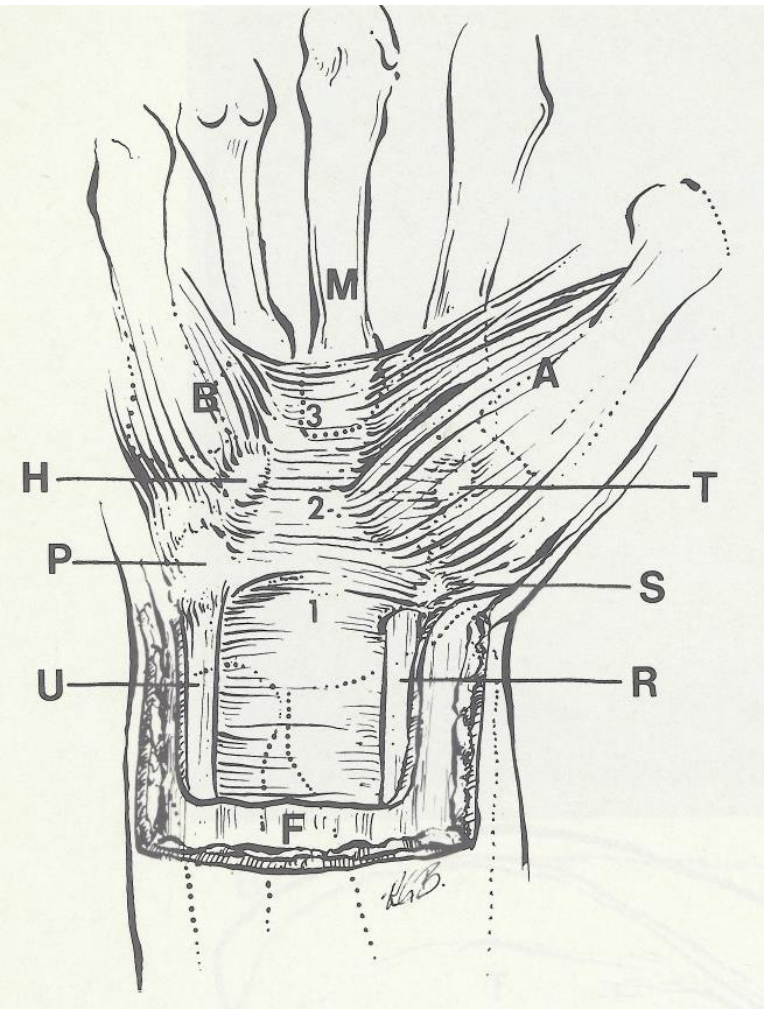

Figure 2.2-10: Drawing demonstrating the three portions of the flexor retinaculum. [59]

1- **Proximal portion if the FR formed from the antebrachial fascia (F).**
2- **Medial portion of FR, also referred to as transverse carpal ligament.**
3- **Distal portion of FR, aponeurosis between thenar (A) and hypothenar muscles (B).**

Extensor Retinaculum

The ER is a thick fibrous structure located on the dorsal radial and ulnar aspects of the wrist joint (Figure 2.2-11). The ER is also formed from the distal extension of the deep forearm antebrachial fascia. This structure is formed from two layers: the supratendinous and infratendinous layers. [31], [60] The structures of the ER form six major compartments containing the different dorsal tendons crossing the wrist joint (Figure2.2-12). The

supratendinous layer is the major layer of the structure, forming the thickest part of the ER. Laterally, it inserts into the radius and forms the lateral septum of the first compartment. The layer then runs slightly obliquely and attaches to the ulnar side of the triquetrum and pisiform. The fibers also blend in with the fibers of the FCU tendon and other soft tissues at the distal end of the TFCC structure. The infratendionus retinaculum is a narrower and shorter sheet of parallel fibers as compared to the supratendious retinaculum. Overall, the lateral end of the ER attaches to the distal part of the anterior border of the radius. While the medial end of the ER attaches to the styloid process of the ulna, the pisiform and the medial border of the triquetrum. [41]

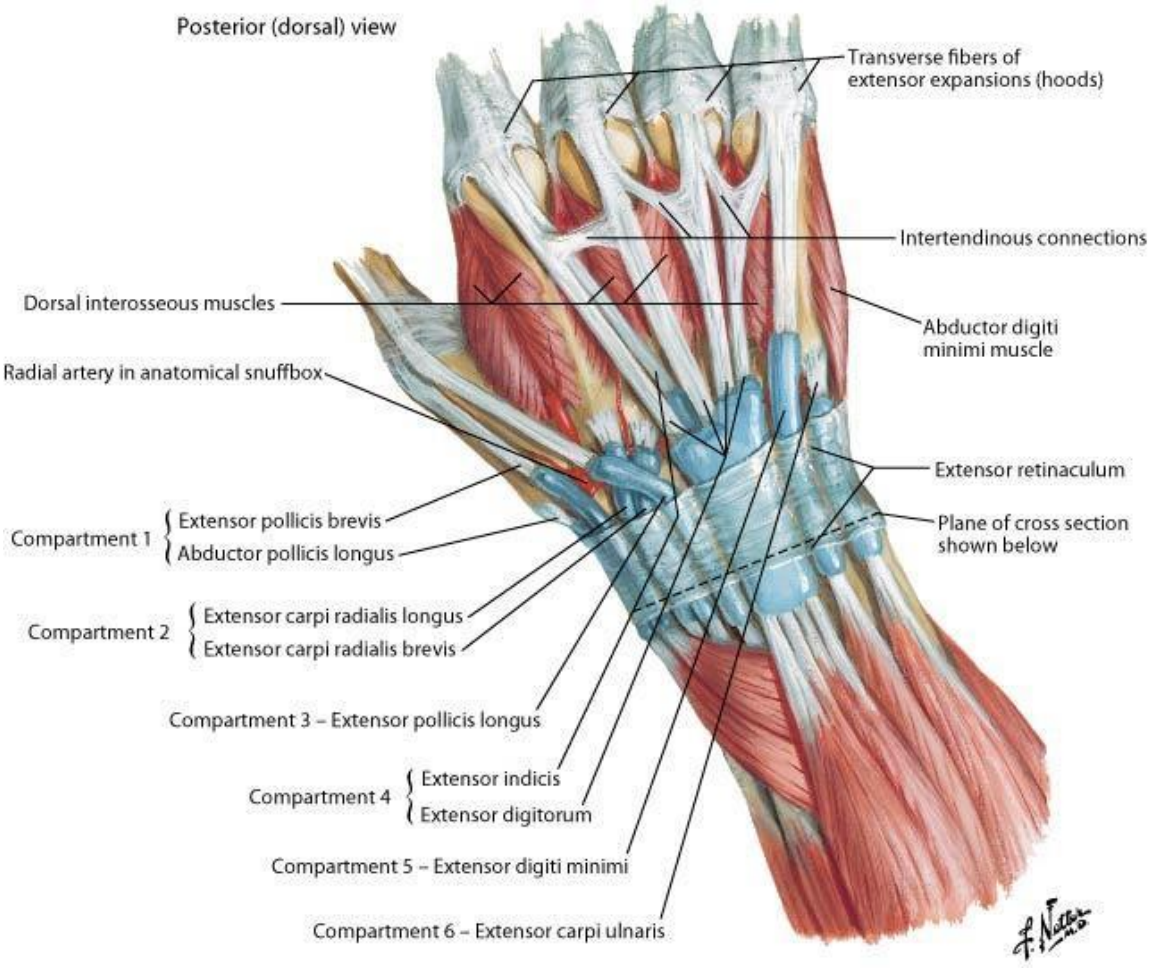

Figure 2.2-11: Dorsal aspect of hand showing extensor retinaculum (top) and Cross-sectional view of extensor retinaculum compartments (bottom). [56]

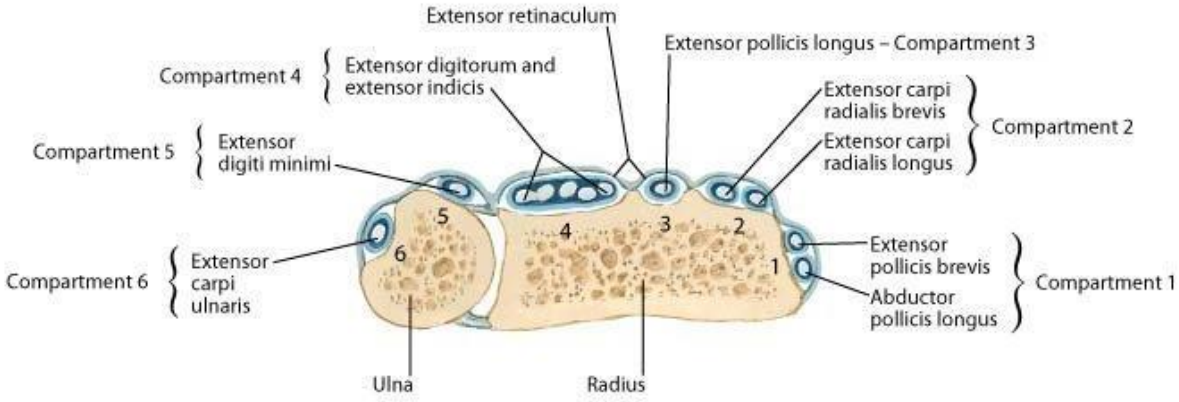

Figure 2.2-12: Cross-sectional view of the distal radioulnar joint and the compartments of the extensor retinaculum. [56]

As with the TFCC, the stabilizing role that the capsular retinacular structures play upon the wrist is not well understood. While there are some experimental studies that looked at the biomechanical effects of these tissue structures, the literature does not provide a complete understanding. Studies have demonstrated decreased carpal arch stiffness [61] and increased carpal arch length [62] with sectioning of the TCL for carpal tunnel release. Additionally, significant bowstringing and tendon excursions to non-anatomically correct lines of action were also observed following sectioning of the FR [62] and the ER [31]. While these studies do not directly indicate any effect the retinaculum might have in carpal kinematics, it does indicate that an overall stabilizing role is performed with all the surrounding tissue. By wrapping around all the tendons, soft tissue structures and the deeper skeletal structures, the reticulum should compact and secure all the tissues together. Its stabilizing role may be further enhanced in a deficient wrist that has undergone trauma or surgery. In this deficient state, the primary stabilizers may not be able to be as effective as they are designed to be and so these capsular structures may in fact passively stabilize the weakened joint.

CHAPTER 3: THREE-DIMENSIONAL WRIST MODEL FORMULATION

3.1 OVERVIEW

The aim of this study was to develop a high resolution, physiologically accurate computational model of the human wrist joint and to study the biomechanical function of the joint using the rigid body modeling (RBM) technique. RBM involves studying the interactions between a system of solid bodies that are supported or restricted based on defined properties or boundary conditions. For the wrist, this involves accurately representing the fifteen bones and their articulating surfaces and recreating the limiting factors enforced by the ligaments and other supporting soft tissues. In this study, high resolution computer tomography (CT) scans of a human upper extremity were used to create a three-dimensional (3D) representation of all the relevant bones and soft tissue structures. Once an accurately represented model of the wrist was formulated, motion studies were conducted by replicating wrist muscle action using a commercially available computer aided design (CAD) program and its native kinematics study tool.

3.2 COMPUTED TOPOGRAPHY OF THE WRIST

The 3D anatomy of the wrist model was obtained from a high resolution CT scan of a fresh frozen left upper extremity of a 52 year old male donor (Figure 3.2-1). The specimen was inspected for any obvious pathology, deformities and proper biomechanical range of motion. No obvious abnormalities were identified. The wrist was then scanned at high resolution with a

SOMATOM Sensation 64 helical scanner (Siemens AG, Forcheim, Germany). The specimen was scanned with the wrist at a neutral position, which is with the long axis of the third metacarpal in parallel to the long axis of the radius. Neutral position was achieved by visually estimating the placement of the wrist. It was later determined, however, that the wrist was scanned with 0.35 degrees of extension and 8.52 degrees of ulnar deviation. This offset had to be adjusted in the model.

Figure 3.2-1: Cadaveric specimen used for wrist model formulation.

For the purposes of this model, it was essential to obtain high resolution images to ensure the capture of all intricate details of the bony articulations within the wrist joint complex. The

scan resolution was 512 x 512 pixels with each pixel containing twelve bits of data. Scan slices were separated by 0.4mm increments for a total 2283 two-dimensional (2D) slice images.

3.3 THREE-DIMENSIONAL BODY CREATION

3.3.1 Mask Creation

Once the high resolution CT scanned images were obtained, they were imported into the commercially available MIMICS (Materialise's Interactive Medical Imaging Control System, Version 13, Materialise, Ann Arbor, MI) software for processing. MIMICS is a specially developed software that is designed to process a number of different types of medical images and can be used in a wide range of engineering applications. In this study, MIMICS was used to take the 2D images from the CT scans and convert them into 3D structures to replicate the bony anatomy of the human wrist.

The 2283 2D CT images were sequentially imported into MIMICS and were arranged into arrays of DICOM (Digital Imaging and Communications in Medicine) images. DICOM images are a standard format for using, storing and transmitting medical images. Within MIMICS, this array or stack of images was then processed to form a 3D representation of the arm. The array was formed by voxels, or volumetric pixels, whose top and bottom faces were formed by pixels from two adjacent slices. Side faces of the voxels were dictated by the slice thickness. Since the length of a pixel is not equal to the distance between the slices, the model was comprised of rectangular voxels.

The entire stack of images was then processed to efficiently capture the bony structures within the specimen. This was done by using a global thresholding tool, which can analyze each

pixel on a slice of the scan and designate it an active (bright) or inactive (dark) status. The tool measures the Hounsfield units (HU), which is a scale that describes the radiodensity of a structure. Each analyzed pixel was assigned an active or inactive state based on the HU range desired by the user. In MIMICS, a standard threshold range for bone is defined to be between 226 to 1703 HU. When this range was used within the scan, it was found that some cortical bone and a large part of trabecular bone remained unselected (Figure 3.1-1). This was most likely due to the low linear attenuation coefficient of trabecular bone and the low density of cortical bone. Thus, the threshold value was adjusted to allow a complete global capture of bony tissue. After a number of trials, it was determined that the optimal range to capture the maximum amount of bony tissue, while selecting a minimal amount of soft tissue, was 180 to 1703 HU. This range was then used to form the global "mask" of the bony structures of the upper extremity.

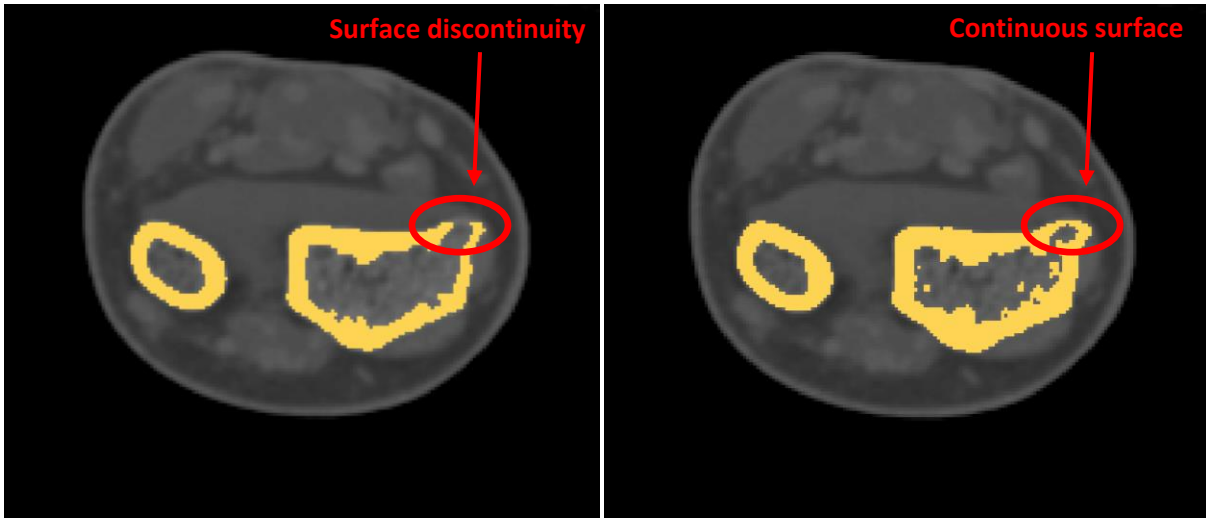

<u>Figure 3.3-1:</u> Thresholding tool used to select osseous structures with standard range (left) and redefined threshold range (right).

3.3.2 Mask Refinement

Once a global mask was obtained, it was further refined to eliminate any soft tissue or noise that may have been selected, as well as carefully define all the articulating surfaces between adjacent bones. MIMICS has a number of different editing tools that allow for global and fine changes to individual masks. The two tools used for quick mass editing were the cropping tool and the multiple slice edit tool. The cropping tool was used to select a region of interest within the scan. The multiple slice edit tool allowed for changes from one 2D slice image to be copied onto adjacent slices and thus enabled quick changes to be applied to the mask. The initial global mask obtained was of the full upper extremity. With the help of these two tools, the mask was edited and reduced to only incorporate the distal half of the forearm and the complete hand. In addition, any remaining noise, such as activated pixels from the scanned portion of the CT table, was also eliminated. This resulted in a complete active mask made up of a total of 754 images instead of the original 2283 images. This not only vastly reduced the file size but also made the images computationally less cumbersome.

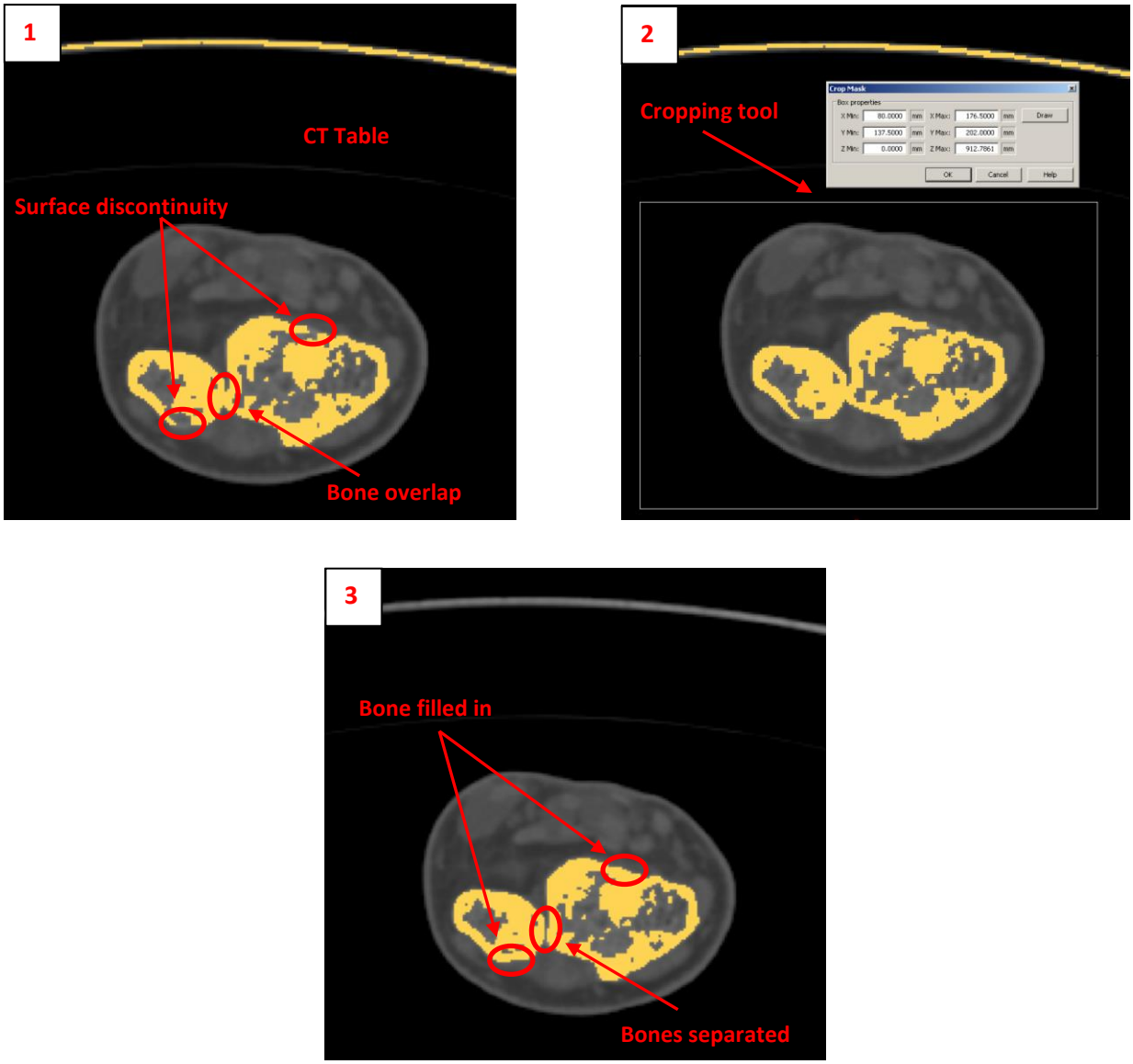

<u>Figure 3.3-2:</u> Mask refinement steps:

1- **Mask created from threshold tool, capturing bone and CT table**
2- **Cropping tool used to eliminate undesired elements from mask**
3- **Slice editing tool used to fill in discontinuities and separate bone overlap**

Once the global mask was refined to a satisfactory point, it was then divided up to give each bone its own individual mask. Fifteen wrist bones were of interest in this study including the two long forearm bones, eight carpal bones, and five metacarpal bones. The phalanges were

also extracted from this mask; however, the phalanges of the fingers and thumb were represented as one mask within the design space.

For the extraction of each bone into its own mask, the group editing tools previously described were used. Additionally, MIMICS has a number of Boolean Operation tools which allowed for quick mask manipulations. These operation tools prevent the need to repeat the same mask editing steps in different masks. The two main Boolean operation tools used for this study were those that allowed for a mask to be added or subtracted from another. These tools were utilized to quickly remove individual bone masks from the global mask, thus allowing for faster acquisition of individual masks. During the creation of each individual bone mask, an additional tool was used to make very fine adjustments. Within the original unedited mask of the proximal arm, it was found that most of the articulating surfaces would not be rendered as smooth surfaces. Furthermore, in many cases there were mask overlaps observed between bones. This was especially seen in the cases of the small carpal bones which also had very small joint space. The joint space between these bones was not distinct enough in the scans and so had to be individually defined and separated. In other regions, surfaces were found to have jagged edges due to thinning or high porosity of the bone. These discontinuities may have also been caused by error in the designated thresholding range. Corrections to these misrepresentations were achieved by editing each individual slice of the mask and appropriately selecting or deselecting pixels using the slice editing tool. This was done to ensure capture of a smooth, continuous articulating surface. This step also allowed manual compensation for any deficiency or irregularities that existed within the wrist bones. As previously mentioned, accurately selecting and capturing the outer cortical layer was critical. If a region inside the outer layer was not selected, it was filled with the help of an additional tool described later.

MIMICS has the capability to analyze individual slices and masks to create various geometrical references such as fitted lines or points that are based on selected regions. The polylines function was used to create individual closed loops around each active selection on individual slices. Since it was ensured that each mask had at least an outermost selected surface layer of the bone, a polyline could be formed to encompass the entire bony region on that slice. This also allowed for the identification and correction of discrepancies that showed discontinuities, cavitations or sharp edges. Once a satisfactory polyline was obtained for all the slices, the exterior most polyline of each slice was used to fill in any voids or inactive pixels. These inactive pixels were usually due to the porous trabecular bone or medullar space of the long bones. Because the presence of hollow regions is not conducive to the RBM method, it was ensured that the entire bone was selected (Figure 3.3-3).

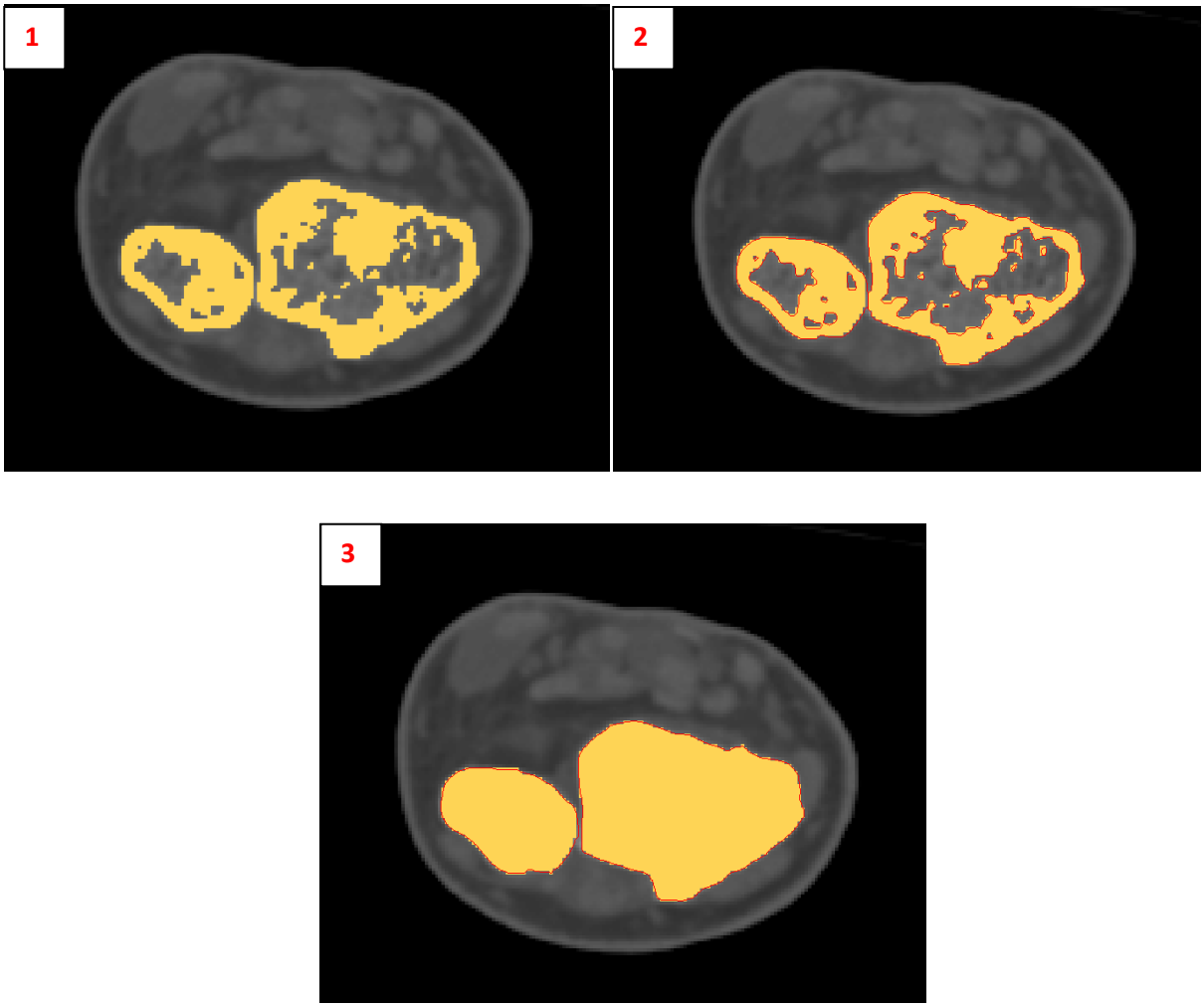

<u>Figure 3.3-3:</u> Mask manipulation in preparation to create 3D bodies.

1- **Refined mask with separated bones and continuous outer surface**
2- **Polylines created to encapsulate outer boundary of bone**
3- **Cavity Fill function used to fill all voids in each mask**

Once accurate masks of the wrist bones were developed, 3D bodies were formed from each mask (Figure 3.3-4). This was done in MIMICS by creating a linear interpolation between the boundaries of each active section on adjacent slices. Once formed, each bone was visually inspected and compared to anatomical texts for accuracy and to ensure all major landmarks had been captured. A final check confirmed that each body contained no extraneous noise and each mask contained only one body.

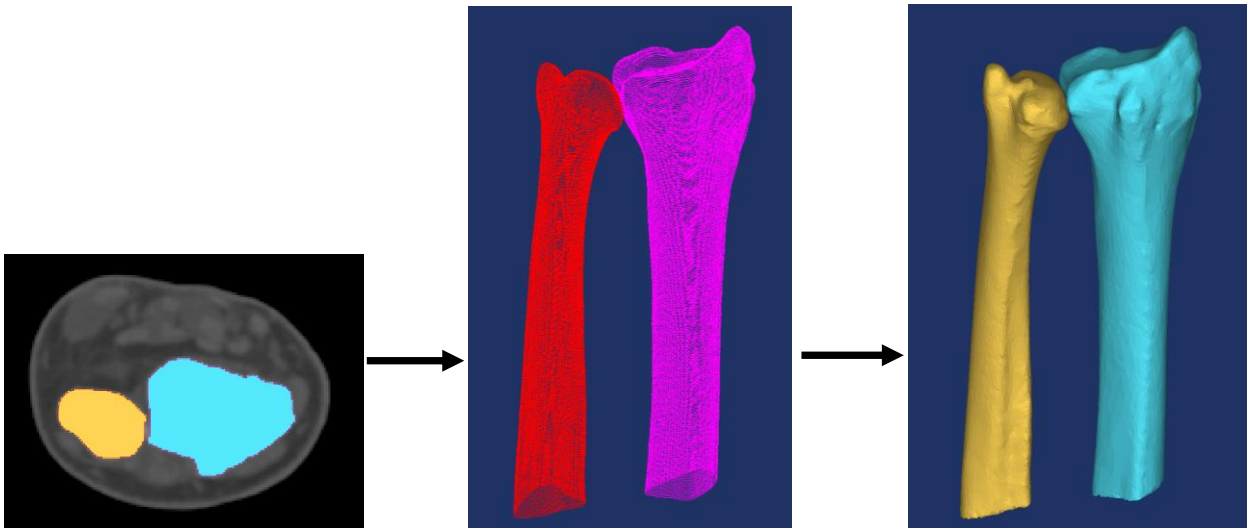

Polylines calculated from mask 3D Body formed from interpolation of polylines

Figure 3.3-4: 3D Bone model formation from individual masks.

3.3.3 3D Mesh Creation and Remeshing

Once a 3D body was created, its surface was represented as a network of triangulated surfaces, which is referred to as a 3D mesh. This triangulated 3D mesh forms the exterior surface of the bone, representing the shape and curvature as defined by the mask. However, the body may still contain significantly rough edges since features can be harder to identify while working in the 2D aspect. To allow for 3D body refinement, MIMICS has a number of tools which allow for the manipulation and modification of the 3D mesh. When a 3D body is first formed, the surface mesh can contain over 100,000 triangles depending on the size of the bone. Any commercially available CAD software would have a very difficult time in importing or using such a large complex file for its calculations. In fact, if such a large file was used for simulations, it would take an inordinate amount of time to converge to a final solution. In many

cases, the computational power may not be sufficient for solving and thus lead to failure. Additionally, the presence of sharp discontinuities within a body can also result in rapid changes during motion studies thereby producing inaccurate results or convergence failure. Thus, it was very important to utilize these remeshing tools to reduce the number of triangles and create a simplified, smooth surface that accurately represented bony contours.

The representative triangles of the 3D surface mesh were formed in a variety of different sizes, angles and dimensions. The overall position of each triangle was defined by the twelve Cartesian coordinates, three for each vertex, and three directional unit vectors. The triangle reduction and smoothing tools were used to refine the 3D bones. These tools allowed for the reduction of the 3D mesh triangles based on defined parameters. This remeshing led to the 3D mesh containing a smaller number of triangles, thereby making the model more computationally manageable. Ideally, a mesh formed by identical equilateral triangles is desirable as it leads to a more consistent regular mesh and allows for efficient solving of computer simulations.

Triangle reduction focuses on two factors to carry out its operation (Figure 3.3-5). First, it utilizes an algorithm to remove all highly acute and obtuse triangles from the mesh. This tool gives each triangle a dimensionless value between 0 and 1 where equilateral triangles are rated as 1 and highly acute or obtuse angled triangles are valued closer to 0. A threshold value is then designated by the user such that all triangles outside the threshold are eliminated while triangles within it are preserved. The eliminated triangles are then replaced with triangles having dimensions within the threshold. These new dimensions are driven by the dimensions and positions of the surrounding triangles. While this step alone does not significantly reduce the number of triangles in the mesh, it greatly improves the quality of the mesh to be formed by incorporating facets within a uniform range.

The second step in triangle reduction involves the evaluation of mesh triangle edge angles. In this case, the tool measures the angle between two facets and combines them based on a defined threshold value. If two facets have a very small edge angle, they are considered as one facet. Any corresponding triangles that have angles greater than the threshold are considered two unique facets and the original orientation is maintained. The threshold angle defines the minimum angle needed between two facets to preserve or accurately represent the surface geometry of the body. For the purposes of this study, the threshold value for the first step was set at 0.3 and the threshold for the edge angle was set at 15 degrees. These values were obtained after a number of trials determined the best outcome in reducing the triangular mesh while still preserving the total 3D volume of the body.

The next tool used during the remeshing process was the smoothing operation. Smoothing allows for the removal of any small cavitations, spikes or discontinuities that may still exist on the represented bone surface. The operation examines the vertices of each triangle and the corresponding neighboring triangles that share the common vertex. In this study, the smoothing analysis led to a weighted value being assigned based on the Smoothing Factor ratio. During this manipulation, each vertex of all the triangles was no longer fixed and was reoriented within the coordinate system based on the assigned weighted value. If the ratio was low, then the initial position of the vertex was predominantly responsible for the new position in space. However, if the ratio was high, then the new position of the vertex was driven by the position and coordinates of the vertices of all the adjacent triangles. This operation resulted in the vertices being redefined to a new position based on the coordinates of vertices common to multiple triangles. While this tool was very effective in quickly removing discontinuities and

cavitations, care had to be taken to ensure that essential landmarks were not inadvertently removed.

For both of these operations, multiple iterations had to be performed to result in a satisfactory outcome. The number of iterations also depended on the bone itself with larger bones requiring a greater number of iterations. For the long bones like the radius and ulna, a maximum number of fifteen iterations were performed. For the smaller carpal bones, fewer iterations were sufficient to obtain a final acceptable structure.

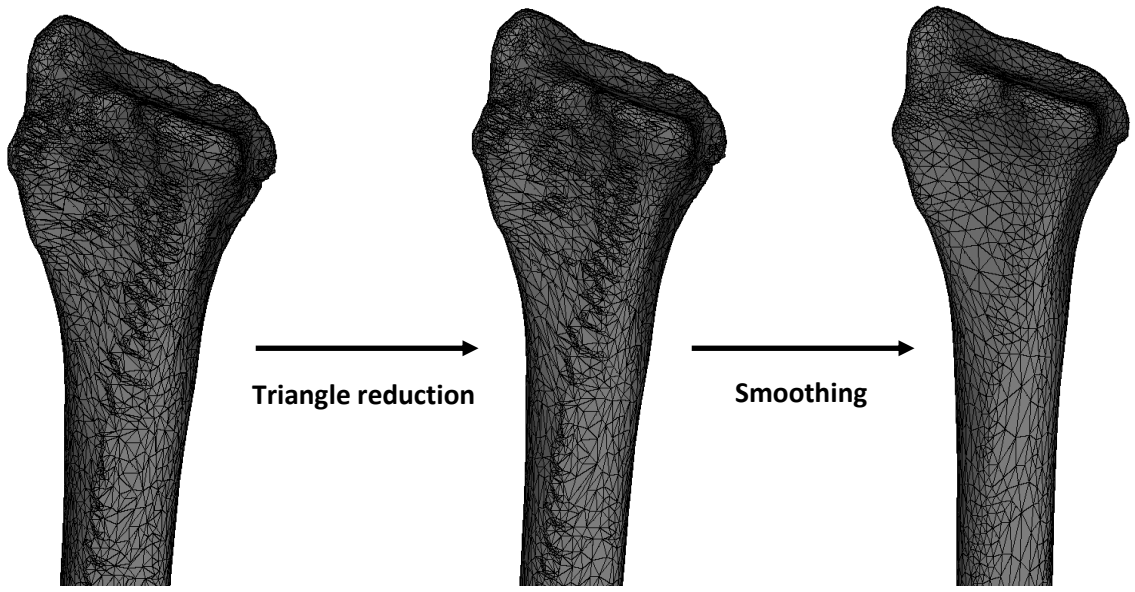

<u>Figure 3.3-5:</u> 3D triangulated mesh formation for radius (left) with additional remeshing performed with triangle reduction tool (center) and smoothing tool (right).

Once remeshing was complete, a final visual inspection of the bodies was completed. In some cases, individual points and triangles were still found that had not been corrected by the global smoothing and triangle reduction operations. A few very sharp points or cavitations were easily identified in all the bone structures. In these cases, the individual triangles in the region were manually manipulated to correct the anomaly. Individual triangles were deleted and redrawn by moving, adding or deleting nodes. Again, very precise care was taken to ensure that an accurate, continuous smooth surface represented the bone structure.

3.3.4 STL Files and SolidWorks

Once the remeshing operation was complete, a final high quality mesh of triangular facets was obtained that accurately represented the shape and major landmarks of each individual bone. Each body was then exported from MIMICS as a stereolithographic (STL) file. STL is a file format widely used in rapid prototyping and CAD programs and is supported in most 3D modeling software packages. STL files only describe the 3D surface geometry of an object without any representation of color, texture or other parameters or attributes. Individual STL files for each bone were imported into SolidWorks and saved separately as part files. During this importation into SolidWorks, each vertex and triangular facet were recreated to rebuild an identical body as was formed within MIMICS.

3.4 SOLIDWORKS AND ASSEMBLIES

SolidWorks (SolidWorks 2010, Dassault Systèmes SolidWorks Corporation, Waltham, MA) is a commercially available 3D CAD software used by designers and engineers. After saving them in SolidWorks, all the individual parts were then assembled together into one design space to form the complete joint. These individual parts could be defined to move and interact in specific ways relative to each other. Since the radius is the major supporting bone of the wrist, it was entered into the design space first. The radius was fixed within the design space such that it could not be moved relative to the global coordinate system. Each subsequent bone was then entered into the assembly space with its orientation and position defined by the initial CT scan. As each bone was placed, it was fixed relative to the radius to prevent any movement while the model was formulated.

Once all the bones had been assembled together (Figure 3.4-1), definitions set forth by the International Society of Biomechanics (ISB) [1] were used to align the coordinate system of the design space with the anatomical coordinate system. According to ISB, each bone in the wrist has its own coordinate system [63]. However, for the purposes of this study, global wrist motion was only of interest. Traditionally, global wrist motion is described as the motion of the third metacarpal with respect to the radius. For the radius, the coordinate system was based on ISB definitions, which was then used as the global coordinate system of the model. Additionally, the long axis of the third metacarpal was also defined. Thus, wrist motion angles within the model were measured between the long axis of the radius and third metacarpal.

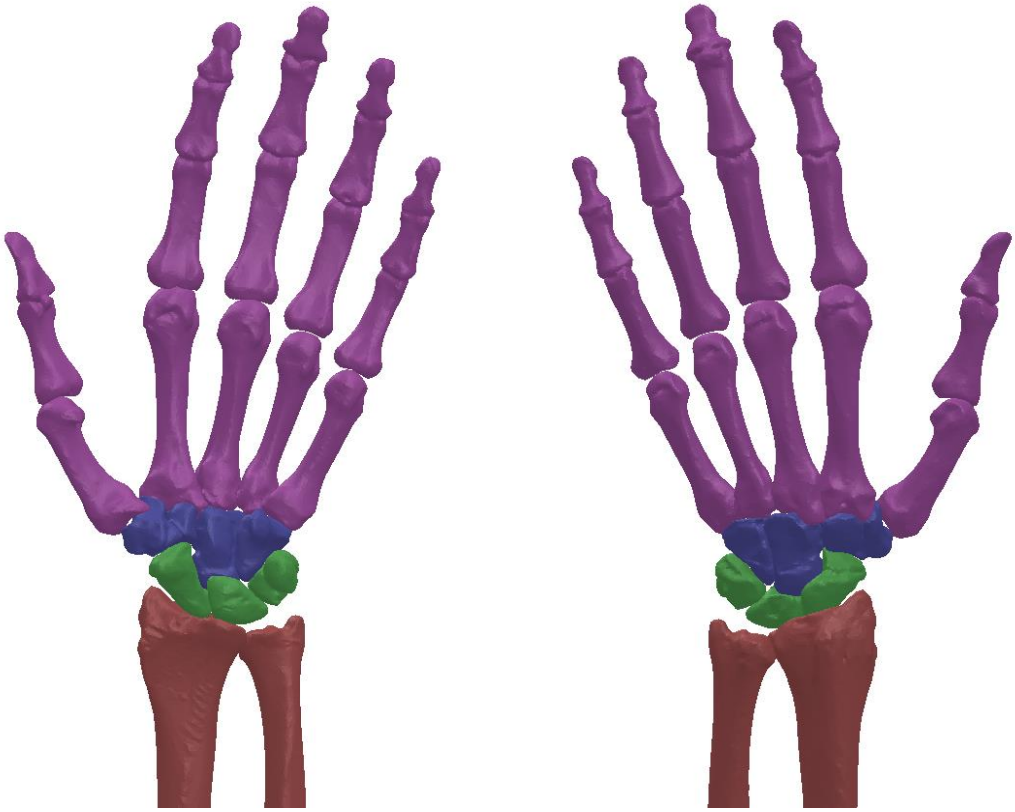

Figure 3.4-1: SolidWorks Assembly of 3D bodies representing the bones of the wrist.

3.5 SOLIDWORKS MOTION

Once the 3D wrist bone assembly was completed within SolidWorks, it was then transferred to SolidWorks Motion design space. SolidWorks Motion, an add-in that is native to SolidWorks, can be used to simulate and analyze motion studies of different structures or assemblies. This tool allows the addition of and control over various elements such as forces, springs, dampers, and friction. Further, Motion enables the addition of restrictions such as mating, fixing, or defining boundary conditions of structures. This motion analysis tool can provide the researcher with a large amount of kinematic data and force results.

In SolidWorks Motion, all the soft tissue structures were represented and additional restrictions and boundary conditions were incorporated. However, first the motion analysis study properties had to be defined. The motion study rate was set at 50 frames per second. A high frame rate was selected to allow enough calculation points to accurately converge to a solution. However, if too high of a frame rate was used, it could also lead to very long computational times. Next, the geometric accuracy and 3D contact resolution of the study was set to the maximum range. Since motion analysis is primarily dependent on the contact reactions between the bone articulations, it was imperative to maintain high accuracy of the surfaces during a calculation.

SolidWorks Motion computationally solves studies by iteratively solving the equations of motions. It also considers additional user-defined forces and restrictions on the system. These equations are solved for every time step to approach the final solution for the overall system.

For this study, the bones were defined as rigid solid bodies. To achieve this, SolidWorks has a unique modeling method. To resolve solid body contact, the 3D contact feature first calculates the amount of overlap that may exist between bodies during each time step. If some overlap is detected between two or more bodies, it applies a force to the centroid of the elements in the opposite direction of the overlapping body. This force is proportional to the amount of volumetric overlap occurring between the bodies and the defined stiffness of the material. For this study, stiffness was defined as 10,000 N/mm with a penetration depth of 0.001 mm and a damping coefficient of 50 N/mm-s. These values were determined to be the optimal values to limit the amount the overlap, while replicating the amount of repelling force experienced when solid bodies experience contact.

3.6 LIGAMENT STRUCTURES

Once the bony tissues of the wrist were defined, the soft tissue structures were then represented within the model. As done in most RBM studies, the wrist ligaments were modeled in SolidWorks as tension only spring elements with no resistance to compression. They were defined as straight line elements spanning the ligament attachment sites with properties determined from experimental studies published in the literature.

3.6.1 Origins and Insertions

Recreating the wrist ligaments as elements in SolidWorks Motion involved first identifying all the origins and insertions of each ligament. Literature and anatomical texts [29], [36], [43], [56], [64–69] were used to identify these attachment sites. Ligament attachment points were found in relation to various landmarks or reference points on the individual bones. Within the literature, there is a large variation in descriptions of the wrist's ligamentous anatomy. This variation is primarily due to the number of ligaments in the wrist, their relatively small size, anatomic variability among individuals, as well as the complexity of the overall system. Chapter 2 of this text discusses in depth the ligaments and structures that have been implemented in this model of the wrist.

Each ligament was modeled as a straight line spring element that only resisted tension. Since ligaments can be wide structures spanning attachment sites, each was modeled using at least two linear spring elements. In some of the larger and wider ligaments, three elements were used. The two elements were usually placed towards the outer margins of the ligament. In representing the interosseous ligaments, two or three different bands were used, each represented by two separate elements. Modeling the wrist in such a manner allowed sufficient replication of the multi-directional constraining effects of an actual ligament.

Each origin/insertion attachment site was marked on the model structures ensuring that it coincided with a vertex, or node, on the triangulated surface mesh. Each point was fixed to the node. Ligament attachment sites were usually represented by two points at either end of the site. Thus, most ligaments in the model were represented by four points, with the exceptions of those described below. The spring elements were then drawn between the attachment sites anchored to the respective points.

While most of the ligaments were simply modeled with two spring elements and four attachment points (Figure 3.6-1 – Figure 3.6-4), a few of the ligaments were modeled differently due to broad insertion sites. The wrist contains six sets of interosseous ligaments (SL, LT, PT, TT, CT, and HT). All of these ligaments have both a dorsal and a palmar component. In the model, each of these ligaments was modeled with two different bands, containing a total of four spring elements and eight attachment points. In the human wrist, the RSC ligament also has multiple attachment points. As described in Chapter 2, the RSC originates on the palmar rim of the radius and courses distally with some fibers attaching onto the scaphoid while the remaining part of the ligament attaches on the capitate. In the model, this structure was represented by two different bands. One band spanned between the radius and scaphoid while the other spanned the radius and capitate. These were referred to as the radioscaphoid (RS) ligament and the radiocapitate (RC) ligament. Each of these ligament portions was modeled with the standard two bands and four attachment sites. In the case of the STT ligament, it was represented as three elements in the model. Since the ligament originated on the scaphoid and had insertions on both the trapezium and the trapezoid, two elements were attached to the trapezium and one element attached to the trapezoid. Finally, the intermetacarpal and carpometacarpal ligaments were each modeled with only one spring element (Figure 3.6-5 and Figure 3.6-6).

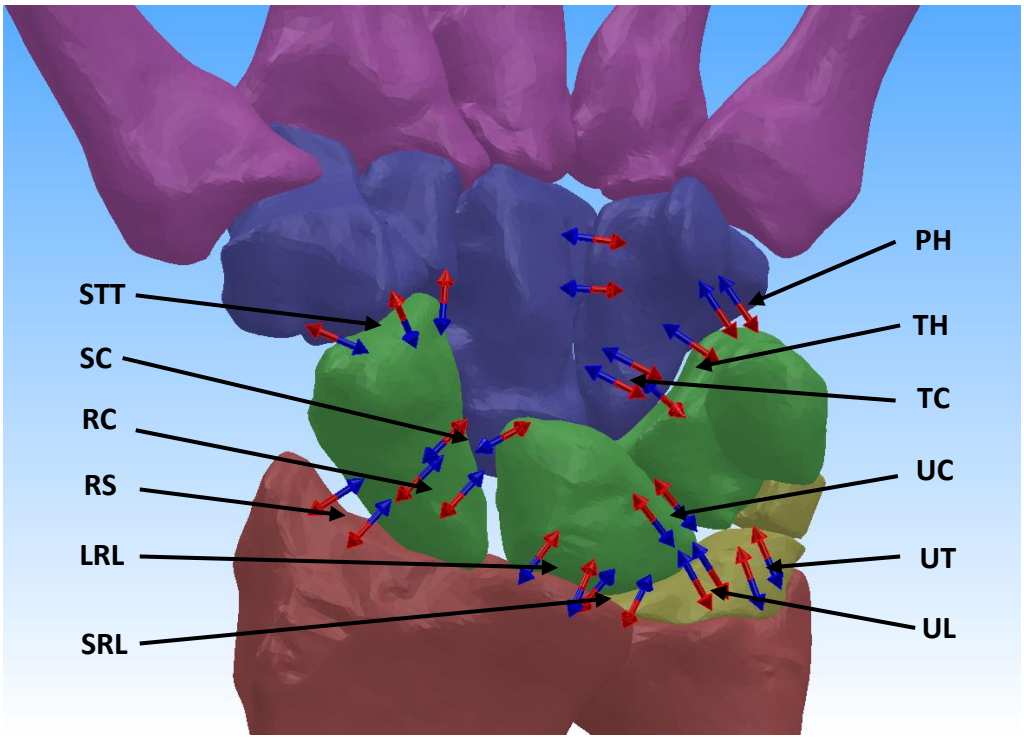

Figure 3.6-1: Palmar extrinsic wrist ligaments in wrist model.

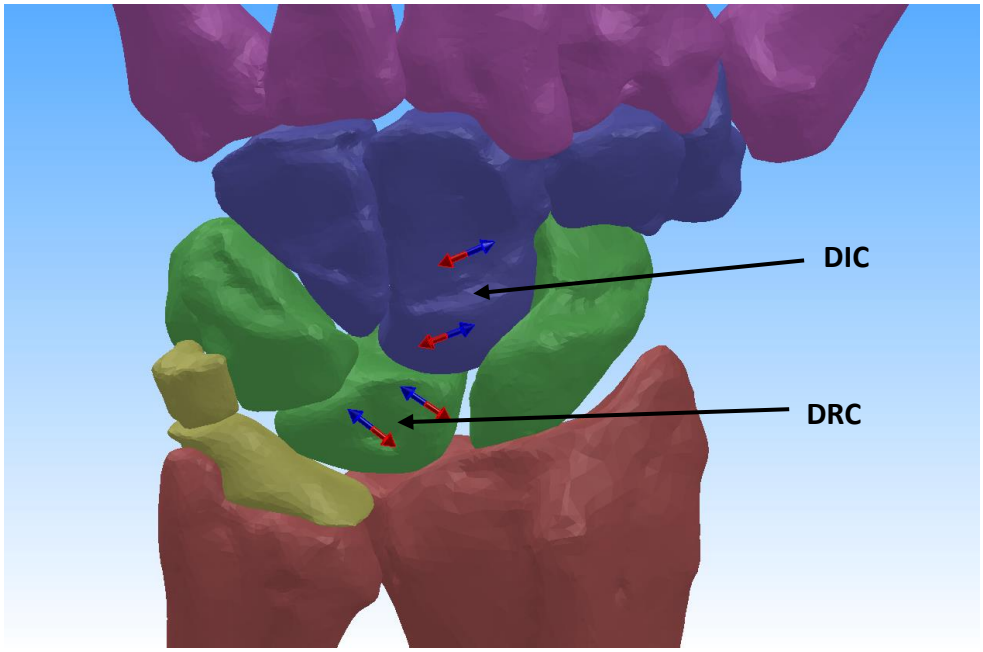

Figure 3.6-2: Dorsal extrinsic wrist ligaments in wrist model.

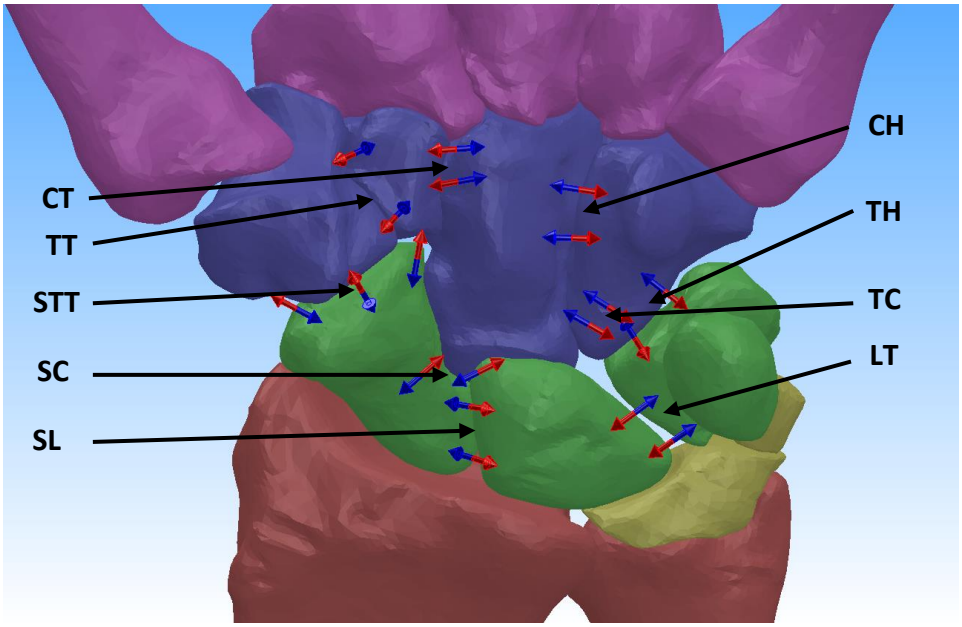

Figure 3.6-3: Palmar intrinsic wrist ligaments in wrist model.

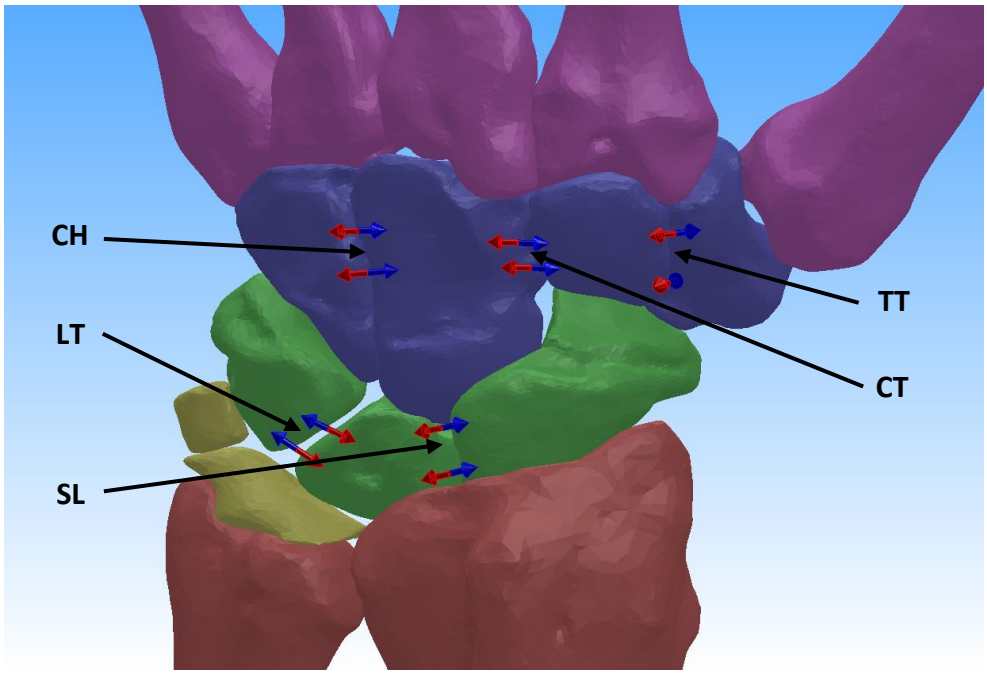

Figure 3.6-4: Dorsal intrinsic wrist ligaments in wrist model.

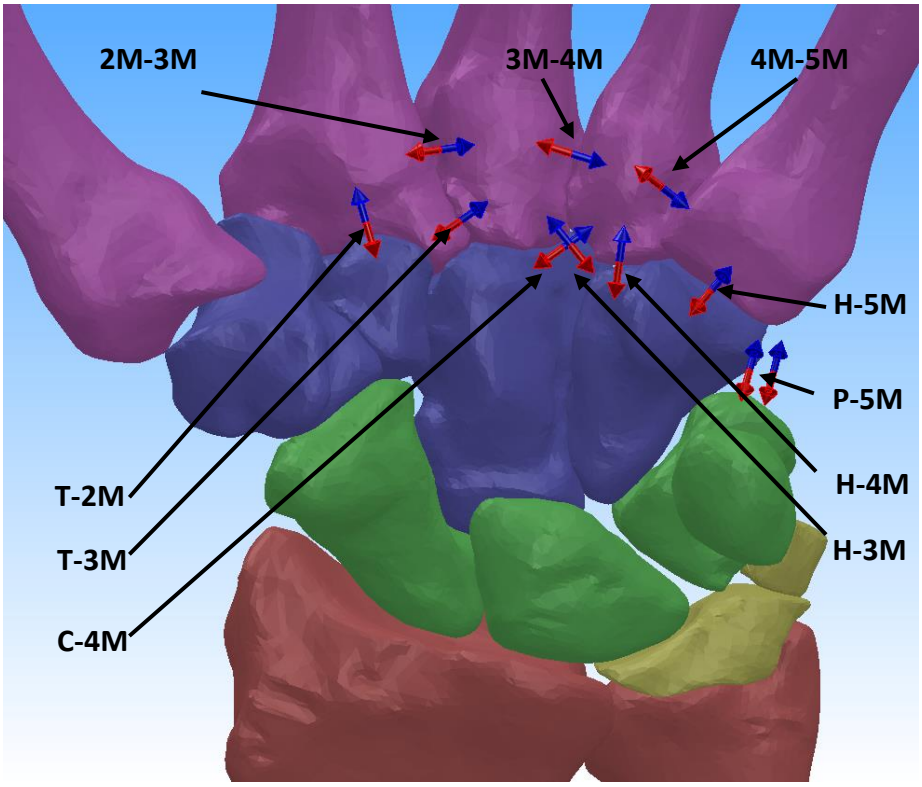

Figure 3.6-5: Palmar carpo-metacarpal and metacarpal ligaments in the wrist model.

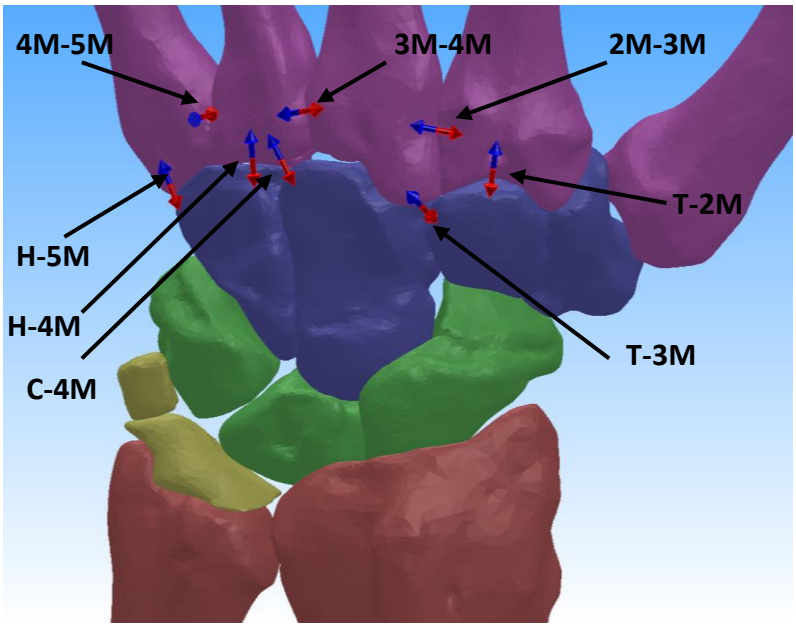

Figure 3.6-6: Dorsal carpo-metacarpal and metacarpal ligaments in the wrist model.

3.6.2 Ligament Mechanical Properties

Once the anatomical locations of the ligaments were identified and the spring elements incorporated, the mechanical properties were defined. Many experimental cadaveric studies have been conducted which have tested and determined mechanical properties (stiffness, modulus, in situ strain and stress free length) of the ligaments. For the purposes of this model, stiffness values of each ligament were incorporated in the model. Stiffness values were chosen to drive the behavior of spring elements in SolidWorks Motion to recreate the tissue's structural property. Stiffness values were identified from reported results from mechanical experimental studies. [18], [37], [39], [61], [70] In some experimental studies, the modulus of the ligaments was reported. [37] These values were converted to stiffness by factoring in the average cross-sectional area reported for the specific ligaments. Most of the stiffness values were reported from either load-displacement curves on isolated ligaments or bone-ligament-bone mechanical tests. While there was some variation in values reported in the literature, specific stiffness value selections were made for the model based on the investigators' experimental methodology (Table 3.6-1, Table 3.6-2 and Table 3.6-3).

Ligament Name	Total Ligament Stiffness (N/mm)
Radioscaphoid Ligament (RS)	50 [18], [48]
Radiocapitate Ligament (RC)	50 [18], [46], [48]
Long Radiolunate Ligament (LRL)	37.5 [37], [39]
Short Radiolunate Ligament (SRL)	37.5 [37], [39]
Ulnolunate Ligament (UL)	40 [18], [37]
Ulnocapitate Ligament (UC)	50 [18]
Ulnotriquetrum Ligament (UT)	40 [18]
Dorsal Radiocarpal Ligament (DRC)	75 [37], [39]

Table 3.6-1– Extrinsic ligament stiffness values defined for 3D wrist model

Ligament Name	Total Ligament Stiffness (N/mm)
Scaphocapitate Ligament (SC)	40 [18], [37]
Scaphotrapeziotrapezoidal Ligament (STT)	150 [18], [37]
Triquetrocapitate Ligament (TC)	40 [18], [37], [46]
Triquetrohamate Ligament (TH)	50 [18]
Pisohamate Ligament (PH)	50
Transverse Carpal Ligament (TCL)	130 [61]
Dorsal Intercarpal Ligament (DIC)	50 [39]
Schapholunate Interosseous Ligament (SL)	230 [18]
Lunotriquetral Interosseous Ligament (LT)	350 [18], [37], [46]
Pisotriquetral Interosseous Ligament (PT)	100
Trapeziotrapezoidal Interosseous Ligament (TT)	150 [61]
Capitotrapezoidal Interosseous Ligament (CT)	300 [18], [37], [61]
Capitohamate Interosseous Ligament (CH)	325 [61]

Table 3.6-2: Intrinsic ligament stiffness values defined for 3D wrist model

Ligament Name	Total Ligament Stiffness (N/mm)
Carpometacarpal Ligaments	100
Intermetacarpal Ligaments	100

Table 3.6-3: Metacarpal ligament stiffness values defined for 3D wrist model

As previously indicated, ligaments were represented as tension only spring elements in the model. In SolidWorks Motion, this was represented as an action-reaction force vector that spanned between the two defined insertion points for each element. The mechanical properties of the force vectors were defined by a custom FORTRAN code. This code was written as a standard If statement and was dependent on the stiffness, current ligament length and the initial ligament length, as shown in Equation 3.6-1.

$$\mathbf{If((LL)-(LL_0):0,0,St*((LL)-(LL_0)))} \qquad \textbf{Equation 3.6-1}$$

Where, LL = Ligament Length
LL_0 = Zero Ligament Length
St = Stiffness

The real-time ligament length at each time step was measured during a simulation and compared that to the stress free zero ligament length. The zero ligament length was defined as the initial length of the spring element between the two attachment points in the wrist neutral orientation. If the ligament length was greater than the zero length, then a force proportional to the difference would be generated. If the ligament length was equal to or shorter than the zero length, then no force would exist.

Along with the force vectors, each of the elements also included a damper. The damper functioned to prevent rapid changes in length and force during computation which could result in unrealistic results or even convergence failure. A linear damper was applied to all force vectors with a coefficient of 0.25 N-s/mm. While the damping element does slow down changes experienced within the system, it does not affect the final results. However, due to the damping effect, sufficient time must be provided for the results to converge to the final solution. Overall, the only difference seen in the incorporation of the dampers was an increase in the time domain.

3.7 TRIANGULAR FIBROCARTILAGE COMPLEX

The TFCC is a complex structure formed from a combination of different soft tissue bands. It has been described as an extension of the ulnar head and provides a continuous articulating surface with the radial surface for the carpal bones. Functionally, the TFCC can be divided up into two sections. The first is the proximal portion which sits atop the ulnar head and is comprised of the radioulnar ligaments, the articular disc and fibrocartilage meniscus homologue. [35], [40], [50] This portion serves as the articulating surface for the carpal bones and, in essence, has a cradling effect on the triquetrum and the lunate bones. The distal portion of the TFCC serves as an attachment point for a variety of soft tissue structures of the wrist including the ulnar collateral ligament, the FR, ER, the pisiform as well as part of the ECU sheath. This region contains fibers from all these soft tissue structures combining to form a dense and compacted homogeneous tissue structure. It was assumed that while this structure itself may not play a major role in "anchoring" the carpal bones, it most likely plays a significant stabilization function by wrapping around the carpal bones, especially in ulnar deviation motions.

The basic structure of the TFCC was not distinguishable from the CT images of the upper extremity. This is due to the similar density of all the surrounding soft tissue structures. To obtain a basic understanding of the shape and size of structure, anatomical texts and dissection studies were analyzed. However, this did not provide sufficient structural information to allow an accurate rendition of the TFCC. As an alternative resource, the U.S. National Library of Medicine's (NIH, Bethesda, MD) cryoslice images obtained for the Visible Human Project (VHP) were analyzed. For the purposes of this project, the Visible Human Female was analyzed which was formed by 24 bit color cross-sectional images which had equivalent pixel size and

image intervals generating cubic voxels. The image deck was processed within MIMICS. The TFCC was visually identified within the image deck and analyzed to obtain a more structural understanding of the entire structure. This rendition, however, could not be incorporated within the 3D wrist model due to the significant size differences and joint space differences between the referenced specimens. The basic understanding from this analysis was used to generate 3D bodies replicating the TFCC and the functional role it is assumed to play within the wrist.

For the purposes of this model, the TFCC was represented as two distinct structures to accurately replicate the two different roles described above. To recreate the structures in the SolidWorks design space, two 3D body structures were extracted out of MIMICS in a similar manner as previously described for the carpal bones.

For the distal portion of the TFCC, a 3D body was captured and formulated in a similar manner as for the bones. However, this body was formulated to be thicker than it anatomically exists within the joint. The thicker body was created by activating additional pixels on the lateral aspect of the body throughout the mask. This was done to allow SolidWorks to recreate the wrapping, stabilizing role that this portion of the tissue is assumed to play in the human wrist. For the proximal portion of the TFCC, it was formulated in an anatomically correct manner, based on descriptions in the literature and renditions in anatomical texts. Both of these 3D bodies were then imported into the SolidWorks model and positioned in their anatomically correct orientations.

In terms of the proximal TFCC 3D body (Figure 3.7-1), its purpose was to provide an even articular surface on the ulnar aspect for the carpal bones. It was replicated to act as an extension of the ulnar head. Using the RBM method, structures cannot be represented as flexible bodies. All bodies within the system must be defined as rigid incompressible structures.

Anatomically, this proximal portion of the TFCC most likely experiences some deformation during wrist motion. However, to replicate the function of an even surface of the articular joint and its cradling effect on the carpal bones, minimal deformation was assumed. Thus, the proximal TFCC was defined as a rigid body solid structure.

Additionally, in the human wrist joint, the TFCC has soft tissue attachment points to the ulnar head and the radius. While functionally, the TFCC most likely does not move as one unit with the ulnar head, minimal movement with just flexion/extension and radial/ulnar deviation of the carpus was assumed. With forearm pronation/supination, significant motion would occur between the TFCC and the ulnar head due to rotation within the sigmoid notch. In the SolidWorks design space, the radius and ulna are fixed relative to each other, so no such motion can occur. Thus, it can be assumed that the proximal TFCC and the ulnar head function as one unit. To replicate this, the proximal TFCC was fixed to the ulnar head to ensure no motion was experienced relative to the forearm long bones.

In terms of the distal TFCC, it was modeled in a thicker manner than it anatomically exists. This was done to allow the modeling software to calculate contact force and recreate the wrapping stabilizing effect in the model. Anatomically, this portion of the TFCC undergoes significant deformation during the wrist motions. This structure is a complex attachment site for the surrounding ligaments and capsular structures. Tissues from the dorsal/volar and proximal/distal aspect of the wrist blend to form a homogeneous tissue region. It is assumed that this site provides some ulnar side stability due to its wrapping effect around the carpal bones. To replicate this wrapping effect, the distal TFCC modeled body is assumed to be rigid and thus able to impart force on any contacting bone. This body was secured to the proximal TFCC structure with force vectors. These force vectors ensure the anchoring of the distal TFCC base to

the proximal TFCC body yet allow the distal part of the body to move in conjunction with the wrist.

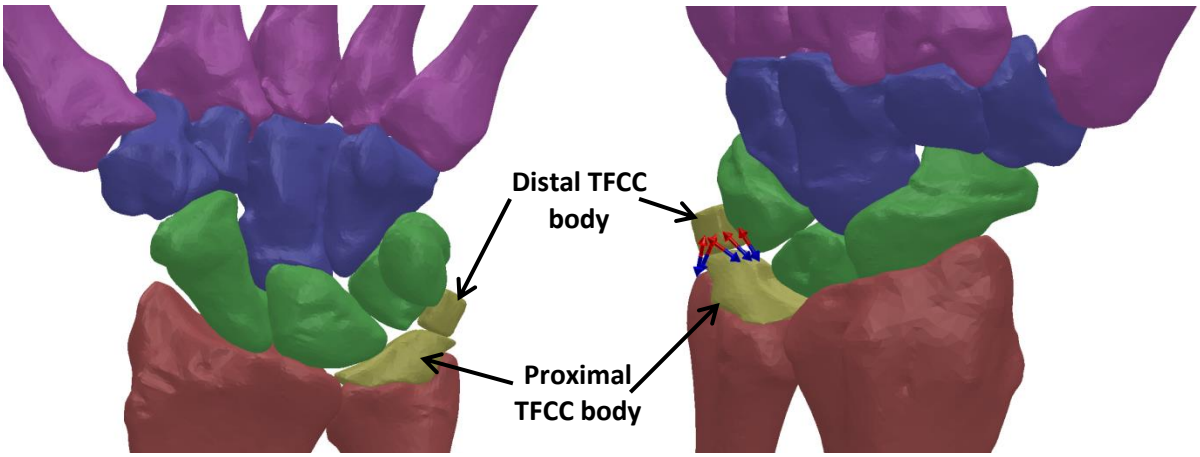

Figure 3.7-1: Palmar (left) and dorsal (right) aspect of the model to show TFCC as a two part structure and the force vectors defined to connect the structures

3.8 CAPSULAR RETINACULAR STRUCTURES

The retinacular structures play a stabilizing role in the wrist joint. As previously described in Chapter 2, this system is comprised of a number of different portions and layers. While in the distal portions, distinct attachment points on the carpal and metacarpal bones can be identified, the proximal portion has been described as more of a continuous sheath that wraps around the distal radial and ulnar head. While the role of these soft tissue structures may not be absolutely clear, it can be assumed that it plays a larger role in stabilization, especially in deficient or injured wrists.

The distal portion of the flexor retinaculum (FR) has distinct attachment points that have been identified and discussed in the literature. This structure has also been extensively studied due to the high interest in the carpal tunnel. When modeling the distal FR, better identified as the transverse carpal ligament (TCL), the structure has attachment points on the lateral side of the hand spanning from the scaphoid tuberosity to the ridge of the trapezium. On the medial aspect of the hand, the ligament attaches to the pisiform and the hook of hamate. Thus, this structure was modeled as a simple linear spring element as described for all the other ligaments. Four attachment points were identified on the carpal bones based on anatomical descriptions. The structure was represented with four force vectors with each attachment point being used for two different spring elements. Two of the spring elements spanned horizontally, while the other two spring elements spanned diagonally crossing the palmar aspect of the carpus (Figure 3.8-1).

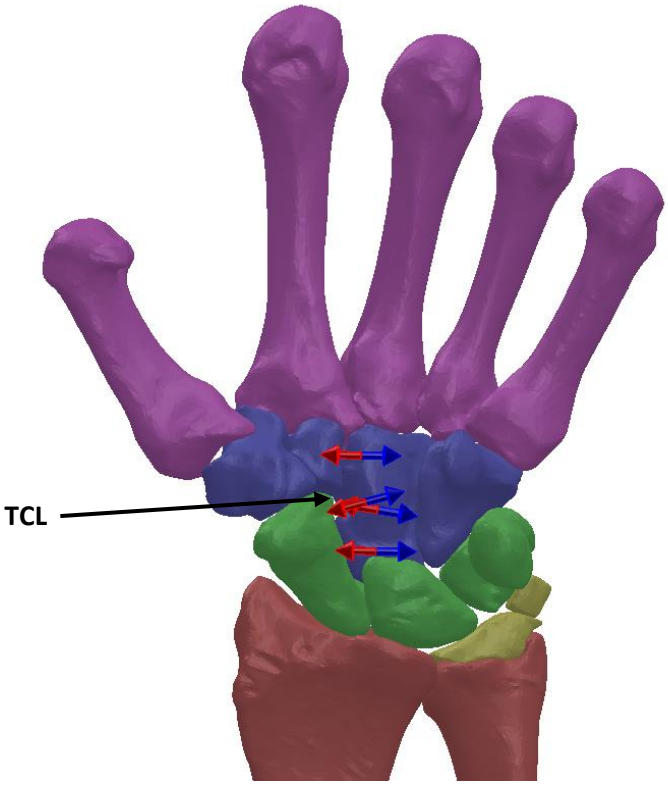

Figure 3.8-1: Modeling of TCL (distal FR) on palmar aspect of wrist

The proximal portions of the FR and extensor retinaculum (ER) do not have any distinct insertion points on the carpal bones. However, these do encapsulate the proximal row of the carpal bones and thus play a role in stabilization by wrapping around the bones. This band of tissue also encapsulates most of the tendons and other muscular and fatty tissue. Thus, the combined mass of tissue cups around the carpal bones and most likely provides some stability to this region of the joint.

To accurately replicate this effect, solid body structures were incorporated into the model (Figure 3.8-2 and Figure 3.8-3). Four solid bodies, two for the palmar aspect and two for the dorsal aspect, were captured out of MIMICS in a similar fashion as described for the TFCC. These structures were created to closely conform to the surface geometry of the bones across the radiocarpal joint. Once these structures were incorporated within the SolidWorks design space,

linear spring elements were used to tether the two palmar structures and the two dorsal structures to each other (Figure 3.8-2 and Figure 3.8-3). In the human hand, the retinacular structures have attachment points on the radial styloid process and the ulnar styloid process. On the distal lateral portion, fibers from these soft tissue structures also embed into the TFCC as well as the pisiform. On the distal medial aspect, while there are no bony attachment points, the fibers from the FR and the ER integrate to form a continuous structure. In the model, spring elements were included in a similar manner to recreate this wrapping effect.

Due to the unique method of modeling rigid bodies in SolidWorks, the four FR and ER structures were modeled in an anatomically modified manner. As previously discussed, SolidWorks measures 3D contact force by calculating the volumetric overlap between bodies during each simulated time step. With very thin structures, SolidWorks may not be able to accurately model 3D body contact due to the low volume which could lead to dramatic and unintended results. Thus, when these structures were formulated within MIMICS, they were modeled to be thicker than they anatomically exist. This was done for the same reason as for the distal TFCC body. By modeling these structures in this manner, they were capable of imparting lateral contact forces when the carpal bones interacted with them. However, this increased thickness may also unnaturally affect the kinematic response of the wrist through its range of motions. To minimize discrepancies due to these bodies, 3D contact with these structures was selectively assigned. 3D contact was defined to exist only between the bones and the FR and ER structures. No 3D contact existed between the individual capsular structures themselves. This ensured that the only affect experienced by the wrist with the addition of these elements was the wrapping effect on the carpal bones.

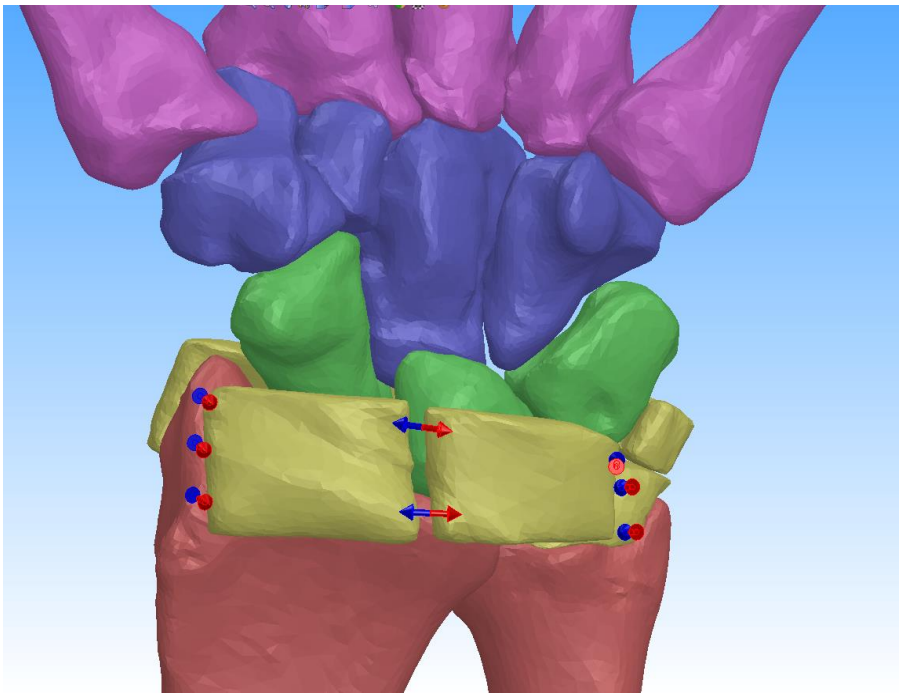

Figure 3.8-2: Flexor retinacular capsular structures in the wrist joint model.

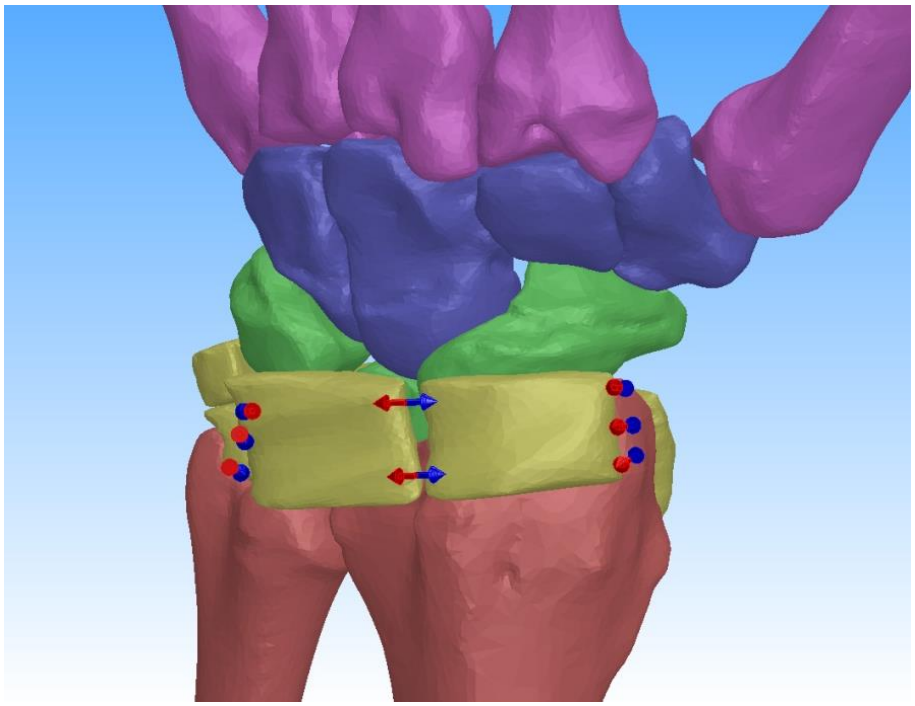

Figure 3.8-3: Extensor retinacular capsular structures in the wrist joint model.

3.9 WRIST MUSCLES

The wrist has six main muscles that govern its motion. As previously mentioned in Chapter 2, the APL has a secondary function in wrist motion and was not modeled in any of the studies covered in this work. The five wrist muscles represented were the ECRL, ECRB, ECU, FCR, and FCU. In the first experimental study, the ECRB was not simulated. In the second experimental study, the ECRL and ECRB were sutured together during testing and thus were considered as one unit. The insertion points of these muscles were obtained from anatomical texts and similarly marked with points on nodes on the triangular mesh of the respective bone. Each tendon was modeled with two straight line force vectors representing the lateral and medial aspects of the tendon. In this case, the force vectors were represented as constant magnitude force vectors.

One of the main limitations of SolidWorks is the inability to model wrapping of elements around structures. This proved to be especially challenging when modeling tendons. Tendons experience dramatic changes in their line of action when a joint goes through its range of motion. Thus, simply modeling the tendon with a straight line vector connecting the origin and insertion of the respective muscle was not sufficient. In this case, some further modifications were needed in order to accurately maintain the line of action of the muscle.

As discussed in Chapter 2, the retinaculum acts as a pulley for the tendons crossing the wrist joint. Thus, it was determined that by defining the force vector to exist between the wrist bone insertion point and the region where the tendons cross the retinaculum, the line of action may sufficiently be preserved for modeling purposes. To achieve this, the distal tendons were located in the CT scans for the muscles of interest and identified using anatomical text books (Figure 3.9-1). Once located, the tendons were then extracted in a similar manner as the carpal

bones and then incorporated into the SolidWorks assembly. Then points were defined on the tendon bodies that lay approximately on the proximal termination point of the flexor or extensor retinaculum. Once these points were identified, force vectors were incorporated that connected these attachment points (Figure 3.9-2 and Figure 3.9-3). As with the ligaments, each of these force vectors also included a damping element to prevent rapid motion changes during the simulation. During each study, a constant magnitude of force was applied to determine the overall effect in the kinematics of the wrist joint.

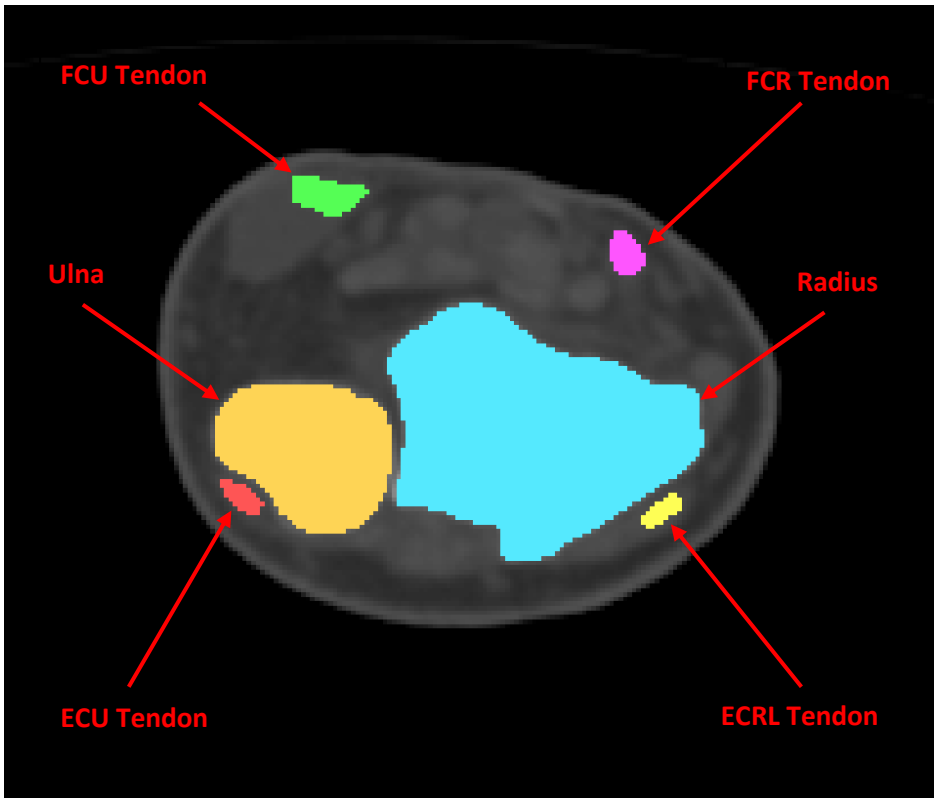

Figure 3.9-1: Selection of muscle tendon masks in MIMICS.

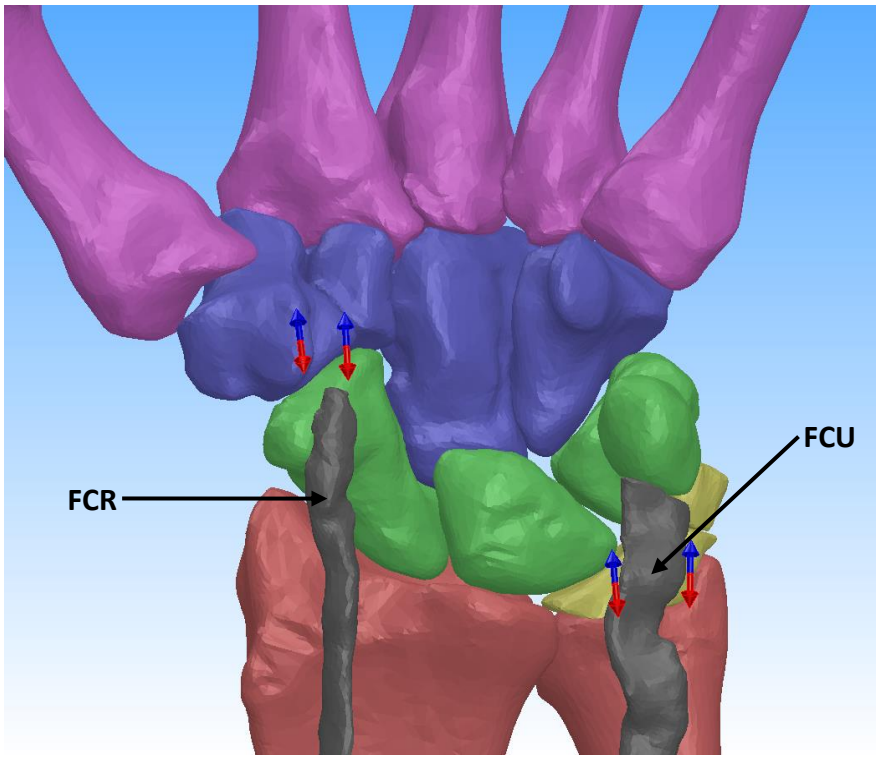

Figure 3.9-2: Flexor muscle simulation with constant force vectors.

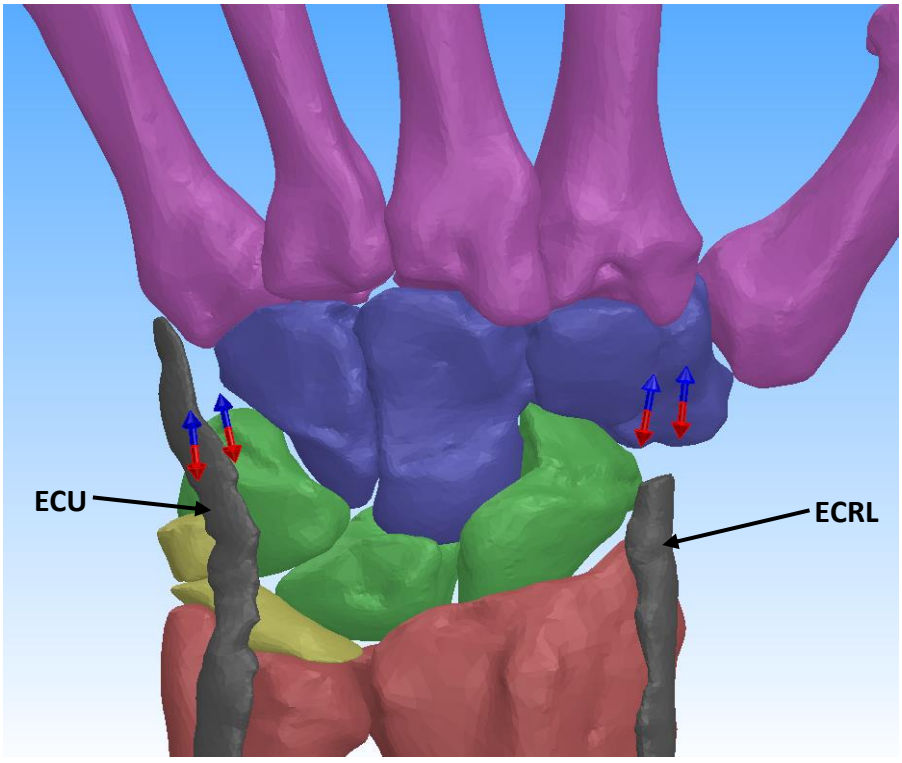

Figure 3.9-3: Extensor muscle simulation with constant force vectors.

3.10 Complete 3D Wrist Model

The complete 3D wrist model was formulated as described throughout this chapter (Figure 3.10-1). The bones and articular surfaces were accurately captured and replicated based on CT images of a joint specimen. The ligaments of the wrist were modeled to mimic mechanical properties determined from experimental studies reported in the literature. The less clearly understood TFCC and retinacular capsular structures were recreated to play the roles that they are assumed to play in wrist stability. Finally, the wrist muscles were represented in a modified manner to allow the application of force simulating muscle contraction.

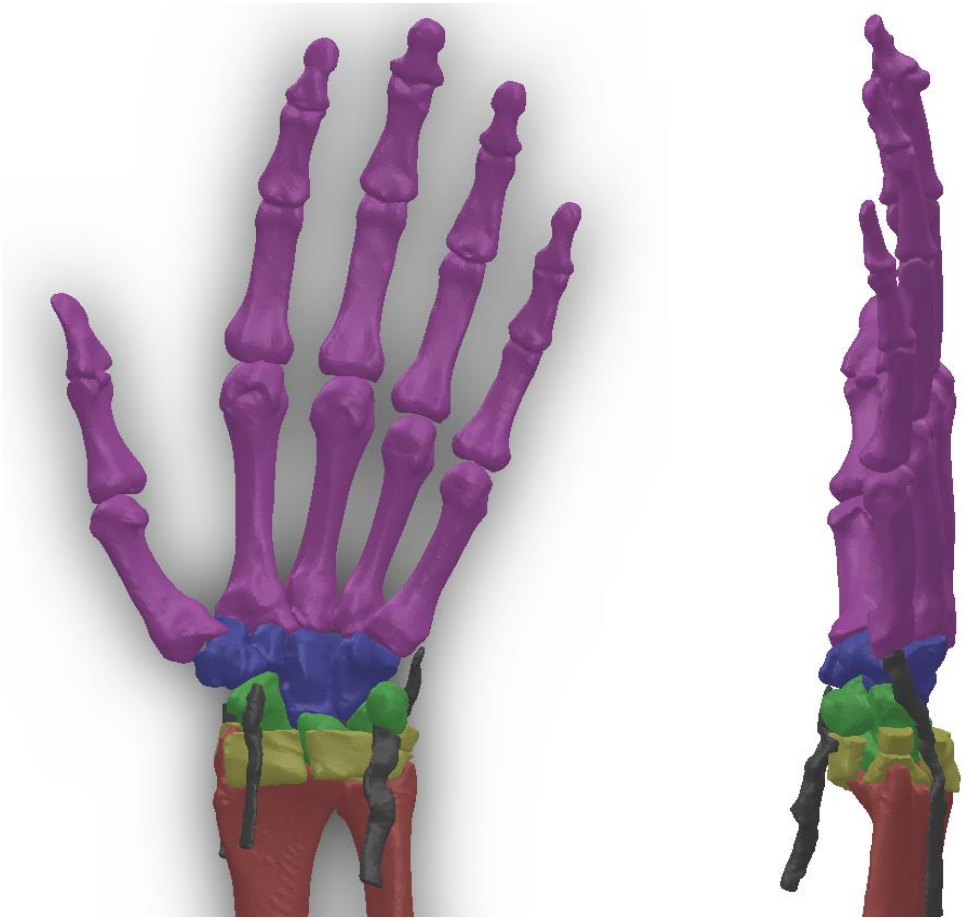

Figure 3.10-1: SolidWorks Assembly of the 3D Wrist Model (Ligament force vectors not shown).

CHAPTER 4: RSL RANGE OF MOTION VALIDATION STUDY

4.1 OVERVIEW

The three-dimensional rigid body wrist model was first validated against a cadaveric experimental study conducted by Pervaiz et al, which analyzed the effects on the kinematics of the wrist following radioscapholunate (RSL) fusion and carpal bone excisions. [32] The first version of the 3D wrist model developed by Majors et al [30] was also validated against this experimental study. For the purpose of this work, the cadaveric experiment was only partially replicated to demonstrate the reproducibility of the results between the original and updated 3D wrist model. In this study, only the range of motion for the intact, normal wrist and the wrist with a RSL fusion procedure were simulated.

RSL fusion is a surgical procedure used for the treatment of radiocarpal arthritis which may result from cartilage degeneration or following incongruent healing of articular bone fractures. This treatment option is designed to alleviate the RSL joint pain and stiffness while still preserving some wrist joint motion [32] It is usually performed when more conservative options are unable to relieve the pain or stiffness experienced in the joint.

4.2 RSL WRIST RANGE OF MOTION STUDY

The experimental study conducted by Pervaiz et al will be briefly summarized. The radius and ulna of ten fresh-frozen, upper extremity cadaveric specimens were secured in the testing apparatus (Figure 4.2-1). Physiological motion of the joint was achieved by loading the four major muscles of the wrist: the FCR, the FCU, the ECRL and the ECU. Flexion was

achieved by loading the FCR and FCU, extension achieved through the ECRL and ECU, radial deviation achieved by loading FCR and ECRL, and ulnar deviation achieved by loading of the ECU tendon. Weights (5 lbs.) were applied to each tendon to simulate muscle contraction.

The range of motion in a respective plane was determined by measuring the angle between the long axis of the radius and the long axis of the third metacarpal via strategically placed markers on the bones. Two-dimensional digital images were taken in the coronal plane for flexion-extension motion and from the sagittal plane for radial-ulnar deviation. These images were processed in a standard imaging software to measure the angle between the markers and provide the motion arcs for the wrist. Each specimen was tested in four different experimental states: intact normal, RSL fusion, RSL fusion with distal scaphoid pole excision, and RSL fusion with distal scaphoid pole excision and triquetrum excision (Figure 4.2-2).

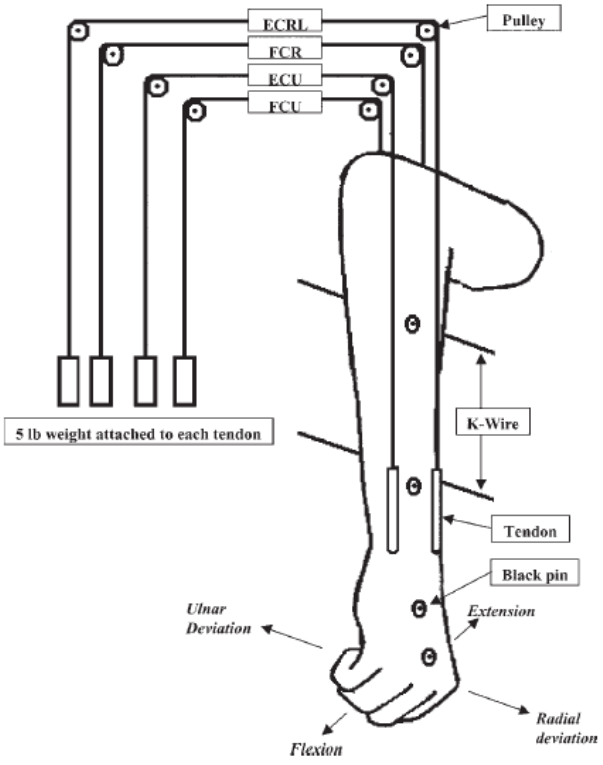

Figure 4.2-1: Schematic of testing set up used in the study by Pervaiz et al. [32]

Figure 4.2-2: Radiograph images of wrist with RSL fusion (A), RSL fusion and scaphoid distal pole excision (B), and RSL fusion, scaphoid distal pole excision and triquetrum excision (C). [32]

4.3 COMPUTATIONAL MODELING OF RSL RANGE OF MOTION STUDY

The original 3D wrist model developed by Majors et al [2] replicated the wrist range of motion experimental study in its entirety. With the current 3D wrist model developed through this work, only the intact state and RSL fusion state were simulated to validate the model and demonstrate reproducibility of the predictions between the models before new surgical studies were investigated.

In the experimental study, the forearm was fixed to the testing apparatus and the limb was positioned vertically with the wrist pointing down. This was replicated in the model by fixing the radius and ulna within the design space and constraining these bones from experiencing any motion. All the remaining bones were free to move in response to perturbations, soft-tissue restraints and solid body contact experienced between the structures, as previously described in Chapter 3. The exception to this was in the third metacarpal, which was fixed to the capitate, since these two bones essentially move as a single unit. [24] Since there was no interest in the individual finger motions, all five groups of phalanges were also fixed relative to the respective

metacarpal bone. Additionally, an external force was applied to the wrist parallel to the coronal plane pointing along the distal axis of the arm to replicate the gravitational force experienced by the limb during the experimental study (Figure 4.3-1). A native tool exists within SolidWorks Motion which simulates the effect of gravity on individual parts or at the assembly level within the design space. Once the direction of action was defined, the tool applies a linear acceleration to the centroid of each body within the assembly to replicate gravitational effects.

Figure 4.3-1: Wrist model with radius and ulna fixed and gravity defined (green arrow) for RSL Fusion study

In the experimental study, no surgical alterations were performed to the specimens in the intact state. Thus, all the structures described in Chapter 3 were included in the wrist model for the simulation of this part of the study. To replicate the 5 lb weight applied to the tendons during

the experimental study, constant force vectors with a total magnitude of 22.24N were applied to each respective tendon in the wrist model. To achieve the motion arcs in the wrist model, the FCU and the FCR were loaded for flexion, the ECU and ECRL for extension, the FCR and ECRL for radial deviation and the ECU loaded for ulnar deviation.

Once testing was simulated in all four motions in the intact state, adjustments were performed on the wrist model to accurately replicate the RSL fusion state achieved in the experimental study. The carpal bone fusion was replicated by utilizing the "mate" tool native to SolidWorks in which the scaphoid and lunate were locked in their neutral orientation relative to the radius. This prevented any motion of these bones during simulations (Figure 4.3-2) and essentially eliminated motion at the radiocarpal joint. All the remaining bones and structures of the wrist were free to move as previously defined. Once this fusion state was achieved, the motion studies were carried out in an identical manner as described for the intact state to examine the observed changes in the range of motion angles.

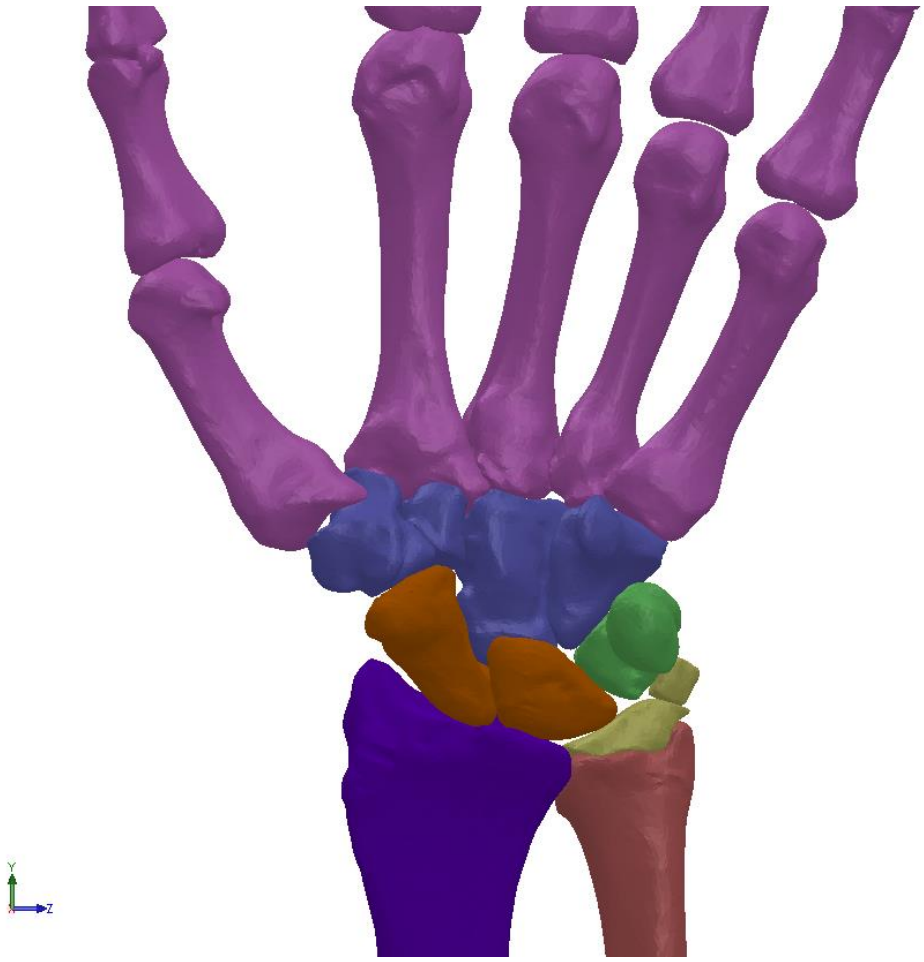

Figure 4.3-2: Simulated fusion of scaphoid and lunate to radius (Capsular structures hidden for clarity).

4.4 RESULTS

In the experimental cadaveric study conducted by Pervaiz et al, the angles of motion were measured from 2D images taken in the coronal plane for flexion/extension and images in the sagittal plane for radial/ulnar deviation. Angles were measured between markers placed along the long axis of the radius and the third metacarpal. A comparable approach was taken to measure the motion angles in the computational model. First the long axis of the radius and the third metacarpal were defined based on anatomical landmarks and definitions provided by ISB [63] and as discussed in Chapter 3. The angle formed between these two reference lines is the most widely accepted method of determining global wrist joint angle. However, the experimental study measured wrist angles from a 2D perspective. Thus, the 3D angles formed between the axes of the bones within the computational model were processed to reflect a 2D perspective of the motion of interest. To achieve this, for flexion and extension, a projection of the wrist coronal plane was created upon which two lines were drawn and defined to be parallel to the long axis of the radius and the third metacarpal (Figure 4.4-1). These lines traced the motions of the long axes in a 2D manner and thus, the angles between these lines could be tracked to determine the flexion/extension motion angle of the wrist joint during a simulation (Figure 4.4-3). For radial/ulnar deviation a similar method was employed, but in this case a projection of the wrists sagittal plane was created (Figure 4.4-2) and the angle between the defined lines was traced to give the joint motion angle (Figure 4.4-4).

Validation of the 3D wrist model was carried out against the four range of motion results obtained in the two different states (intact normal and RSL fusion) of the cadaveric experimental study. These results were further compared with the wrist motions predicted by the computational model developed by Majors et al (Figure 4.5-1 – Figure 4.5-4). [30]

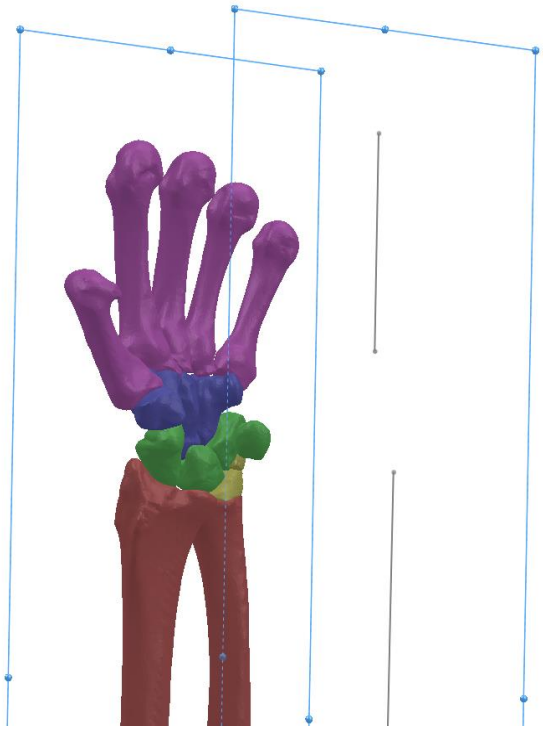

Figure 4.4-1: Projected coronal plane to measure wrist flexion/extension angles (Capsular structures hidden for clarity).

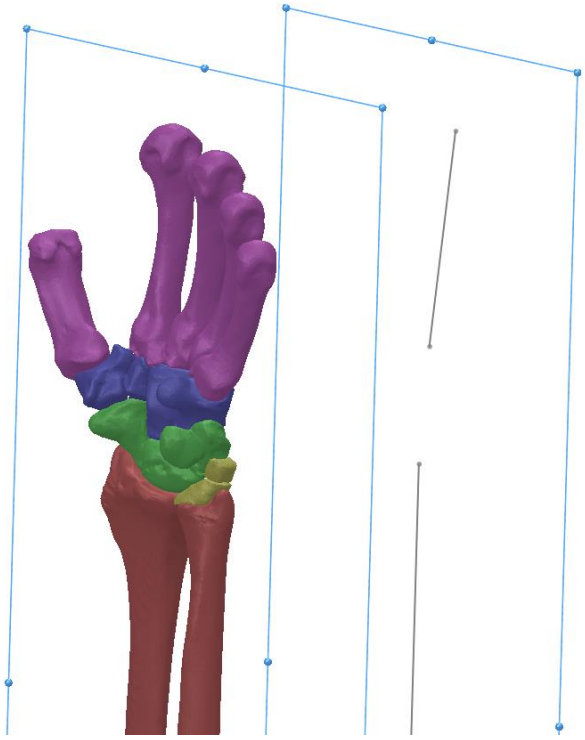

Figure 4.4-2: Projected sagittal plane to measure wrist radial/ulnar deviation angles (Capsular structures hidden for clarity).

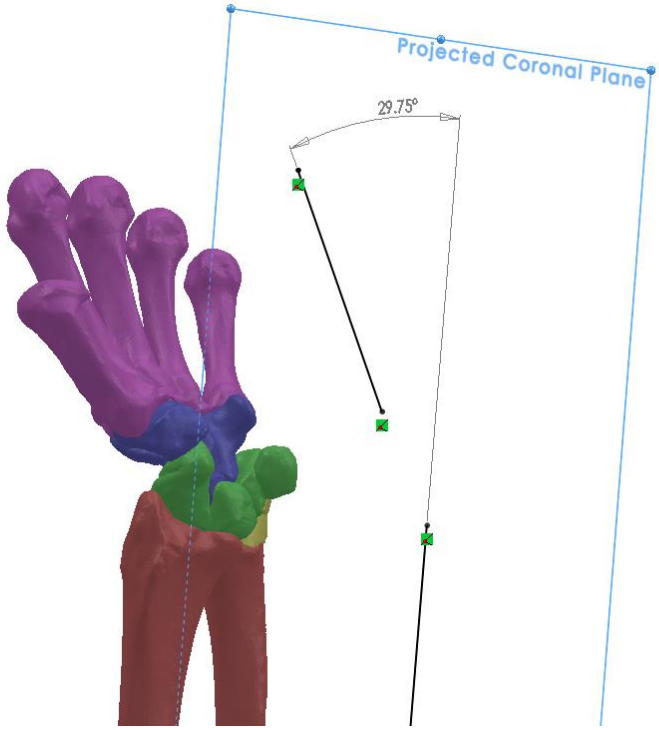

Figure 4.4-3: Extension angle measured between long axis of radius and third metacarpal (Capsular structures hidden for clarity).

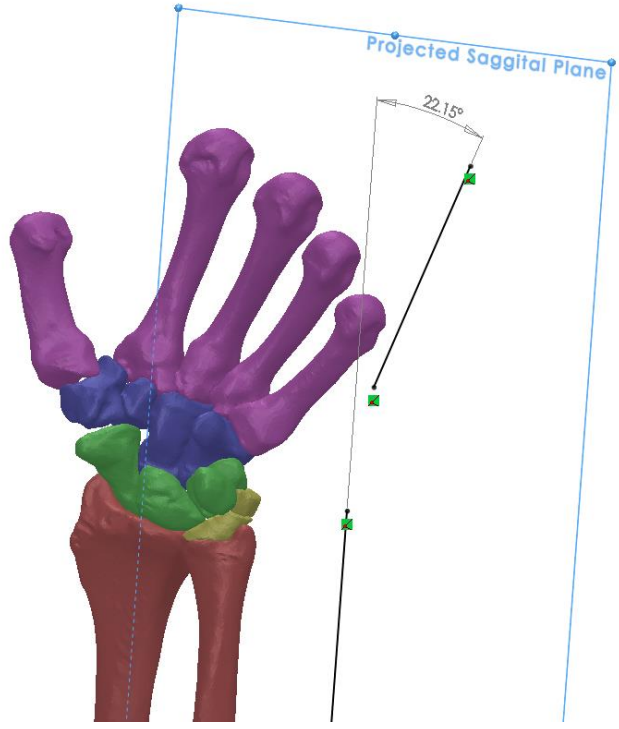

Figure 4.4-4: Ulnar Deviation angle measured between long axis of radius and third metacarpal (Capsular structures hidden for clarity).

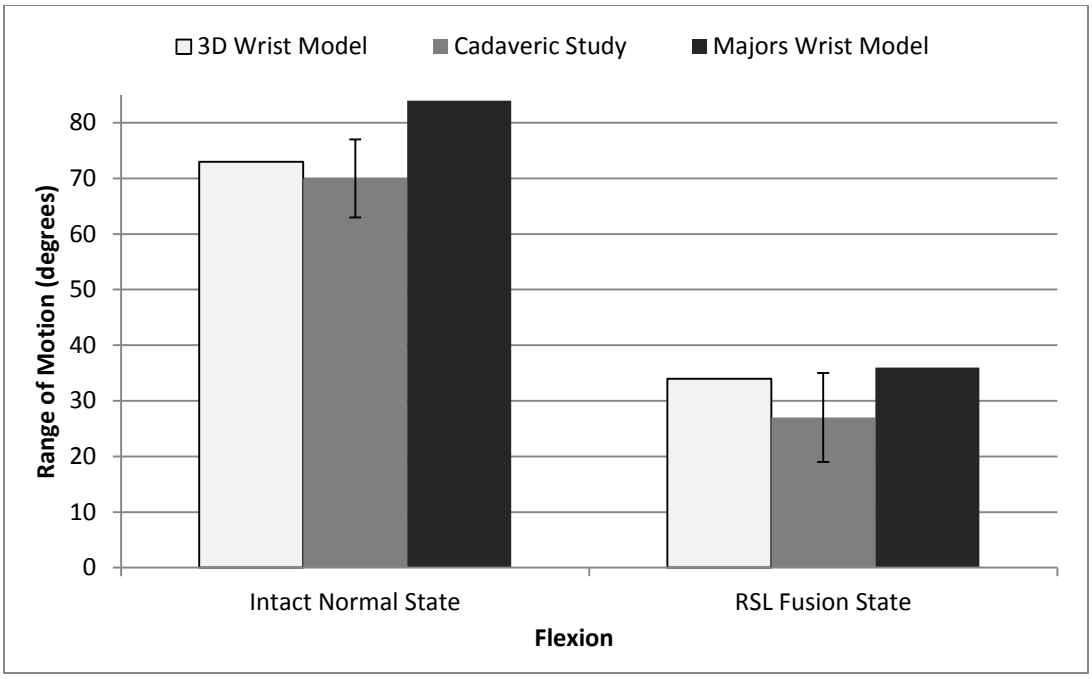

Figure 4.5-1: Range of motion obtained during flexion in 3 studies.

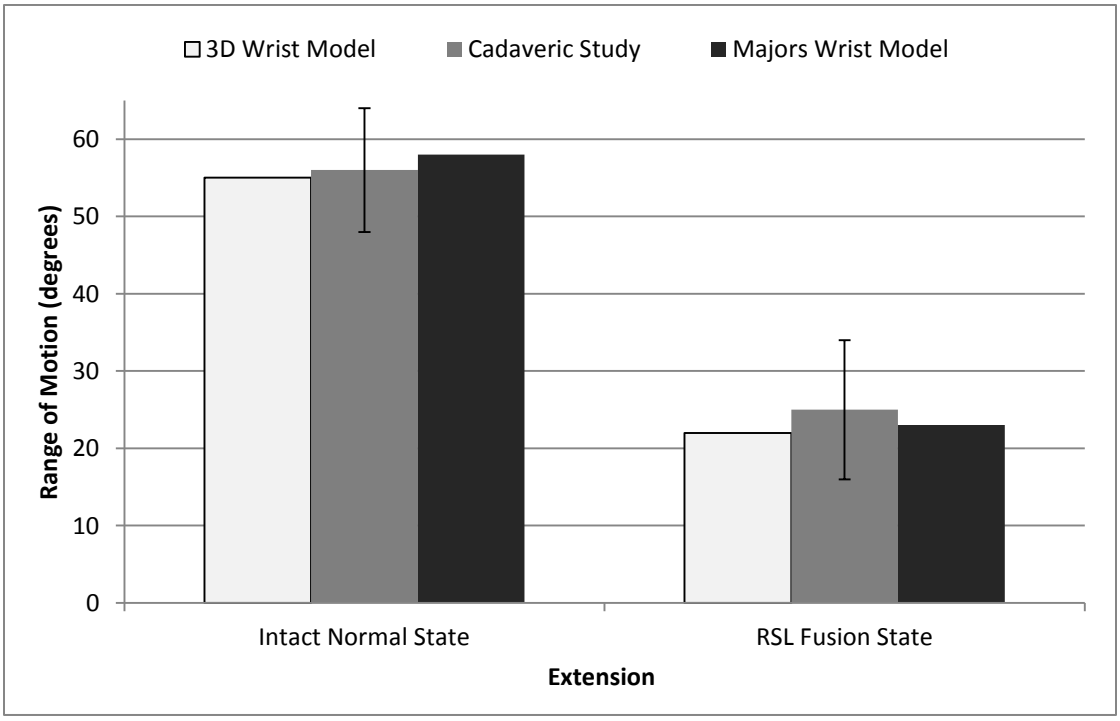

Figure 4.5-2: Range of motion obtained during extension in 3 studies.

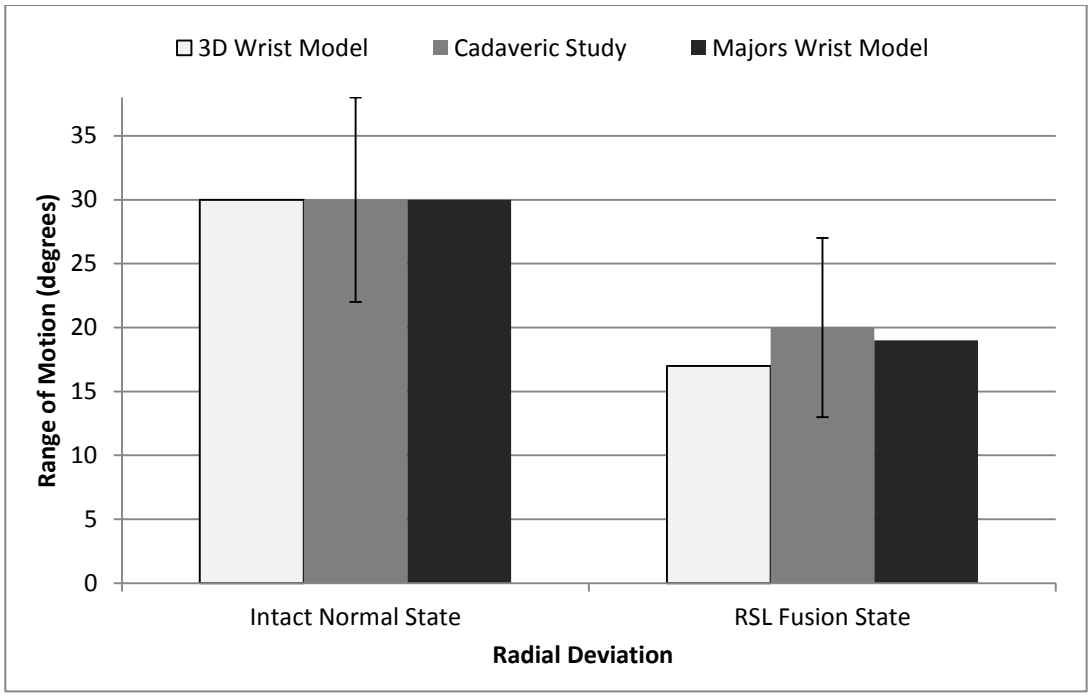

Figure 4.5-3: Range of motion obtained during radial deviation in 3 studies.

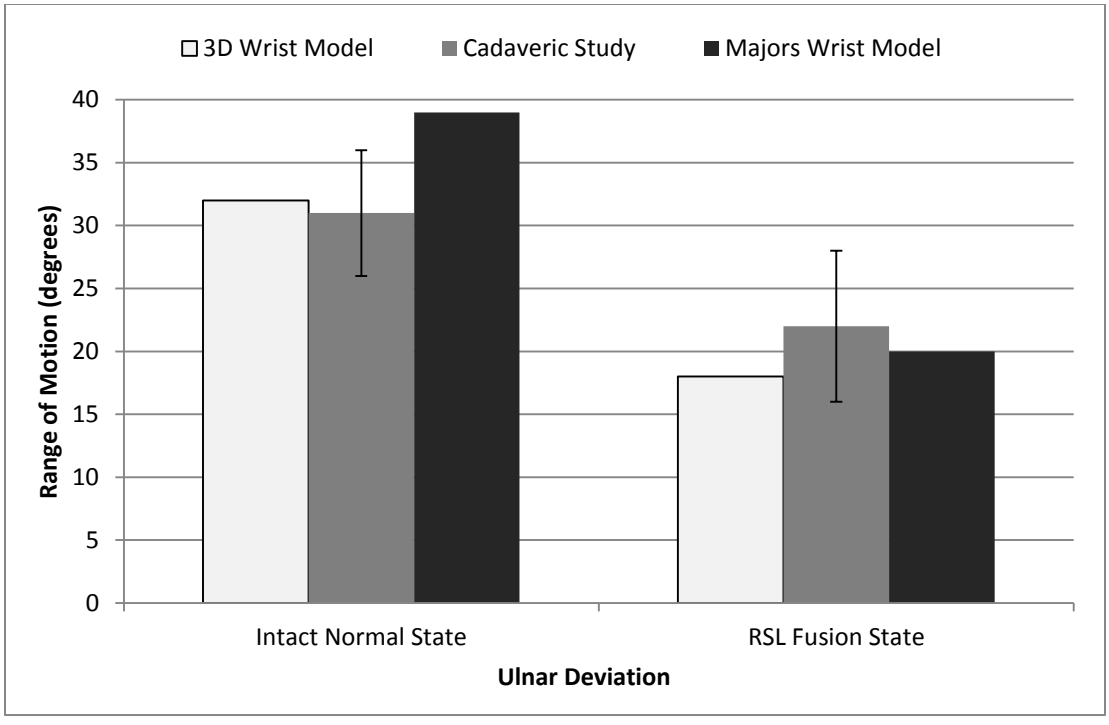

Figure 4.5-4: Range of motion obtained during ulnar deviation in 3 studies.

A summary of the range of motion angles predicted by the 3D wrist model in comparison to the cadaveric experimental study and Majors wrist model (Table 4.5-1) demonstrates excellent correspondence. For both the intact and RSL fused states, the 3D wrist model was able to accurately reproduce the angles obtained in the experimental study in each of the planes of motion. Additionally, the model also provided more accurate predictions than those provided by Majors wrist model which overestimated motion in certain planes.

		Intact Normal State	RSL Fusion State
Flexion	3D Wrist Model	73^o	34^o
	Cadaveric Study	70^o	27^o
	Majors Wrist Model	84^o	36^o
Extension	3D Wrist Model	55^o	22^o
	Cadaveric Study	56^o	25^o
	Majors Wrist Model	58^o	23^o
Radial Deviation	3D Wrist Model	30^o	17^o
	Cadaveric Study	30^o	20^o
	Majors Wrist Model	30^o	19^o
Ulnar Deviation	3D Wrist Model	32^o	18^o
	Cadaveric Study	31^o	22^o
	Majors Wrist Model	39^o	20^o

Table 4.5-1: Range of motions obtained in three separate studies.

One of the advantages of computational simulation is the ability to measure a wide range of different parameters, many of which may be very difficult or impossible to determine in an actual living or cadaveric specimen. A parameter of particular interest to researchers is the force generated within each ligament and the changes observed between different wrist motions and

surgical states. For both states, the change in tension generated in the scaphocapitate ligament was compared between the four motions (Figure 4.5-5 and Figure 4.5-6). It was observed that in multiple motion arcs no force is generated while 21 N of force is measured in radial deviation for the intact wrist. Additionally, the change in tension in the ligament follow a similar trend between the motions in both states, except in RSL fusion a lower overall force is observed and small amount of force is generated in extension.

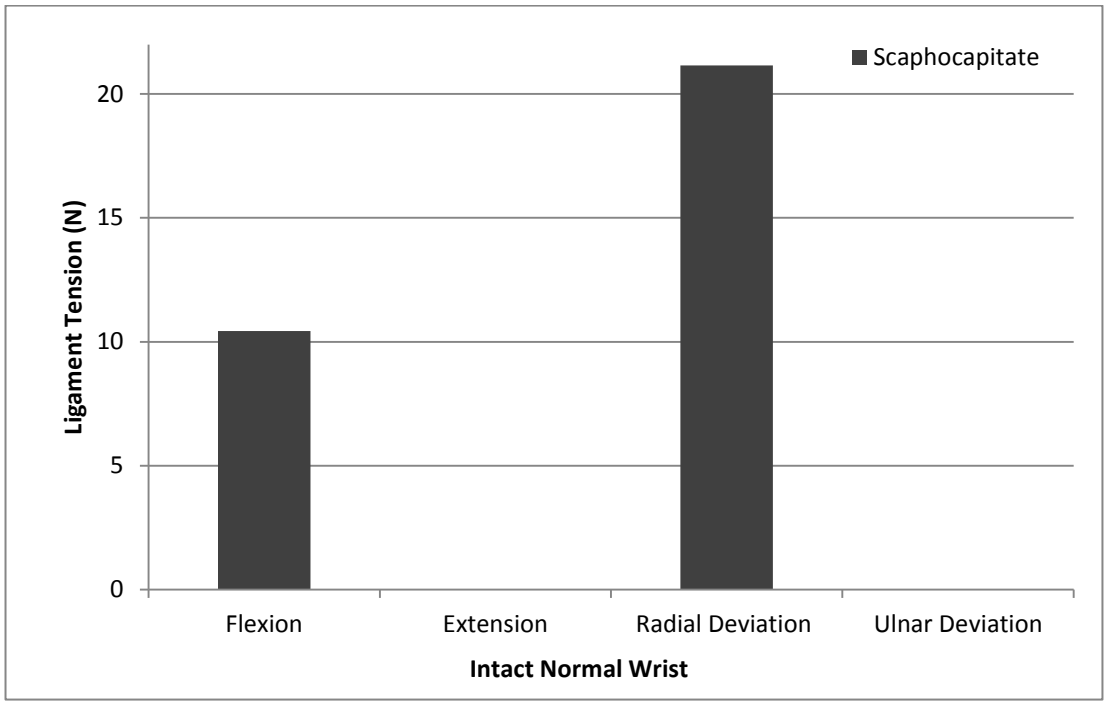

Figure 4.5-5: Tension generated in Scaphocapitate ligament in Intact Wrist.

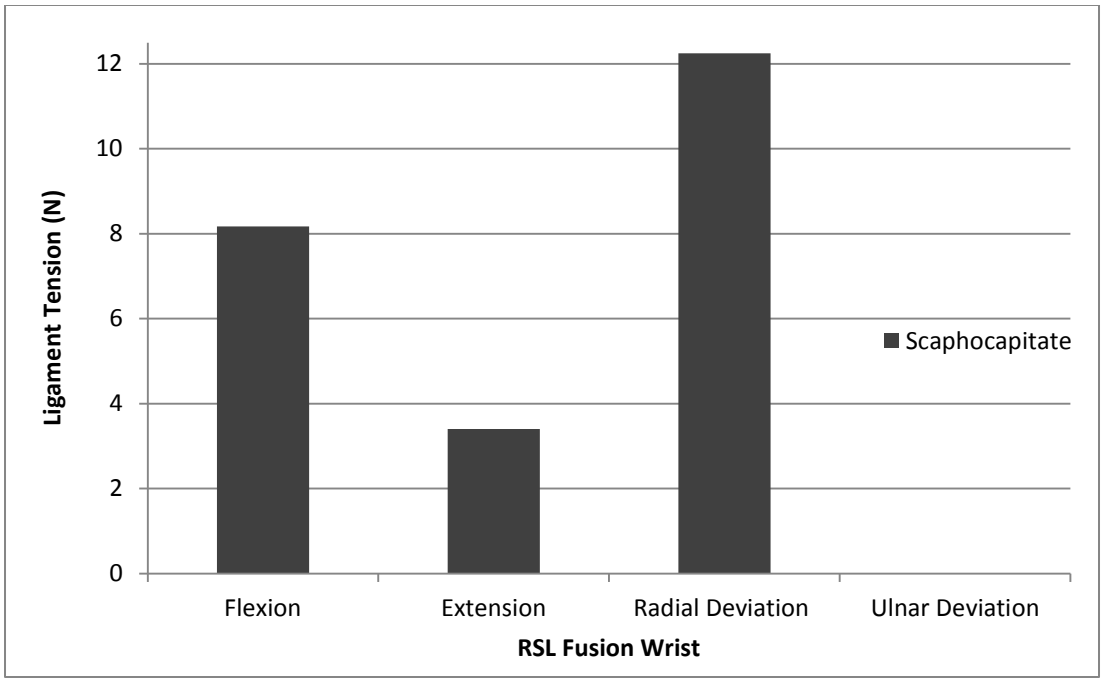

Figure 4.5-6: Tension generated in Scaphocapitate ligament in RSL Fusion Wrist.

Additional measurements were made to determine the changes in tension observed within particular ligaments. A comparison of the changes in force observed pre- and post-operatively was conducted for all four wrist motions (Figure 4.5-7 – Figure 4.5-11). In flexion, a dramatic drop in the DRC tension and an increase in the TC and DIC tension is observed in post-op. In extension, large drops in ligament tension is observed in the RC and UL ligaments and new force is generated in the SC ligament. In radial deviation, minimal changes occur in UT, a drop in tension is observed in SC and force is generated in UC post-op. Finally, in ulnar deviation, a drop in tension generation is observed in both the STT and the DIC ligaments.

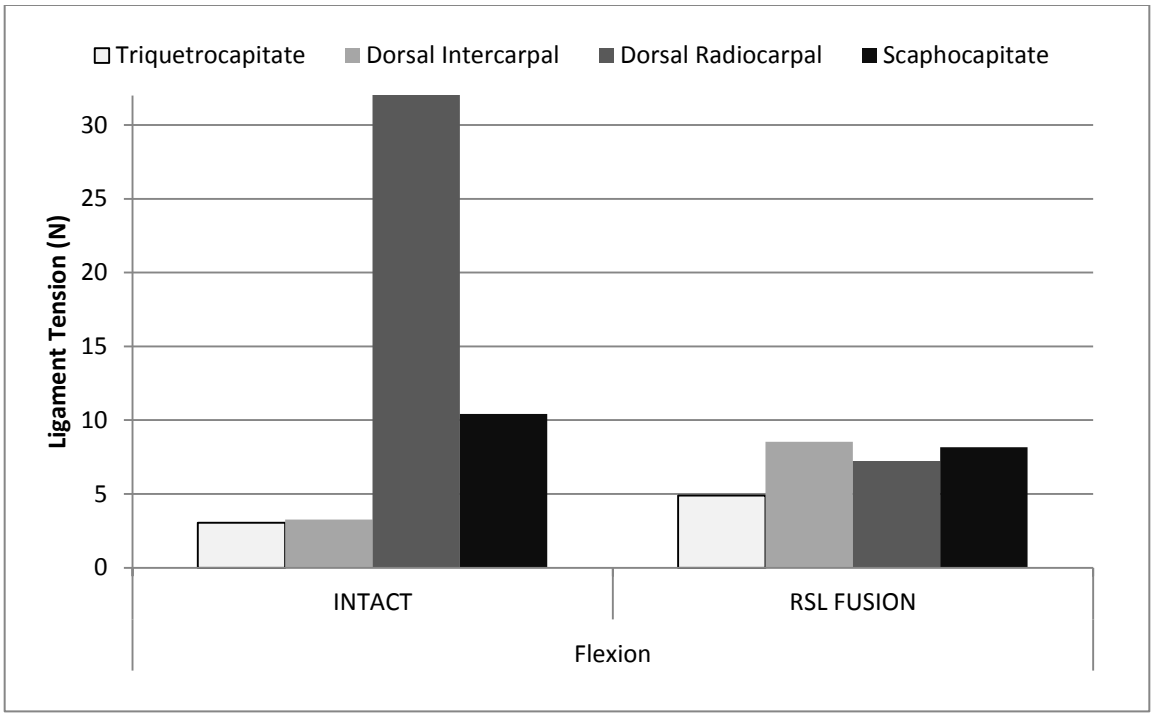

Figure 4.5-7: Comparison of tension generated in wrist ligaments during flexion.

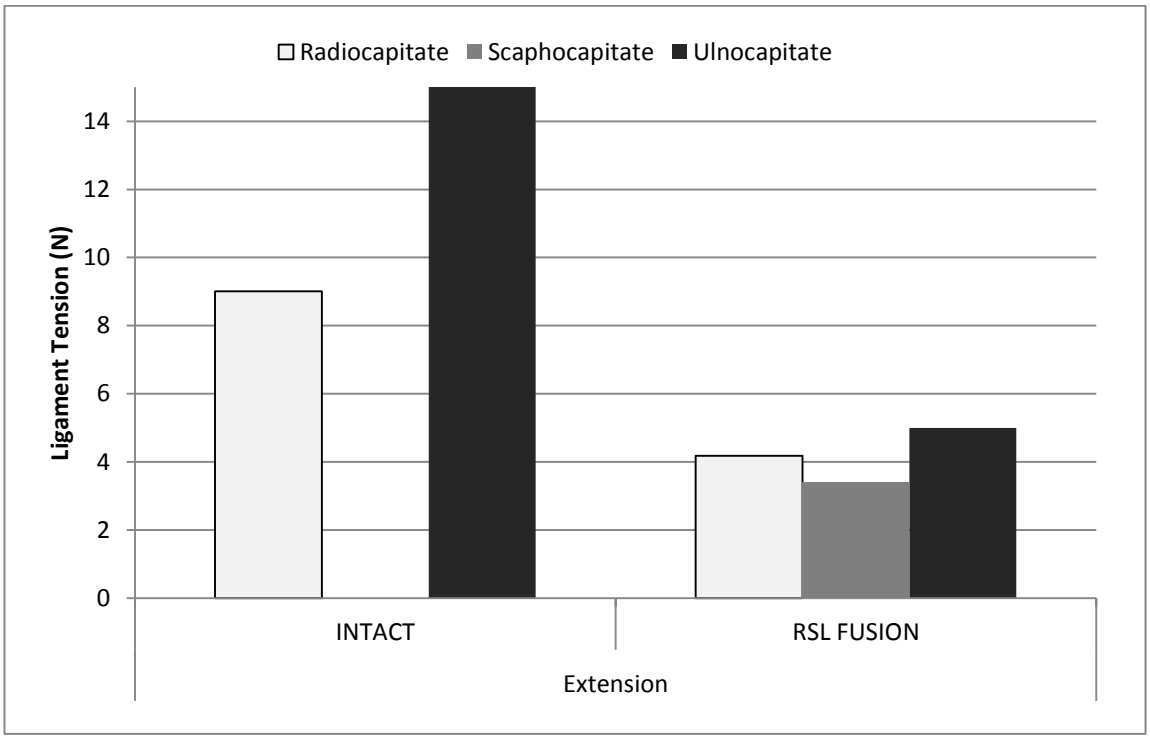

Figure 4.5-8: Comparison of tension generated in wrist ligaments during extension.

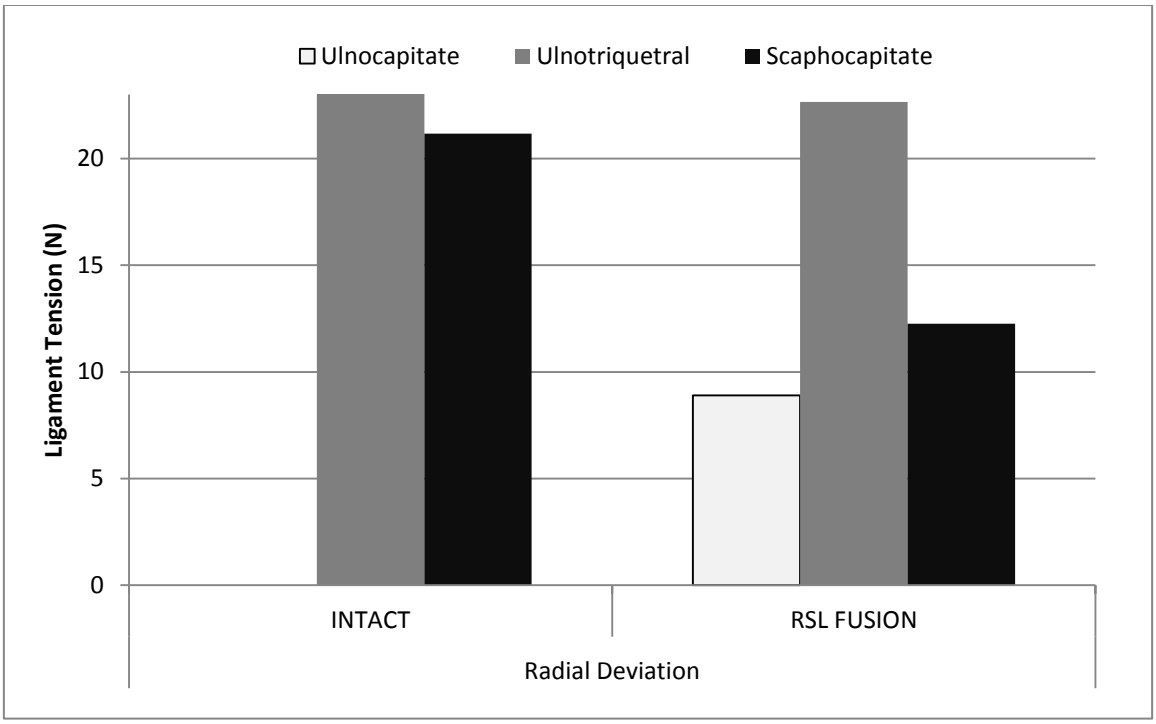

Figure 4.5-9: Comparison of tension generated in wrist ligaments during radial deviation.

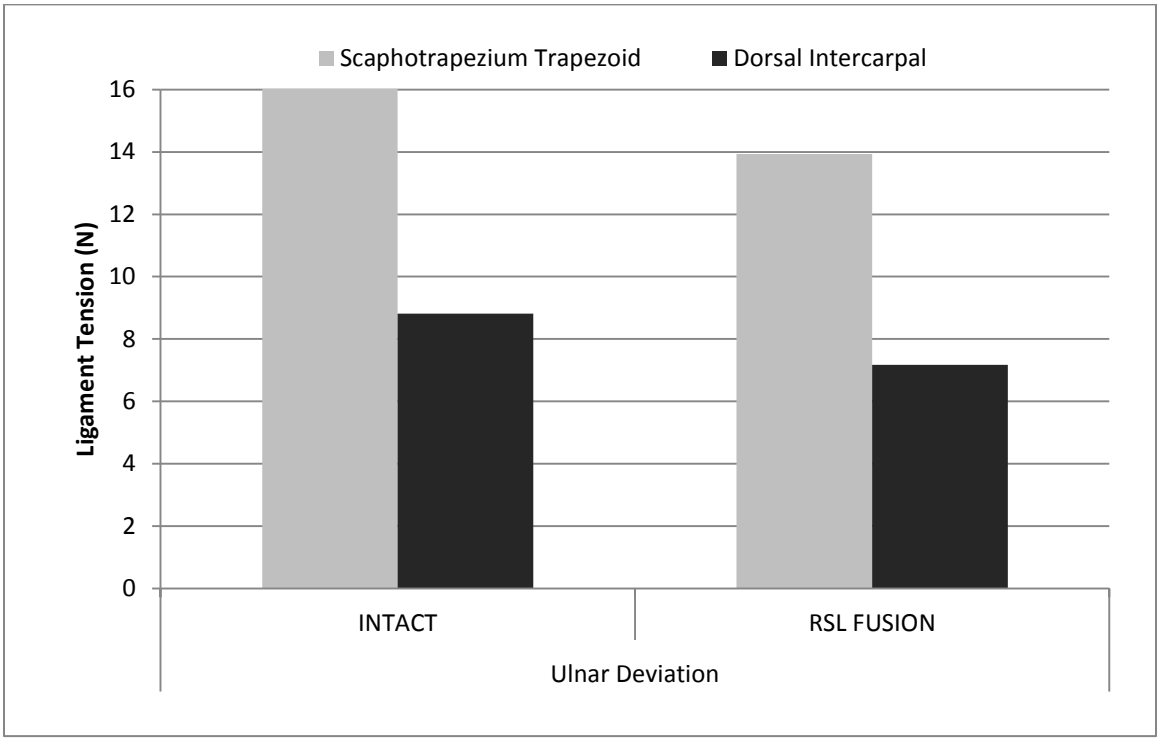

Figure 4.5-10: Comparison of tension generated in wrist ligaments during ulnar deviation.

CHAPTER 5: BIOMECHANICS OF THE WRIST FOLLOWING PROXIMAL ROW CARPECTOMY

5.1 OVERVIEW

Following the validation of the experimental range of motion study by Pervaiz et al, two additional experimental studies were replicated with the three-dimensional (3D) wrist model. Both studies investigated the biomechanical effects of a proximal row carpectomy (PRC) procedure on the human wrist joint. The first study, by Blankenhorn et al, [33] looked at the effects on carpal kinematics while the second study, by Tang et al, [34] compared the changes in contact biomechanics in a wrist following a PRC procedure. Both these experimental studies were conducted within the same laboratory utilizing a similar testing apparatus and methodology.

The cadaveric experimental studies conducted this motion sparing surgical procedure which is used as a treatment for certain advanced wrist degenerative conditions. PRC has been found to be a clinically useful treatment for conditions such as scapholunate advanced collapse, scaphoid nonunion advanced collapse, chronic perilunate dislocation and Kienbock's disease. While clinical studies have shown that a wrist demonstrates a decreased range of motion following PRC, [71–73] the procedure has been found to have fewer complications, can be easier to perform and provides similar grip strength and greater pain relief as compared to limited wrist arthrodesis. [33]

5.2 PROXIMAL ROW CARPECTOMY EXPERIMENTAL STUDIES

In the experimental study conducted by Blankenhorn et al, eight fresh-frozen cadaveric upper extremities were prepared by removal of all soft tissue overlaying the middle third of the long forearm bones. Care was taken not to damage the interosseous membrane and the major wrist muscle tendons. Each specimen was secured onto a testing apparatus (Figure 5.2-1) in neutral forearm orientation by bolting the radius and the ulna. Each of the tendons of interest were sutured and attached to spring loading scales on the testing fixture. The tendons of interest were the FCU, FCR, ECU, ECRL, and ECRB. However, to simplify the procedure, the ECRL and ECRB were tied and sutured together to one loading scale and treated as a single unit.

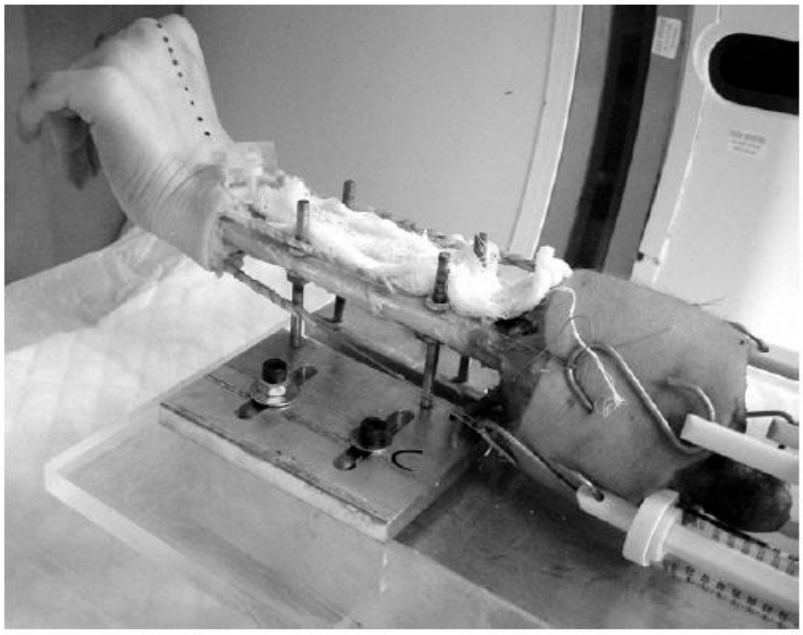

Figure 5.2-1: Testing fixture to hold and test cadaveric specimens during PRC studies. [33]

Each specimen was tested in flexion, extension, radial deviation and ulnar deviation. These motions were achieved by manually varying the force applied by each spring scale to the four tendons. Each tendon was loaded with forces between 5 and 50N to achieve the desired

position of the wrist joint. Once a targeted angle was obtained, the spring scale cables were clamped to the testing fixture to statically maintain the position while CT images of the hand were obtained. These CT images were used to determine the global wrist joint angles, as well as the angles observed within the radiocarpal joint and the midcarpal joint.

Each specimen was tested in two different states: intact normal and the PRC wrist. The PRC procedure was performed by the excision of the scaphoid, lunate and triquetrum with a dorsal longitudinal incision. Care was taken not to cause any damage to the lunate fossa on the radial articular surface and the articular head of the capitate. Each of the incisions to the joint capsule and the skin were re-approximated and repaired using a 2-0 braided suture. Once the PRC procedure was complete, each wrist specimen was tested in the motions previously described with the same methodology and tendon forces.

Blankenhorn and colleagues developed a unique software to analyze and measure the various angles of the wrist joint from CT scans. [33], [74] 3D computer bodies were generated from the CT scans representing the capitate, lunate and radius for the intact wrists and the capitate and radius for the PRC wrists. The kinematics positions of the wrist specimens were determined from bone orientation changes between the neutral scans and scans with the four motions of interest. In terms of the intact wrist, angular changes in the midcarpal joint, the radiocarpal joint and global wrist angles were calculated and reported. Following PRC, the global wrist motion (also referred to as the new radiocarpal joint) was calculated and reported.

In the second study conducted by Tang and colleagues, three pairs of cadaveric upper extremities were prepared in a similar manner as described above. Each specimen was radiographically inspected for obvious degeneration and prepared and loaded on the testing

fixture with the forearm secured in a neutral position (Figure 5.2-1). The specimens were secured by bolting the radius and ulna to the test fixture. The flexor and extensor tendons were sutured and attached to spring loading scales on the testing fixture. Each wrist specimen was tested in three positions: 45^{o} of flexion, neutral and 45^{o} of extension. Each wrist position was achieved by manually varying the force applied to the tendons, with a combined total load equaling 200N. In the intact state, the tendon loads were varied until the desired wrist angles were achieved. The wrist angle was verified using a goniometer to measure the angle between the radius and third metacarpal. Once desired wrist position was achieved, each specimen was manually secured to prevent change in joint angle during testing. The manner in which the specimens were secured in the desired position for each test was not discussed in the publication. Each specimen was tested in two different states: intact normal and PRC wrist. The PRC procedure was performed as described in the previous experimental study.

After excision of the carpal bones for the PRC procedure, a radial styloidectomy was performed with care to preserve the articular surfaces and the radioscaphocapitate ligament. A radiostyloidectomy was performed to eliminate carpal bone abutment against the radial styloid process during contact force test. In this case a much higher combined load was applied as compared to the range of motion study, and so the bones compacted together to a greater extent. Thus, a styloidectomy was required to reduce undesired bone contact. Once the surgical alterations were completed, each tendon was loaded with the same amount of force as used in the intact state. Again, the specimen was manually supported to maintain the desired joint angle and position while the pressure test was conducted.

For this study, Tang and colleagues investigated the changes in contact pressure between the bones pre- and post PRC surgery. The contact pressure was measured using Fuji pressure

contact film (Fuji Photo Film Co., Ltd., Tokyo, Japan). Two types of contact films were used: UltraSuperLow film (range 0.2-0.6 MPA) for the intact wrist and Low film (range 2.5-10 MPA) for the PRC wrist. Each film was calibrated and sealed to protect it from moisture during the experiments. The films were placed within the radiocarpal joint through a dorsal longitudinal incision of the wrist. Once the radiocarpal joint was exposed in the intact wrist, a template of the distal forearm (including the radial articulating surface, TFCC and ulnar head) was created. These templates were used to create custom shaped Fuji films for each specimen.

Each wrist specimen's tendons were first loaded with the combined 200N force to achieve the desired testing position. The exact loads applied to each individual tendon were not disclosed within the publication. Once the desired position was achieved for the intact wrist, the carpus was manually distracted to allow placement of the custom shaped UltraSuperLow film within the radiocarpal joint. The tendon loads were then reapplied for 60 sec, while manually securing the specimen to ensure that wrist position did not change. The load was then removed and the carpus distracted to allow for careful removal of the film. To ensure accuracy, this testing was repeated in each position until three consistent sets of film were obtained. Care was taken throughout testing to minimize the creation of artifacts on the Fuji film. Once the wrist specimen was tested in all three positions with consistent results, a PRC and radial styloidectomy was performed. The testing sequence was then repeated with the same tendon loads at identical wrist angles. Again, the wrist specimens were manually supported to ensure no motion occurred during testing. Each Fuji film was analyzed using a custom software developed in MATLAB (The MathWorks, Inc., Natick, MA). This determined and measured the pressure, contact area and location of the carpal bones during each test.

5.3 COMPUTATIONAL MODELING OF PROXIMAL ROW CARPECTOMY BIOMECHANICAL STUDIES

As with the range of motion study by Pervaiz et al, the two cadaveric PRC experiments were replicated with the 3D rigid body wrist model. Testing was recreated within the SolidWorks space with the model in both the intact state and after a simulated PRC procedure. All the active muscle forces and soft tissue constraints were replicated from each study within the model. The simulations provided wrist biomechanical results which were validated against the findings reported in the two experimental studies.

In the experimental study by Blankenhorn et al, the cadaveric wrist specimens were secured to a testing fixture with the arm in a horizontal orientation with the palmar aspect facing the ground. This orientation of the wrist was recreated within the SolidWorks design space by fixing the radius and ulna in a neutral position and defining the direction of the gravitational force in the palmar direction along the dorsopalmar axis (Figure 5.3-1). Gravitational force was replicated with the use of the native SolidWorks Motion tool as described in Chapter 4. As was done with the RSL fusion range of motion study, all the remaining carpal and metacarpal bones were permitted to move freely. These bones were only constrained by the defined soft tissue structures and the bony articulations. Once again, the first and third metacarpal bones were exceptions to this. The first metacarpal bone was fused to the trapezium bone since it did not play any role for wrist motion in this study. The third metacarpal was fixed relative to the capitate since the two bones have been defined to move as one unit.

Figure 5.3-1: Wrist model orientation and gravity direction (green arrow) for PRC experimental studies

The muscle tendon forces were replicated in a similar manner as previously described. Each tendon was represented with two constant force vectors applied at the respective insertion points (Figures 3.9-2 and 3.9-3). The magnitudes of the forces applied at each insertion point for the four wrist motion angles are shown in Table 5.3-1. All four sets of tendons were loaded to varying degrees to achieve each of the wrist positions.

Muscle Name	Flexion	Extension	Radial Deviation	Ulnar Deviation
Flexor Carpi Ulnaris	24 N	12 N	20 N	4 N
Flexor Carpi Radialis	24 N	12 N	40 N	5 N
Extensor Carpi Radialis Longus	12 N	30 N	50 N	5 N
Extensor Carpi Ulnaris	12 N	30 N	12 N	25N

Table 5.3-1: Muscle load applied to achieve each wrist position

Once all four motions were tested in the intact normal wrist model, a simulated PRC procedure was conducted to accurately replicate the surgically altered experimental specimens. First, the scaphoid, lunate and triquetrum bone structures were removed from the design space. All the remaining bones of the carpus were temporarily locked together to create one unit. The entire carpus was then moved proximally towards the distal radial articulating head and positioned such that the proximal capitate head sat upon the lunate fossa of the radial articulating surface (Figure 5.3-2). The positioning of the carpus was further examined to ensure that the carpal bones were oriented between the capsular structures and that no structural overlap existed. Once a satisfactory placement of the distal wrist was achieved, all the bones were then unlocked from each other. This allowed the bones to move freely in response to any perturbation, restrained only by the articulating surfaces and the soft tissue structures.

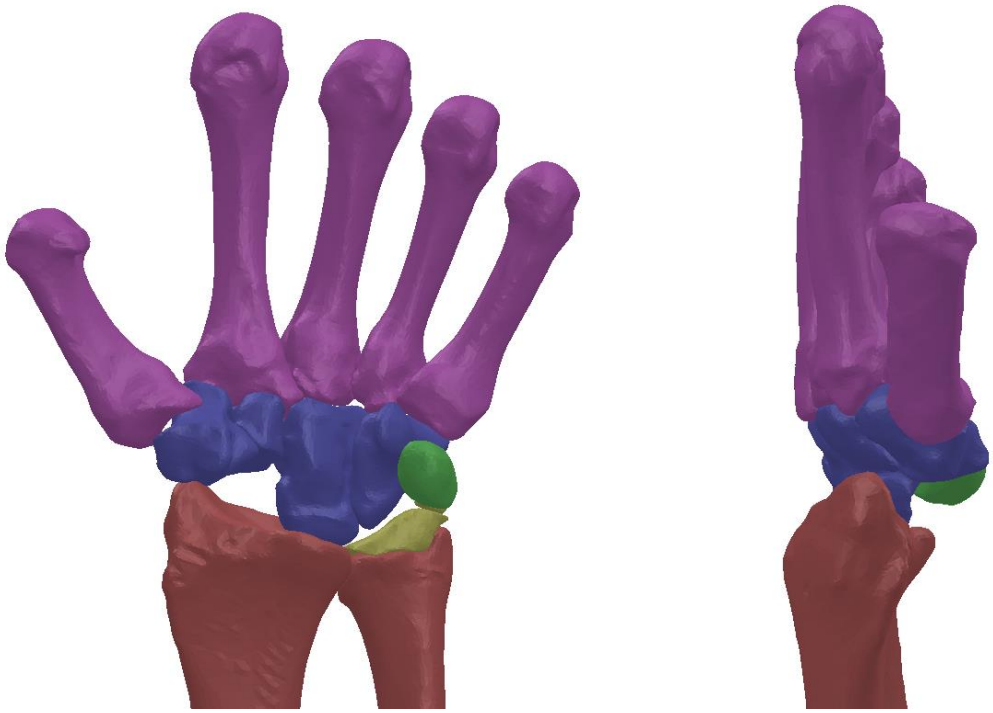

Figure 5.3-2: Wrist model after applying simulated PRC procedure (Capsular structures hidden for clarity).

All the remaining settings and definitions for the model were maintained as previously defined. With the removal of the proximal carpal row, a number of the ligaments were suppressed since attachment points existed on the excised bones. These ligaments were the SL, RS, UL, SRL, LRL, DRC, SC, RT, TC, LT, UT, STT, DIC, TH, PT and the proximal part of the TCL. During a clinical PRC surgical procedure, these ligaments are not normally extracted from the joint. However, they are essentially suppressed since they are no longer physically attached to a bone. Except for the interosseous ligaments, most of the ligaments are also connected to the surrounding soft tissue forming parts of the capsular structures. Thus, even with the loss of many of its native ligaments, some stabilization comes from the surrounding soft tissue that encapsulates the entire wrist complex.

With the newly attained PRC wrist state, the model was then tested in the four wrist motions with the tendon loads used during the intact sate. Flexion, extension, radial and ulnar deviation angles achieved during each motion was measured.

The experimental set-up for the contact pressure study conducted by Tang et al employed a similar testing apparatus and methodology. Thus, the study was replicated within SolidWorks in a very similar manner as the carpal kinematics PRC study. The 3D wrist model's positioning, orientation, and structures were all modeled in an identical manner as described for the previous two studies. However, during the final contact force test simulation, the capsular retinacular structures and the distal TFCC were removed from the SolidWorks design space. The proximal TFCC was included in the model as previously described.

The capsular structures and the distal TFCC replicated the soft tissue wrapping effect on the carpus during joint motion. Based on the testing methodology of this experiment, their incorporation was not essential for this study. In fact, the incorporation of these structures would most likely diminish the final contact force experienced between the bones and lead to inaccurate results. The capsular structures and the TFCC were represented as solid bodies to enable them to impart contact forces to the carpal bones. This was done to replicate the wrapping effect these structures anatomically are assumed to perform. This stabilizing effect is most critical when the joint is going through its kinematic motions. However, during the experimental study, the specimens were manually maintained at the desired wrist angle. Thus, these tissues were not able to play the stabilizing role they normally would have performed. Moreover, since the structures were modeled as solid bodies, forces experienced by the carpal bones would also be transmitted through these structures instead of just the bones. Thus, inclusion of the soft tissue

structures would lead to an inaccurate prediction of the path of force transmission. The manner in which these structures were removed is discussed in further detail below.

In the contact pressure experimental study, each wrist specimen was tested in three different positions (45^o flexion, neutral, and 45^o extension) and in two different states (intact and PRC). For each test, the wrist was manually loaded via the tendons to the desired positions with a combined 200 N load while ensuring the carpus maintained the desired wrist angle. To replicate this testing sequence, additional restrictions on the computational model had to be employed to maintain the desired wrist angle during each test.

To replicate the desired restrictions as the experimental study, reference planes were defined within the SolidWorks design space. During testing in the neutral position, two additional planes were created to ensure proper orientation of the wrist model. The 3D wrist model has been designed in an initial resting neutral state. To maintain this neutral state a medial-lateral plane and an anteriorposterior plane were created and aligned such that the long axis of the third metacarpal perfectly lined up at the intersection of these two planes. The third metacarpal long axis was then defined to remain coincident at the intersecting line of these two planes. This prevented the third metacarpal, and hence the overall wrist, from going into any flexion/extension or radial/ulnar deviation (Figure 5.3-3). Yet, this set up allowed the carpus to move along the proximal/distal axis. Once the desired wrist position was achieved and the third metacarpal was secured within the reference planes, the capsular structures and the distal TFCC were removed prior to running the contact force test. During the simulated test on the wrist model, a neutral state was maintained while still allowing carpal bones to interact in a proximal/distal manner in response to the tendon loads. This procedure was replicated in an identical manner to test the PRC wrist in the neutral position.

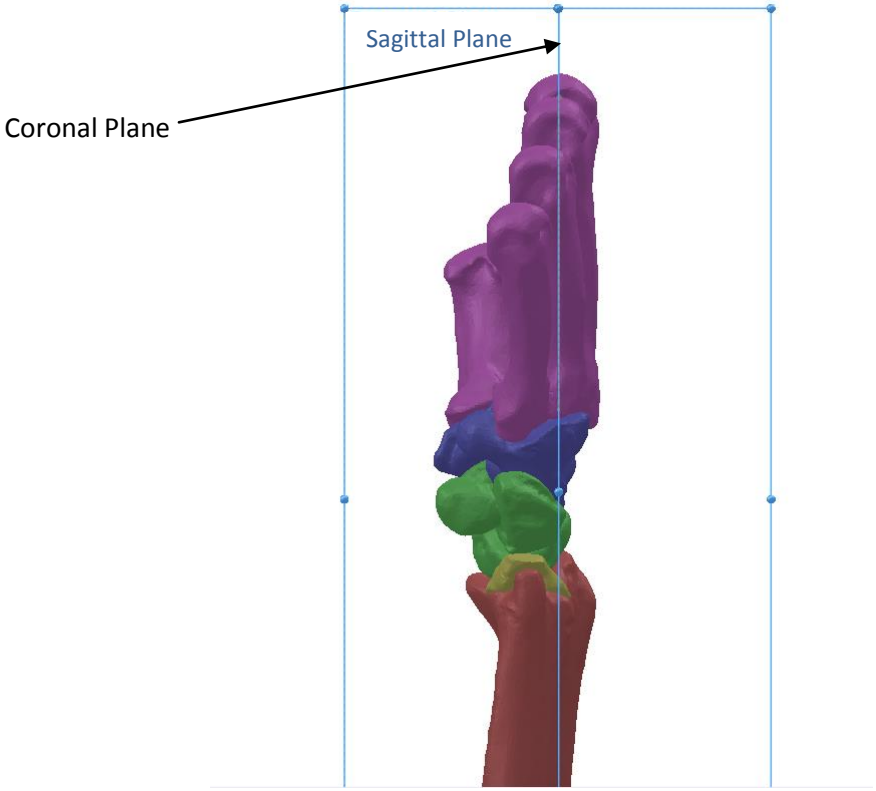

Figure 5.3-3: Securing intact wrist third metacarpal long axis to two planes for neutral position contact force test

In replicating the tests conducted in flexion and extension, a slightly different approach was utilized. First, the complete intact model was loaded with the forces outlined for the kinematic PRC study (Table 5.3-1). From the kinematic responses observed from the perturbations, the wrist position at 45^{o} of flexion angle was identified. By referencing this position, a new plane was defined along the medial-lateral aspect of the wrist. This plane was positioned such that the long axis of the third metacarpal was perfectly aligned within it in the 45^{o} flexed orientation. The normal vector of this plane was defined to remain parallel to the sagittal plane in the model design space. A similarly defined a medial-lateral plane was also created, positioned to line up with the third metacarpal in the 45^{o} wrist extension orientation.

With these newly defined planes, the bones of the hand and wrist were reoriented such that these angular states would be the starting position for the contact pressure test simulation.

The 3D wrist model was formulated such that each simulation always began with the joint in the neutral resting position. To achieve the desired flexed/extended starting point, the modeled bones had to be manually repositioned to align up with the defined reference planes. Since the intact wrist is a compound joint made up of multiple joints, this repositioning had to be achieved in multiple steps. Since the desired kinematic position had already been identified, the capsular structures and the distal TFCC were removed from the model. This was acceptable since the kinematic stabilizing role they performed was no longer required. Next, the entire wrist was locked together into one unit and was rotated along the dorsal palmar plane around the centroid of the lunate bone (Figure 5.3-4). The amount of angular motion required was estimated by visually inspecting the position of the long axis of the third metacarpal and the reference plane. The proximal carpal row (scaphoid, lunate, triquetrum and pisiform) was then unlocked from the locked unit. This created a single unit formed by the remaining bones of the hand. This unit was then angularly rotated in the dorsal palmar plane around the centroid of the capitate to achieve the overall desired wrist angle (Figure 5.3-5). The desired positioning required was again determined from visual inspection from a medial/lateral aspect. A small amount of translation was also required for the entire carpus in the dorsal palmar direction to achieve the closest possible alignment with the defined plane. To achieve the flexed intact wrist position, the carpus was rotated 27^{o} around the centroid of the lunate and 17^{o} around the centroid of the capitate. Yet, perfect alignment between the long axis of the third metacarpal and the defined plane was very hard to achieve. This was likely from the fact that wrist motion also

incorporates motions in the carpo-metacarpal joint and translational motions of the individual bones themselves.

Once the manually re-oriented wrist joint was positioned within 1^{o} of the desired angle, the wrist orientation was determined to be sufficient for the purposes of this test. The defined 45^{o} reference plane was then redefined to align up with the long axis of the third metacarpal in the flexed wrist joint. Once this was complete, all the bones were unlocked and were free to move based on the restrictions defined within the model.

The repositioned extended wrist joint was also achieved in a similar manner. With the defined reference plane, the carpus was rotated around the centroid of the lunate and capitate to achieve the desired alignment. The carpus was rotated 31^{o} around the lunate and 15^{o} around the capitate. Once the wrist angle was positioned with 1^{o} of the desired 45^{o} extended state, the reference plane was redefined to perfectly line up with the third metacarpal.

For both the flexion and extension test, the long axis of the third metacarpal was defined to remain coincident within the newly defined reference plane. This prevented the wrist from going into any further flexion/extension during the contact force testing. However, the wrist was still free to move within the anterior-posterior plane or along the proximal/distal axis (Figure 5.3-6 and Figure 5.3-7).

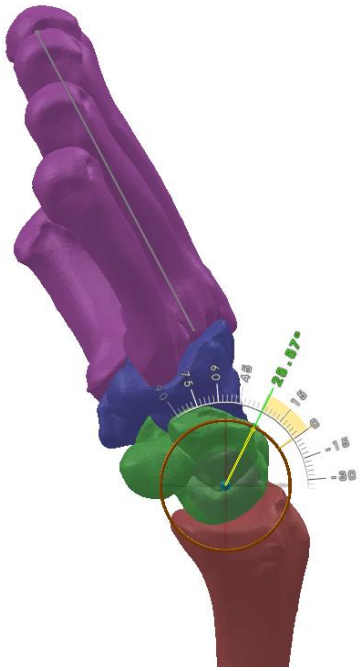

Figure 5.3-4: Reorienting the carpus around the radiocarpal joint to achieve desired flexion angle position

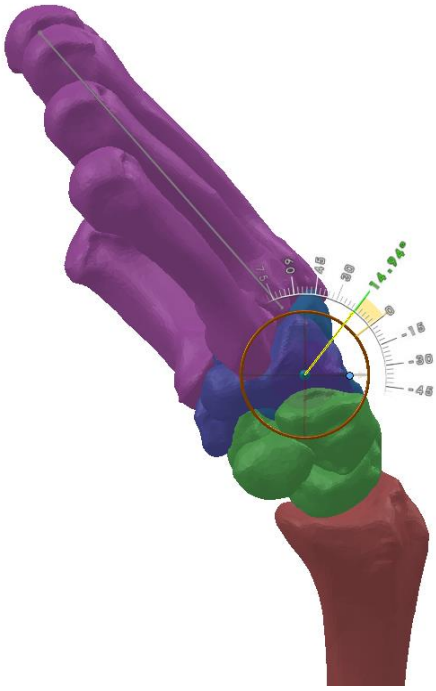

Figure 5.3-5: Reorienting the carpus around the midcarpal joint to achieve the desired flexion angle position

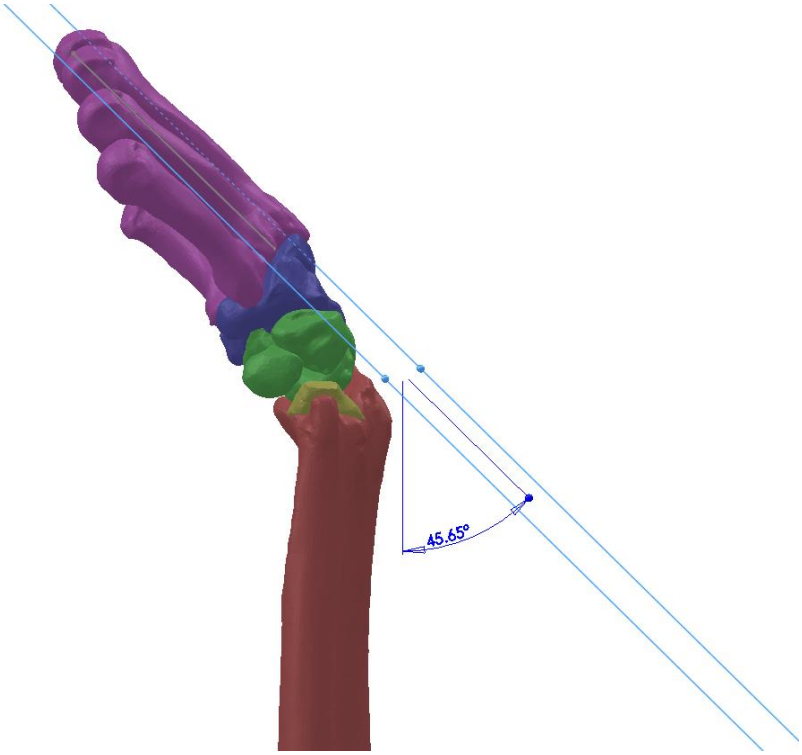

Figure 5.3-6: Securing third metacarpal long axis for flexion position contact force test for intact wrist

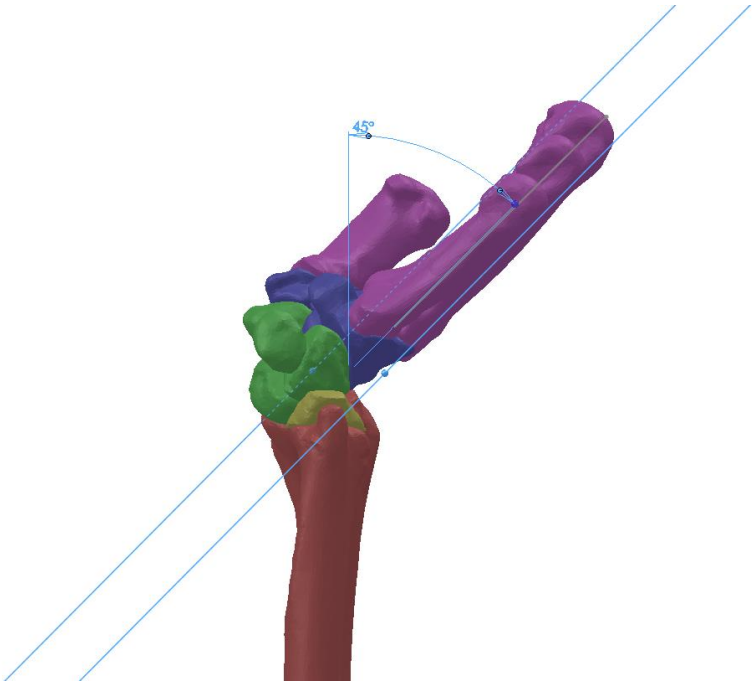

Figure 5.3-7: Securing third metacarpal long axis for extension position contact force test for the intact wrist

With the newly oriented wrist starting positions with the external restrictions imposed, the wrist tendons were then loaded to replicate the test conducted within the study. The tendon loads applied for each position was a combined total of 200 N. The individual amounts of loads applied to each tendon for flexion and extension was based on the ratio at which the loads were applied to the PRC range of motion test (Table 5.3-2). For the neutral state, slightly higher loads were applied to the extensor muscle tendons due to the orientation of the hand and its tendency to go into flexion due to gravity (Table 5.3-2).

Since the starting wrist position for some of the tests was not in the normal neutral resting state, the model needed a chance to stabilize prior to the application of the external perturbation. Thus, during each simulation, the tendon loads were defined to be activated one second after the start of the study. This was important in the cases of the flexion and extension tests. Since the 3D wrist model was designed in a neutral position, all the ligaments and soft tissue structures are defined by lengths and properties while in the neutral state. During a simulation, if the starting state of the wrist is of a non-neutral nature, many of the soft tissue structures are no longer in their defined resting state. Thus, the entire model underwent motion and changes to achieve a new equilibrium at the new wrist position. Imposition of external forces while this equilibrium was being achieved can lead to unpredictable results. Thus, a slight delay was provided before the tendon forces were activated.

Muscle Name	Flexion	Neutral	Extension
Flexor Carpi Ulnaris	28.58 N	45 N	66.66 N
Flexor Carpi Radialis	28.58 N	45 N	66.66 N
Extensor Carpi Radialis Longus	71.42 N	55 N	33.34 N
Extensor Carpi Ulnaris	71.42 N	55 N	33.34 N

Table 5.3-2: Muscle load applied at each position during contact pressure test

Once all three position tests were conducted on the intact wrist, a simulated PRC procedure was carried out in a similar manner as previously described. Additionally, a radial styloidectomy was also performed to reduce impingement of the trapezium with the radial styloid process (Figure 5.3-8). An "extrude cut" feature native within SolidWorks was used to simulate the styloidectomy. Care was taken to ensure the attachment point for the radiocapitate ligament was preserved with the removal of the distal lateral tip of the radius.

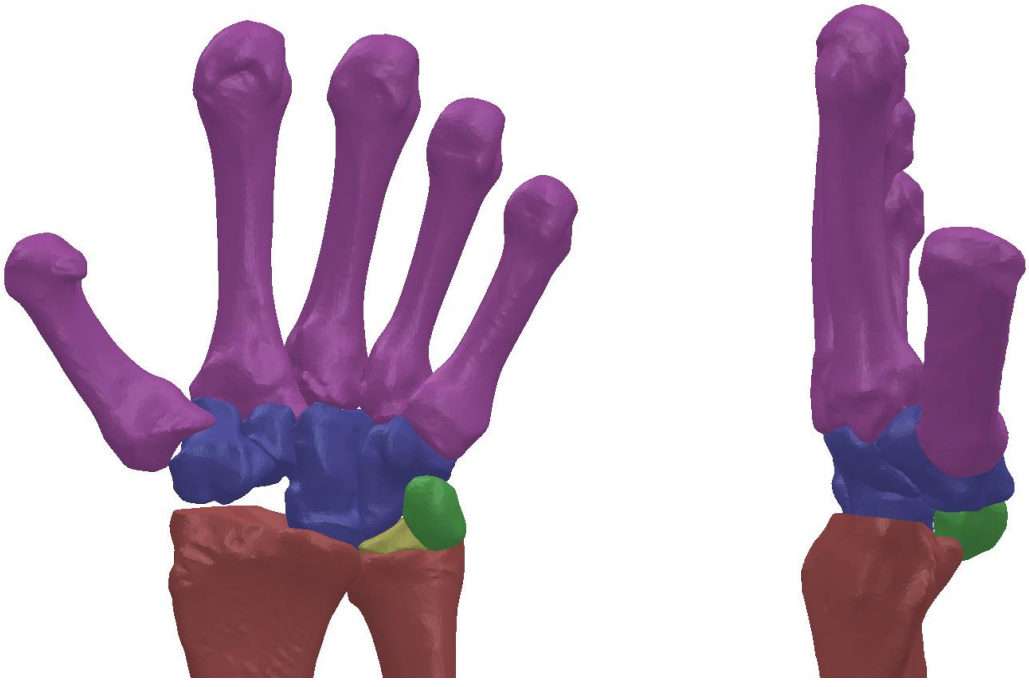

Figure 5.3-8: PRC Wrist with radial styloidectomy

In the PRC state, a similar reorienting method was used to achieve and secure the carpus in the neutral, 45^{o} of flexion and extension positions. For the neutral state, the PRC wrist was secured between the intersecting line of the coronal and sagittal planes (Figure 5.3-9). To obtain the 45^{o} wrist flexion plane, the PRC wrist model tendons were loaded with the forces used for the PRC kinematic study (Table 5.3-1). The reference plane was obtained in a similar manner as the intact wrist. The carpus was rotated around the centroid of the capitate (Figure 5.3-10) to achieve the alignment with the defined reference plane (Figure 5.3-11). For the extension position, the PRC wrist did not achieve a minimum of 45^{o} extension with the applied loads. The PRC wrist model tendons were loaded with similar flexor forces as the kinematic study (Table 5.3-1) but with slight higher extensor muscle forces (35 N for ECRL and ECU). This ensured that the minimum 45^{o} extension position was achieved. The reference plane was then defined and the carpus reoriented to achieve the desired extended starting position for the PRC wrist (Figure 5.3-12). The capsular structures and distal TFCC were removed from the design space. Similar assumptions and corrections were made as described for the reorientation of the intact wrist. Once the newly oriented positions for the PRC wrist were achieved, the sequence of testing was then repeated to obtain contact force results with the defined tendon loads (Table 5.3-2) in the different wrist positions.

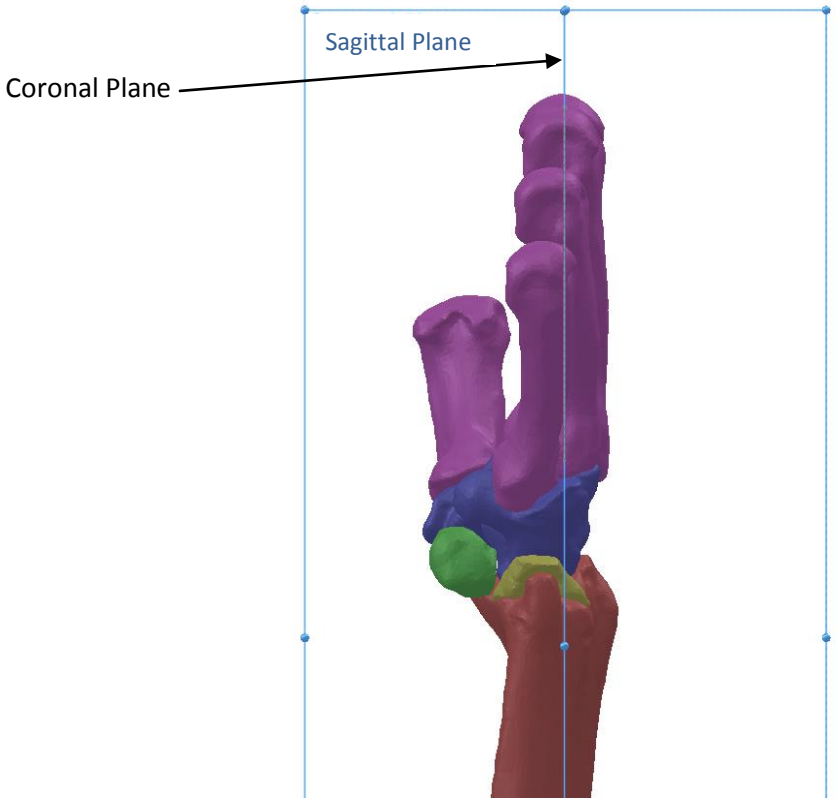

Figure 5.3-9: Securing PRC wrist third metacarpal long axis to two planes for neutral position contact force test

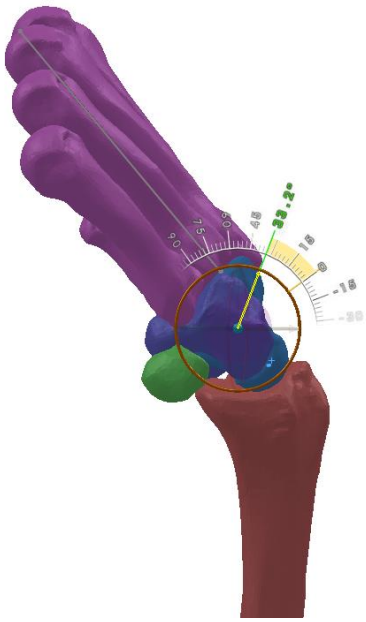

Figure 5.3-10: Reorienting the PRC carpus around the capitate centroid to achieve desired flexion angle position

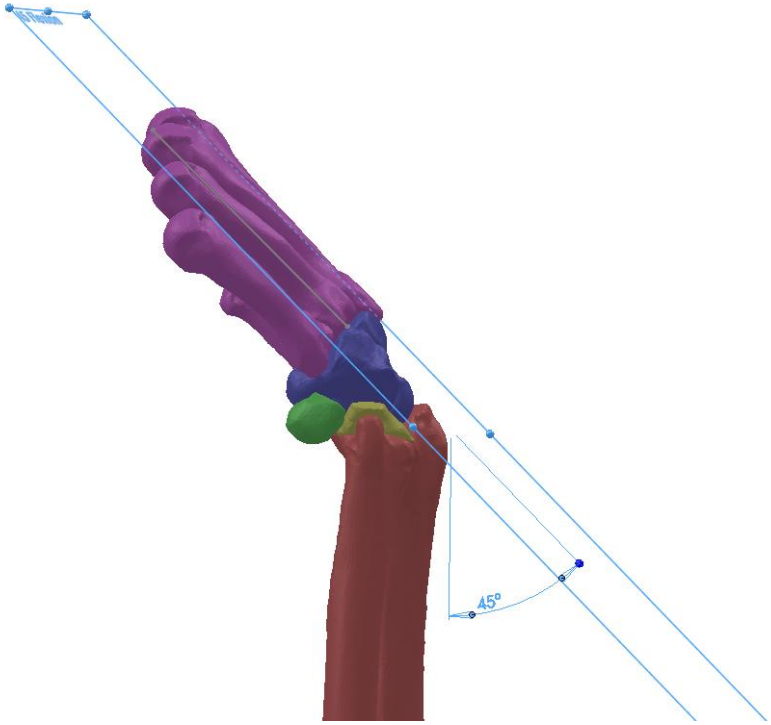

Figure 5.3-11: Securing third metacarpal long axis for flexion position contact force test for PRC wrist

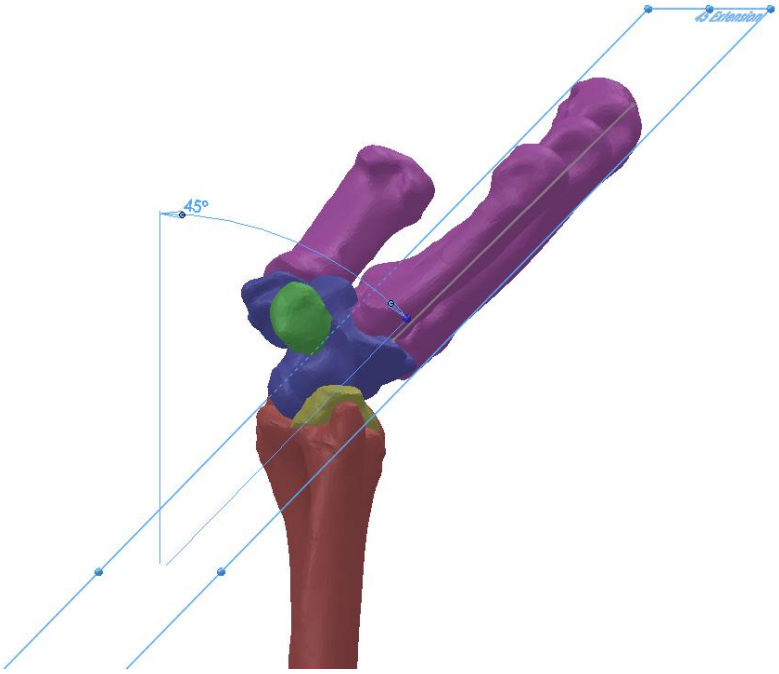

Figure 5.3-12: Securing third metacarpal long axis for extension position contact force test for PRC wrist

5.4 RESULTS

In the experimental PRC kinematics study conducted by Blankenhorn et al, the angles of motion achieved in each state were determined by comparing CT images of the wrist bones in neutral and at the final position at the end of the test. The tendon forces applied were varied to ensure there was minimal out of plane motion for the wrist. Thus, to measure the planar angles achieved by the 3D wrist model, a similar approach was utilized as described in Chapter 4. Projections of the coronal and sagittal planes were created to allow 2D measurements of flexion/extension angles and radial/ulnar deviation angles respectively. The global wrist motion was determined by measuring the projected angles formed between the long axis of the radius and the third metacarpal on the respective planes. The experimental study measured the angles formed between the long axis of the radius and the capitate. However, in the model, since the third metacarpal and the capitate were designed to act as one structure, it could be said that both bones shared the same long axis.

The range of motion results obtained from the simulated study with the 3D wrist model were validated against the outcomes reported by the cadaveric study (Figure 5.4-1 – Figure 5.4-3). Overall, the results demonstrate that the wrist range of motion was significantly reduced following a PRC procedure. The 3D wrist model determined that the wrist flexion-extension arc decreased from 117^{o} to 90^{o} after a PRC procedure. Likewise the radio-ulnar motion arc decreased from 57^{o} to 40^{o}. These results correspond to a 23% predicted decrease in the flexion-extension motion arc as compared to a 32% decrease as experimentally observed in the cadaveric study. In the radial-ulnar deviation motion arc, a 29% decrease was predicted by the model as compared to a 27% decrease determined experimentally.

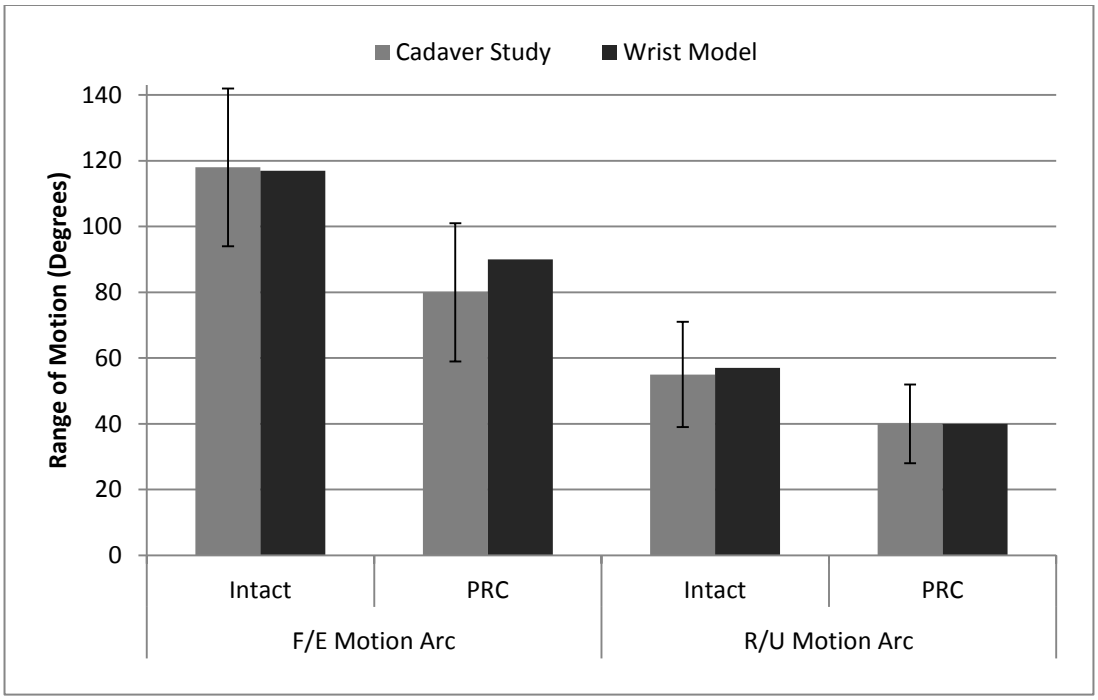

Figure 5.4-1: Total wrist motion arc in intact and PRC wrist

Similar trends in the results can be seen between the values predicted by the 3D wrist model and the experimental cadaveric study for each of the motions individually (Figure 5.4-2 and Figure 5.4-3). In the intact normal state, the model predicted 72^{o} of flexion, 45^{o} of extension, 25^{o} of radial deviation and 32^{o} of ulnar deviation. Once a simulated PRC procedure was conducted on the wrist model and kinematics was retested, the model predicted 49^{o} of flexion, 41^{o} of extension, 15^{o} of radial deviation, and 25^{o} of ulnar deviation.

When comparing the angles in each individual wrist motion in the modelled and experimental results, specific differences can be observed. In terms of flexion, the model results accurately reproduced the experimental result trends and percent difference. The model predicted a 32% decrease in flexion after PRC while the experimental results showed a 29% decrease. In extension, even though a decreasing trend in wrist angle is observed, the model

underpredicts the overall percent change. The model predicts a 9% decrease in extension angle while the experimental study shows an overall decrease of 36%. In terms of radial deviation, a similar trend is also maintained , with the model predicting a 40% decrease while the cadaveric results shows a reduction of 45%. Finally, in ulnar deviation, the model predicted the percent decrease to be at 22% while the study results show a decrease in 15%. While some over and underprediction is observed by the 3D wrist model, all differences fall within one standard deviation. Thus, these differences are not significant and the model is able to accurately replicate the expected kinematics results for such a procedure.

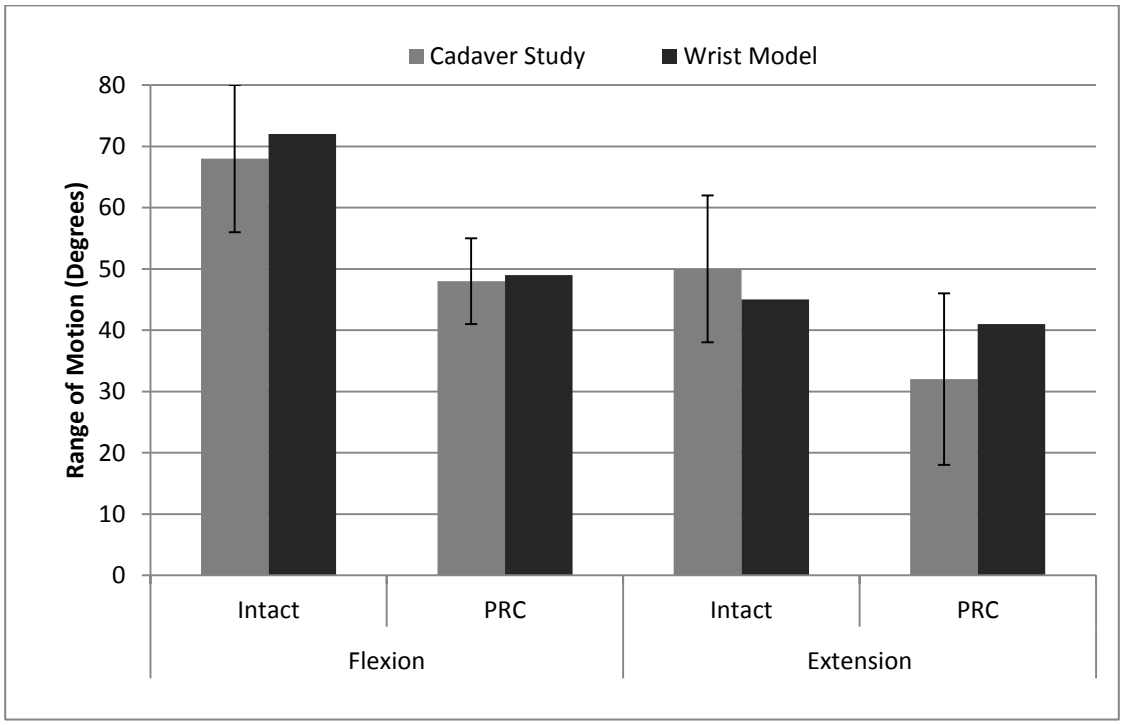

Figure 5.4-2: Flexion and Extension Range of Motion in Intact and PRC Wrist

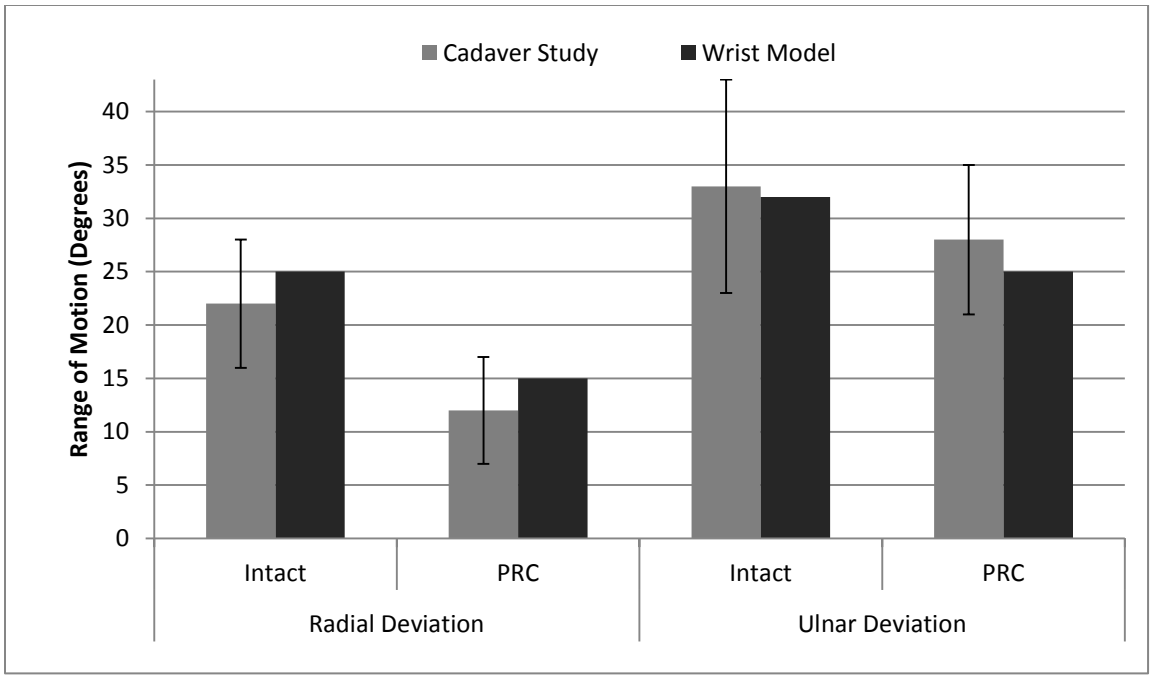

Figure 5.4-3: Radial and Ulnar Range of Motion in Intact and PRC Wrist

A qualitative inspection of the PRC wrist during the range of motion testing demonstrated that wrist angular motion was isolated between the capitate and the radio-carpal articulating surface (Figure 5.4-4 – 5.4-5). In addition to the angular motion, some translational motion of the capitate head was also observed. Some minor translational motion was observed in flexion, extension and radial deviation. However, in the case of ulnar deviation, a larger amount of translation was seen in the lateral direction of the wrist (Figure 5.4-5). This greater additional translation led the wrist to achieve the larger angular position in ulnar deviation as compared to radial deviation in the PRC state.

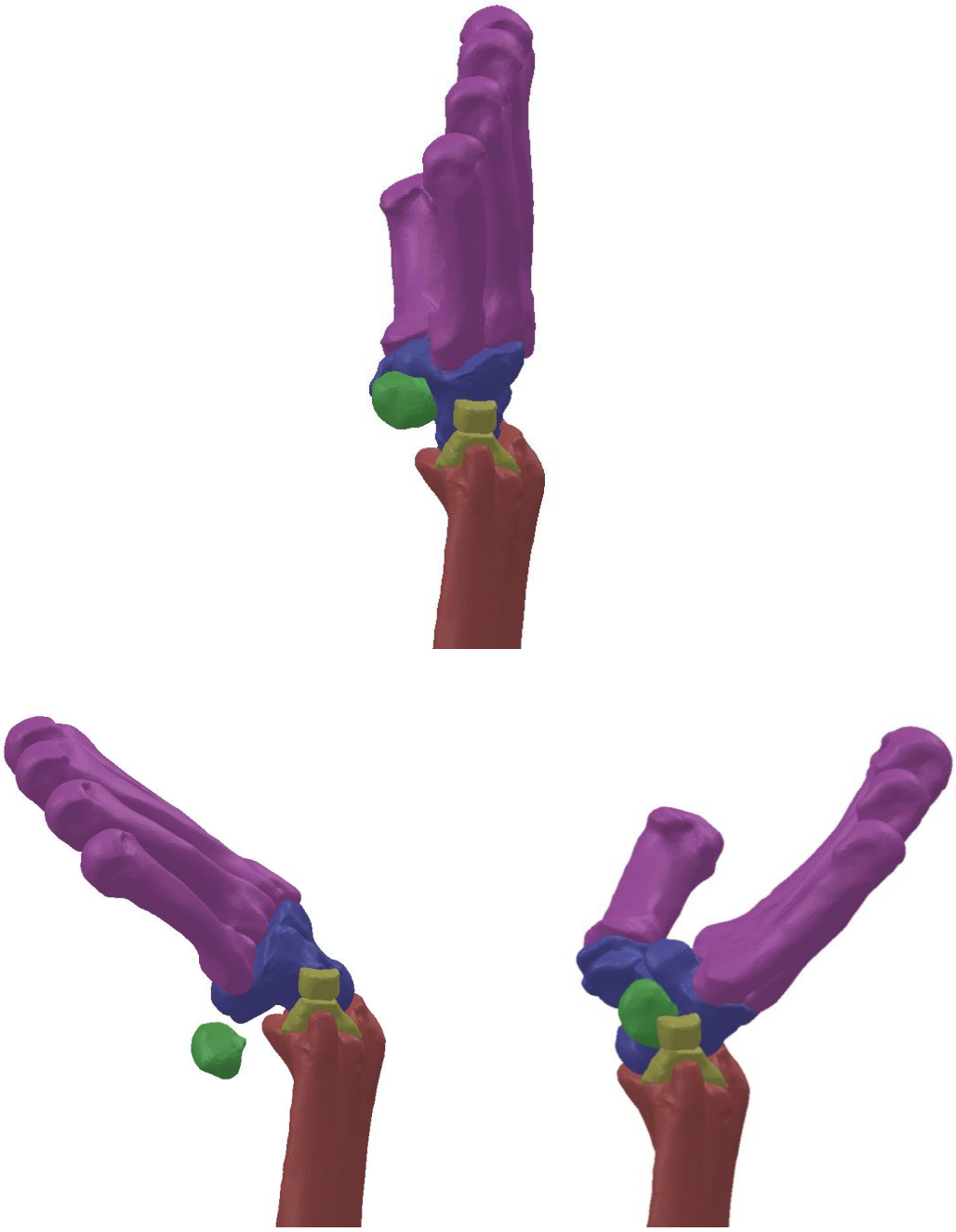

Figure 5.4-4: Motion of the PRC wrist in the flexion-extension arc. PRC Wrist in neutral (top), flexion (bottom left) and extension (bottom right) (Capsular structures hidden for clarity).

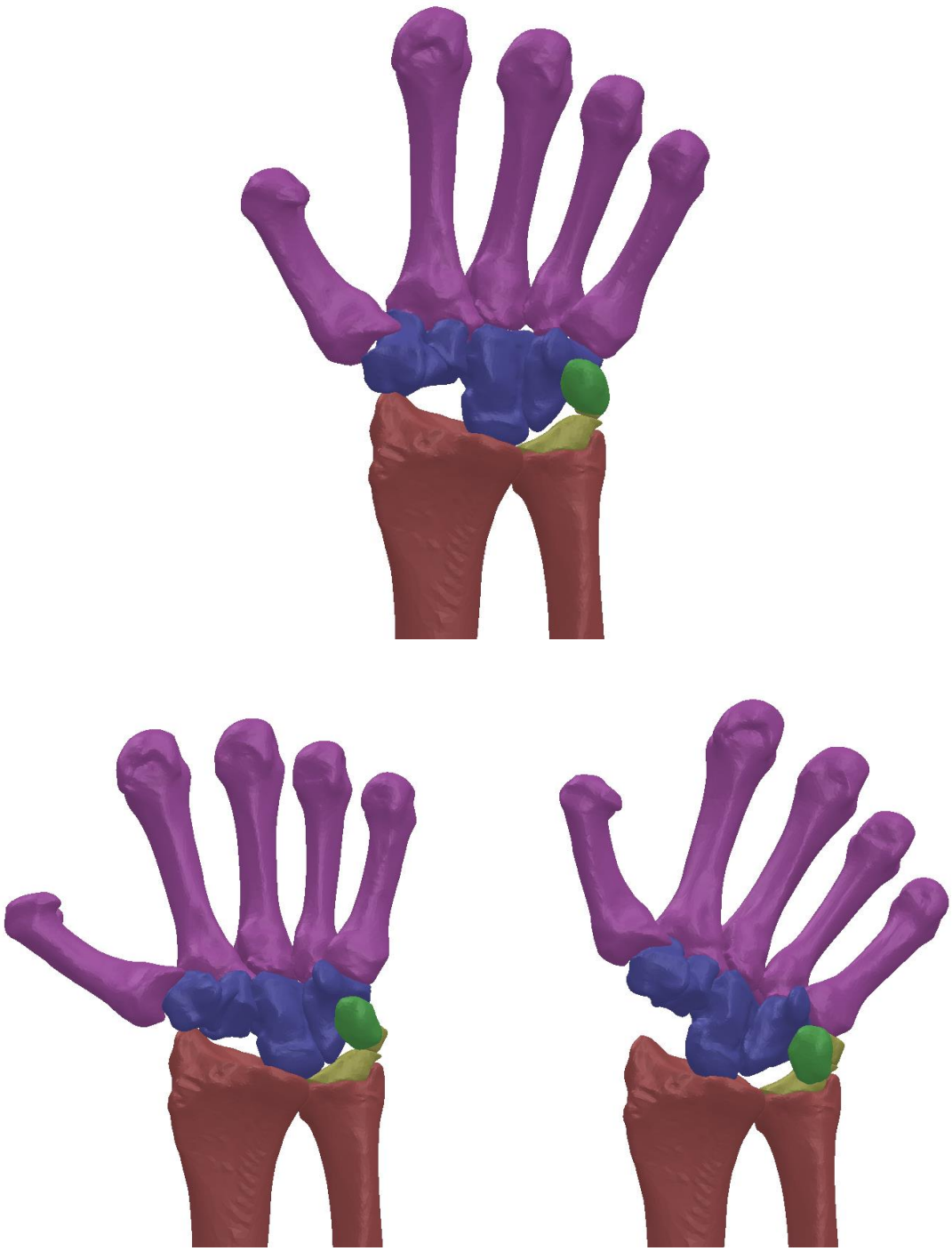

Figure 5.4-5: Motion of the PRC wrist in the radial-ulnar deviation arc. PRC Wrist in neutral (top), radial deviation (bottom left) and ulnar deviation (bottom right) (Capsular structures hidden for clarity).

In the experimental contact biomechanics study conducted by Tang et al, the investigators determined contact pressure within the radiocarpal joint with the use of Fuji pressure film. The study reported the changes in pressure and contact area between three motions and two different wrist states. Within SolidWorks, no native feature exists that allows for the calculation of pressure created between two interacting objects. However, SolidWorks is able to calculate the contact force generated between solid bodies. This tool was utilized to determine the contact forces generated between the various bones of interest and then compared to the contact force calculated from the reported pressures and corresponding contact areas.

The 3D wrist model was used to replicate this study and the findings were compared to the results from the cadaveric study (Figures 5.4-6 – 5.4-9). The results reported by the cadaveric study included peak pressure and contact area values between the distal forearm surface (distal radial surface, TFCC, and ulnar head) and the scaphoid and lunate for the intact wrist and the capitate for the PRC wrist. These values from the study were used to calculate the contact force experienced by the respective bones. It is not clear from the publication whether additional contact between remaining carpal bones and the distal forearm surface was ignored or if it was not reported. From the simulated studies, additional contact was found to occur in various orientations especially in the PRC wrist. It was found that in certain positions, contact occurred between the hamate and the TFCC as well as the trapezium and the distal radial surface. In addition to that, standard deviation values were not reported and could not be calculated from the data presented for the pressure results of the individual carpal bones.

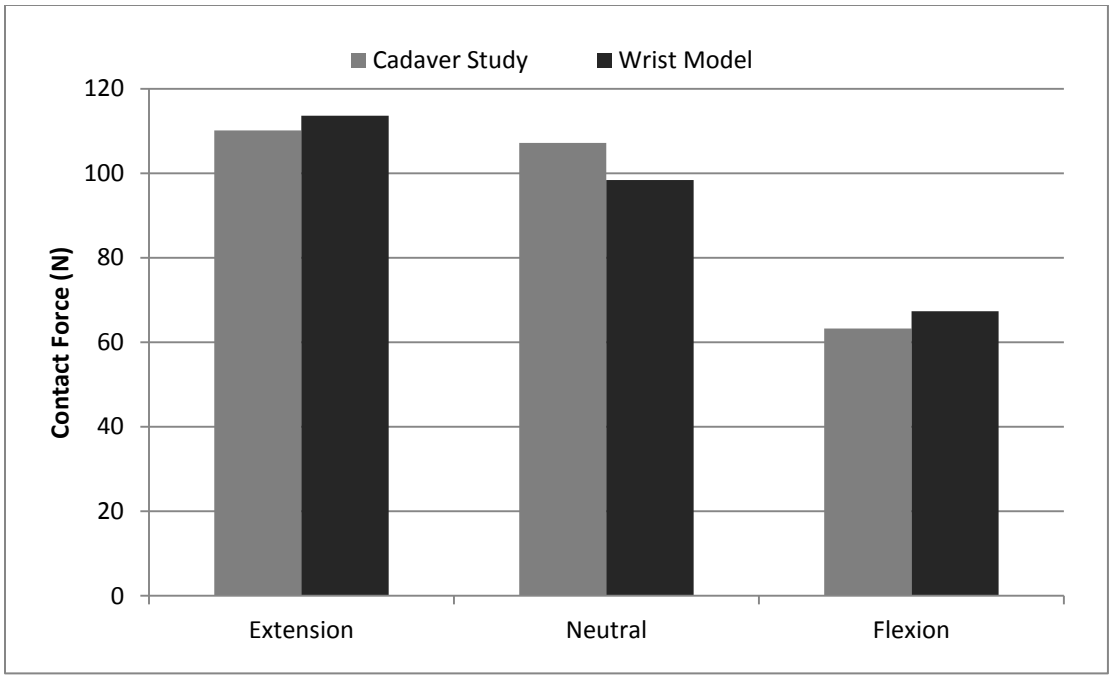

Figure 5.4-6: Scaphoid Contact Forces at the Radiocarpal Joint in the Intact Wrist

For the intact wrist, the contact forces predicted by the 3D wrist model for the scaphoid followed a relatively similar trend as the results from the experimental study (Figure 5.4-6). In all three positions, the results demonstrated good correlation. In flexion the experimental study reported a 63 N contact force, while the model predicted 67 N of force. In extension, experimental 110 N was observed while the model predicted 114 N of force generation. And in neutral, experimental 107 N of force was reported while the model predicted 98 N.

In the wrist, the lunate interacts with both the radial articulating surface as well as the TFCC/ulna during joint motion. Thus, at the radio carpal joint, contact forces are generated from two sources with the lunate. The experimental results reported for the lunate are a summation of the forces generated from both sources. The 3D wrist model's predicted results for the lunate bone were not as comparable as that predicted for the scaphoid bone (Figure 5.4-7). However, the overall decreasing trend in force generation when the wrist went from extension to flexion

was replicated. The largest difference was found in the force predicted in the extension position where the predicted value was nearly twice the experimental value (experimental = 102 N, model = 199N). In terms of the neutral (experimental = 76 N, model = 96N) and flexion (experimental = 69 N, model = 43 N) position forces, the obtained results were much more comparable.

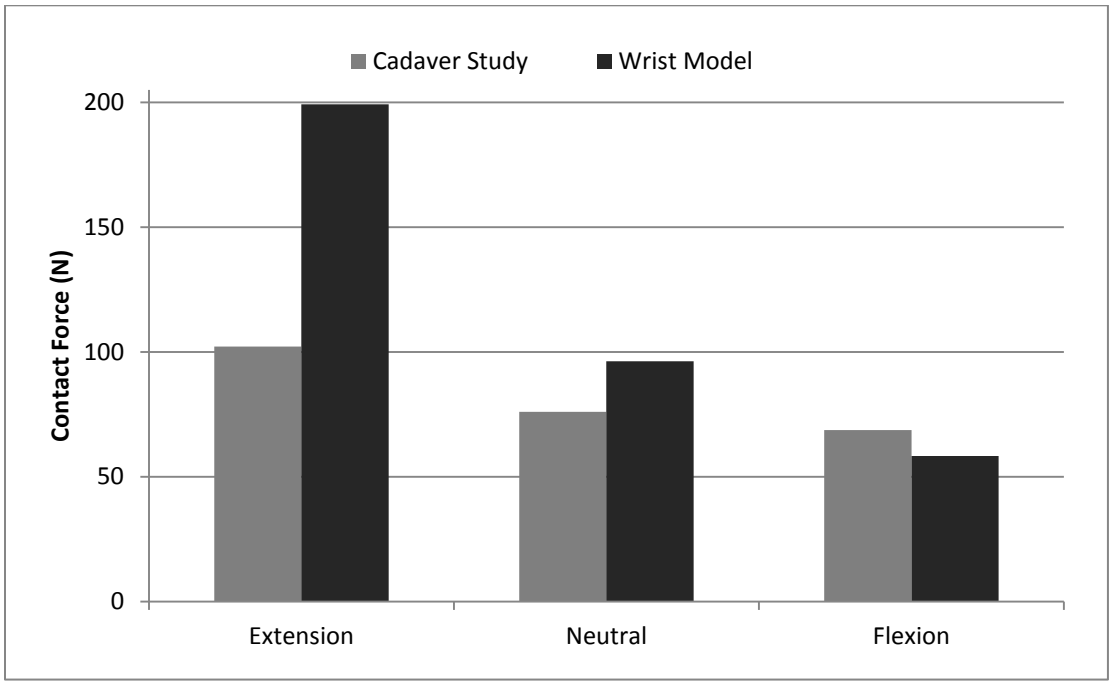

Figure 5.4-7: Lunate Contact Forces at the Radiocarpal Joint in the Intact Wrist

In the experimental study, once each specimen underwent testing in the PRC state, the results reported were the contact pressure generated between the capitate and the distal radial surface. In the wrist model it was observed that contact forces on the capitate were generated from both its articulation with the radius as well as the TFCC. The total predicted forces reported for the capitate are a summation of these two sources. When comparing the overall

predicted contact forces for the capitate bone (Figure 5.4-8), the general trend of the data reported was found to be opposite of that of the experimental results. In the experimental results, a slight increase in contact force was observed when the wrist goes from extension (155 N) to neutral (167 N) to flexion (174 N). However, the wrist model predicted a much more rapid decrease in contact force as the capitate moved from extension (197 N) to neutral (175 N) to flexion (114 N). Even though the overall trend in change may be slightly off, the results observed here does give an understanding of the range of forces the bones experience through its motions. In addition to that, due to the lack of some information in the reported experimental results, an extensive comparison between these values may not be appropriate.

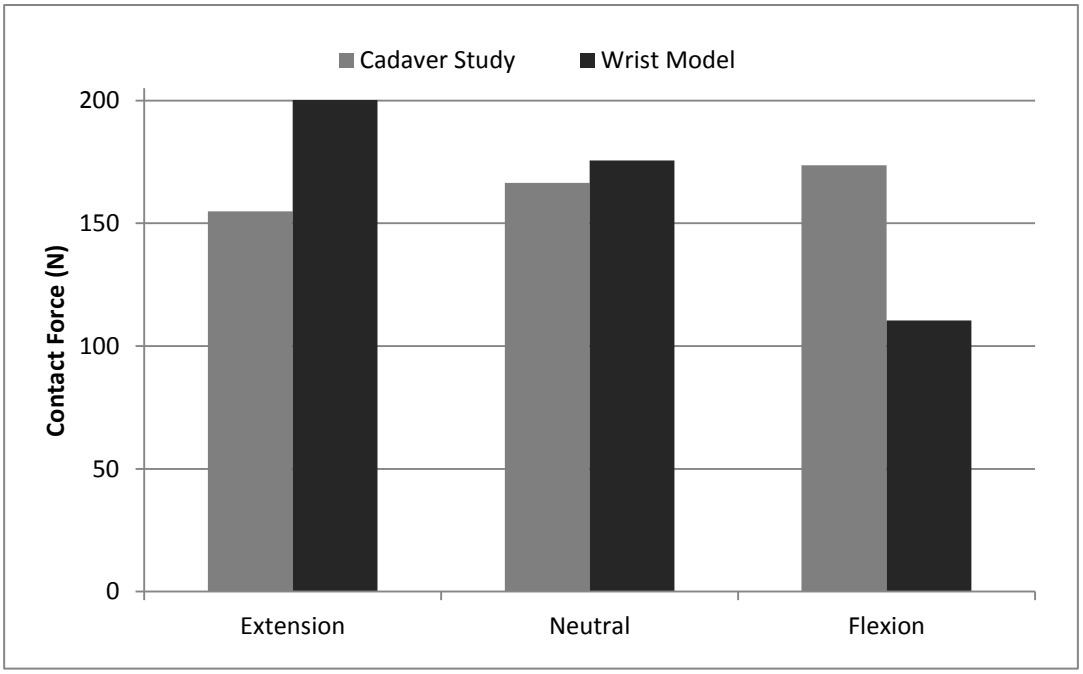

Figure 5.4-8: Capitate Contact Forces at the Radiocarpal Joint in the PRC Wrist

Since the 3D wrist model predicted additional contact forces in carpal bones other than just the scaphoid, lunate and capitate as reported by the experimental study, an additional

comparison of total force generated at the radiocarpal joint was conducted (Figure 5.4-9). In the intact state, the model predicted forces of 28N in extension, 27 N in neutral and 39 N in flexion. As previously mentioned, the study publication did not report any additional force generation in the intact wrist other than for the scaphoid and lunate. It is not clear whether no force was detected or whether these forces were eliminated from the results due to researcher selected focus. Similarly, in the PRC state, the 3D wrist model showed that along with the forces generated at the capitate, some force was also detected at the hamate, trapezium as well as the trapezoid. The forces generated at these bones were relatively low and ranged from 0 N to 31 N. These additional contact forces are incorporated in the total force comparison.

Standard deviations for the experimentally reported results were calculated from the data presented in the publication (Figure 5.4-9). The standard deviation of contact pressure (MPa) and contact area (mm^2) were graphically represented in the publication. These were measured and used to determine the high and low values for pressure and area. These pressure and contact area values were then multiplied to give an approximation of the standard deviation for the total contact force experienced across the joint.

Overall, the model was able to replicate the overall trend of the contact force experienced in the respective joints. However, a significant amount of over prediction was observed in multiple positions. The greatest differences found in the intact extension (experimental = 220 N, model = 341 N) and PRC extension (experimental = 155 N, model = 244 N) test specimens. While an overall over prediction is observed in these values, one main factor that may attribute to this difference may be the fact that the experimental results did not report the any additional contact forces in the other carpal bones. Additionally, the approximated standard deviations obtained from the experimental result show very high variance within the reported results. This

high variance could also account for the differences observed between the experimental and predicted results. It should be noted that most of the predicted values fell within the standard deviation of the observed results. The percent difference between the model's predicted results and the experimentally reported values range from 17% for the flexion position in PRC to 57% for the extension position in the PRC wrist (Table 5.4-1).

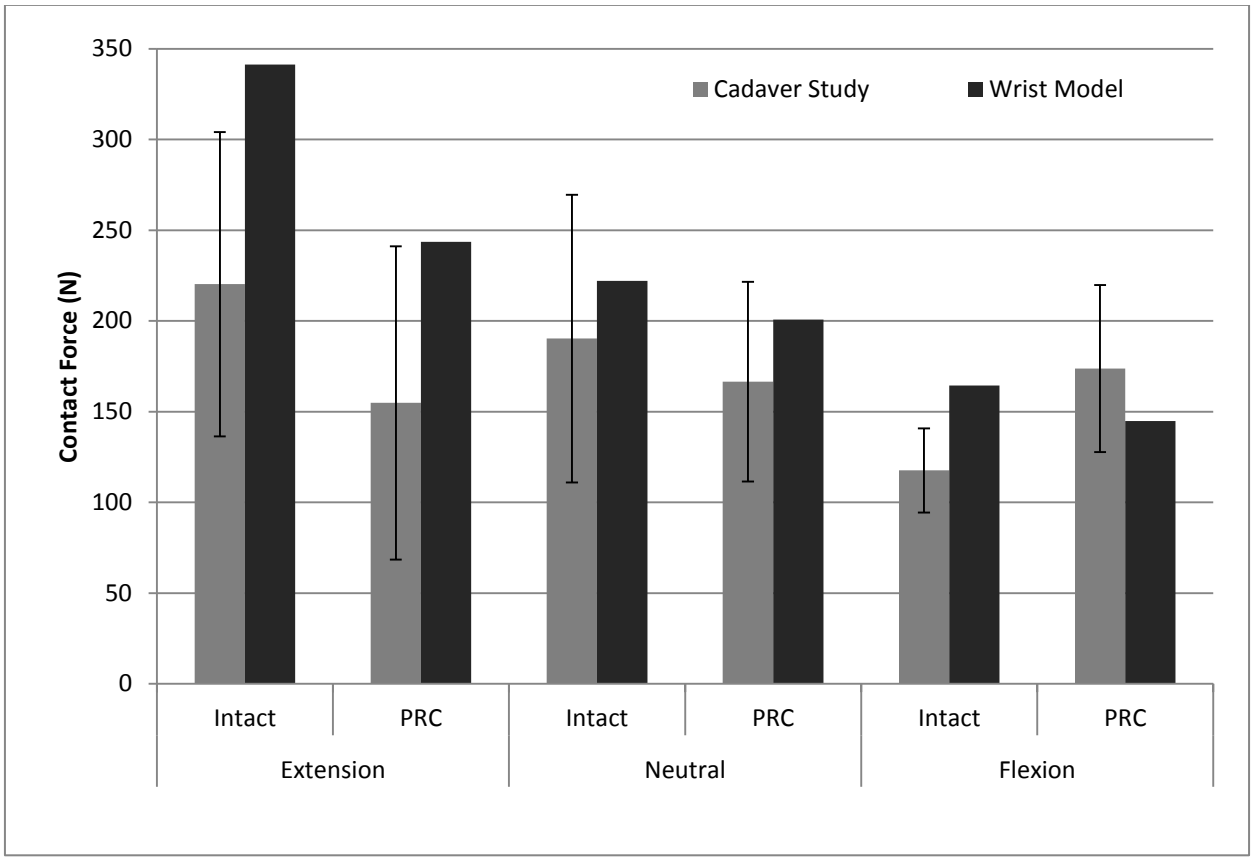

Figure 5.4-9: Total Contact Forces experienced by carpal bones at the Radiocarpal Joint (Standard deviation approximated from publication)

	Extension		Neutral		Flexion	
	Intact	PRC	Intact	PRC	Intact	PRC
Cadaver Study	220 N	155 N	190 N	167 N	118 N	174 N
Wrist Model	341 N	244 N	222 N	200 N	164 N	145 N
Percent Difference	+55%	+57%	+17%	+21%	+40%	-17%

Table 5.4-1: Total contact forces at Radiocarpal Joint with Percent Difference

The differences observed in the predicted contact forces may be attributed to a number of different factors. Within the research community, it is well known that experimental contact force measurements can be fraught with error due to the method of measurement or the manner in which it is calculated. External force artifacts are very easily captured and cannot be distinguished from the remaining results. In addition to that, the study's publication did not report in enough detail all the testing methods and results. Finally, the high standard deviation indicates high variation within the experimental results itself. In addition to that, contact forces are usually very hard to replicate in a model. Different modeling softwares measure this parameter in different manners and further analysis of this aspect needs to be conducted to determine whether such experimental and modeled results can be directly compared.

A comparison of the percent force transmission through the scaphoid and lunate in the intact wrist was conducted (Figure5.4-10 – Figure 5.4-11). Again, similar trends in percent transmission were replicated to provide an overall understanding of how force transmission occurred through the joint. However, since the model predicted additional force transmitted through the triquetrum, these values were included to provide an adjusted lunate force value (Figure 5.4-10) such that an overall understanding of the total force transmitted was captured relative to the medial or lateral aspect of the carpus.

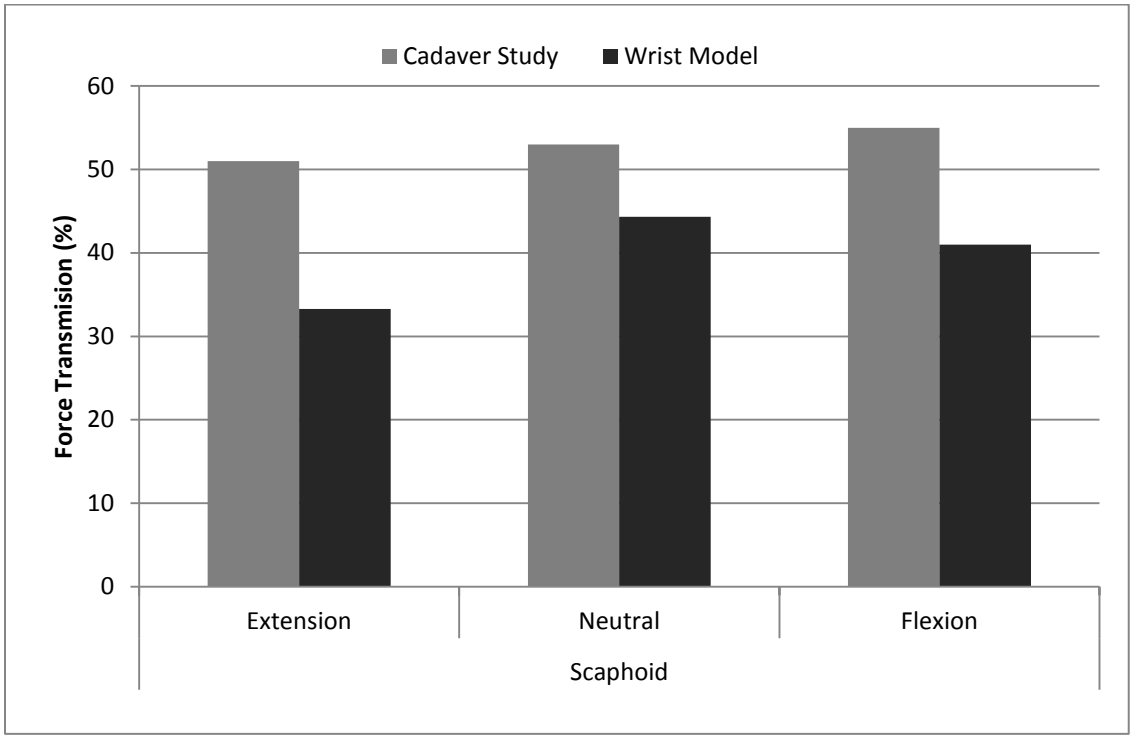

Figure 5.4-10: Percent force transmission through scaphoid in intact wrist

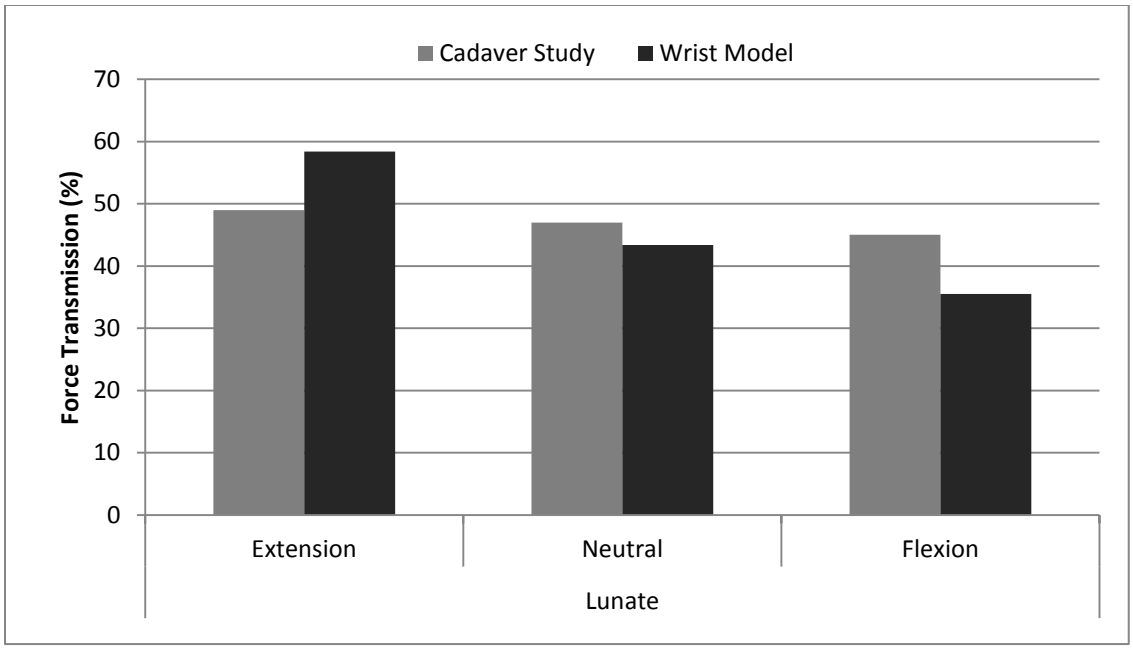

Figure 5.4-11: Percent force transmission through lunate in intact wrist

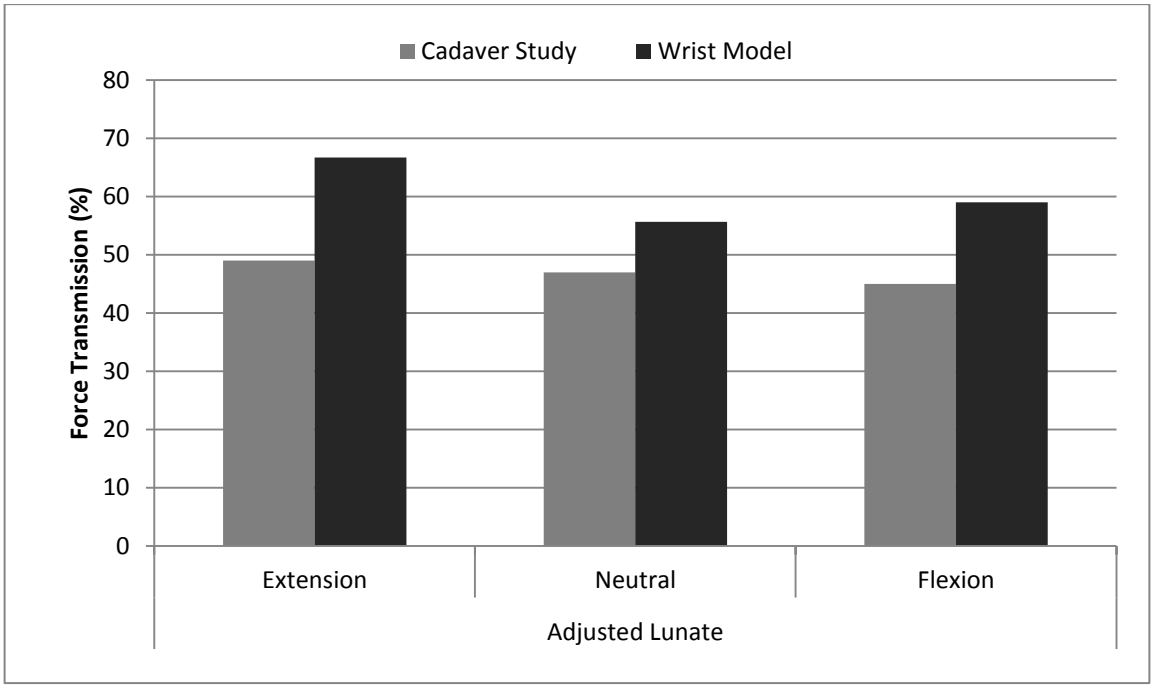

Figure 5.4-12: Percent force transmission through lunate (adjusted to include forces detected in triquetrum) in intact wrist

CHAPTER 6: DISCUSSION

Through the course of this thesis, a three-dimensional (3D) rigid body wrist model was developed to accurately replicate the function and response of the human wrist joint. The 3D wrist model was developed as described in Chapter 3 and validated against three different cadaveric experimental studies discussed in Chapters 4 and 5. The experiments examined the biomechanical changes observed in intact and surgically altered wrist joints. These studies were replicated within SolidWorks and analyzed to demonstrate accuracy and its possible use as a powerful predictive tool to determine wrist behavior.

The 3D wrist model developed during this work was based on the model developed by Majors et al. For purpose of clarity during this discussion, the previous version of the wrist model will be referred to as the Majors' wrist model and the current version will be referred to as the 3D wrist model. The method of modeling and representing the bones, ligaments and tendons of the wrist were carried out in a very similar manner in both versions of the model. The method of modeling for both these versions are unique compared with existing computational wrist joint models reported within the literature. In the two computational wrist models, the function and response of the joints were solely dependent on the 3D anatomy of the bony articular surfaces, the ligaments and other soft tissue restraints and were directed by muscular forces or other external perturbations. Accurate renditions of the bony articular surfaces were recreated within the model design space to replicate the joint's physiological range of motion. Joint motion was not restricted to predefined paths or planes but instead responded in a geometry and restraint based forward dynamic manner.

Majors' wrist model replicated the right human hand while the 3D wrist model represented the left human hand. Further, the 3D wrist model included additional soft tissue structures, like the triangular fibrocartilage complex (TFCC) and capsular retinacular structures that were not included in the previous version of the model. A detailed description of the method of formulation and implementation of these additional soft tissue structures has been discussed in Chapter 3.

The 3D wrist model was first validated against a cadaveric experimental study conducted by Pervaiz et al which tested range of motion of the wrist joint in the normal state, and following radioscapholunate (RSL) fusion, distal scaphoidectomy and triquetrectomy surgical procedures. The Majors' wrist model replicated this study in its entirety, with comparably good results. To validate the 3D wrist model developed during the span of this work and to show reproducibility of the results obtained between the two versions of the models, part of the RSL fusion experimental study was simulated in the current version.

The 3D wrist model accurately replicated the trends observed during the experimental study, functioned within physiologically reported ranges of joint motion and demonstrated repeatability between the two versions of the computational model. In the intact state, the 3D wrist model was able to accurately predict range of motion angles as reported by the cadaveric study. For the four motions tested, there was less than 5 percent difference in the predicted values for the modeled wrist and the values reported by the Majors' model. All the predicted results were also well within one standard deviation of the experimental study results. In the Majors' wrist model, while most of the angles obtained were well compared, some over prediction was observed for ulnar deviation and flexion. In the 3D wrist model, more accurate prediction capabilities were achieved. The over prediction in the original wrist model was

attributed to the absence of certain soft tissue structures like the TFCC and the capsular structures. Thus with the incorporation of these structures in the 3D wrist model, a more accurate prediction of the wrist joint's response was achieved. In terms of extension and radial deviation, the range of motion angles achieved between the two different models and the experimental study were consistent.

The 3D wrist model predicted a flexion angle of 73^o and an extension angle of 55^o, demonstrating a total flexion-extension arc of 128^o. In the experimental study, flexion of $70^o \pm 7^o$ and extension of $56^o \pm 8^o$ for a total 126^o flexion-extension arc was highly comparable to the predicted value. Similarly, the 3D wrist model's 30^o of radial deviation and 32^o of ulnar deviation predicted a total radio-ulnar motion arc of 62^o. This is also highly comparable to the radio-ulnar arc of 61^o ($30^o \pm 8^o$ radial deviation and $31^o \pm 5^o$ ulnar deviation) reported by the cadaveric study.

In similar cadaveric experimental studies reported within the literature, the work conducted by Berkhout et al [75] reported a total flexion-extension arc of $149^o \pm 19^o$ and radio-ulnar motion arc of $54^o \pm 14^o$ while McCombe et al [76] reported motion arcs of $141^o \pm 9^o$ and $49^o \pm 9^o$, respectively. While the flexion-extension arcs are larger than those predicted by the model, the radio-ulnar motion arc was much more comparable to the predicted results.

The greater difference in the flexion-extension arc may be explained by the various experimental testing methodologies. In the study by Berkhout and colleagues, the wrist specimens were secured and tested in a vertical upward orientation and thus the force of gravity would promote further flexion/extension. Additionally, the study utilized an electromagnetic tracking system which requires the attachment of hardware and can increase the total weight of the specimen. In the work conducted by McCombe and colleagues, instead of applying fixed

specified loads, each specimen was manually moved through the two motion arcs to the approximate end-point of the range of motion. Finally, if the anatomical structure of the radiocarpal joint is analyzed, the bony articular surface prevents motions in the radial and ulnar aspect of the joint. On the other hand, motions in the palmar and dorsal aspect of the wrist are not as restricted by bony articulations but rather controlled by soft tissue structures. Thus, the flexion-extension arc is more likely dependent on the testing methodology and thus greater differences are observed between the studies. This could also explain the consistency observed in radio-ulnar motion arc between studies, even with different test methodologies.

The results obtained from the 3D wrist model with the simulated RSL fusion procedure also resulted in consistent predictions as reported by the Majors' wrist model. Further, the trends of these predicted results correlated well with those observed in the experimental study. However, the accuracy of the predicted angles did not improve as much as it did for the intact normal wrist state. In the RSL fusion state, the 3D wrist model predicted a total flexion-extension arc of 56^o (flexion = 34^o, extension = 22^o) and radio-ulnar motion arc of 35^o (radial = 17^o, ulnar = 18^o). By comparison, the experimental cadaver study reported a RSL flexion-extension arc of 52^o (flexion = $27^o \pm 9^o$, extension = $25^o \pm 10^o$) and radio-ulnar motion arc of 42^o (radial = $20^o \pm 8^o$, ulnar = $22^o \pm 9^o$). As expected, with the simulated fusion of the scaphoid and the lunate bones, global wrist motion decreased significantly. While the 3D wrist model still demonstrated predictions similar to those shown in the Majors' wrist model, all results fell within one standard deviation of the experimental study results. A comparison of the results of the two different models showed some slight differences in motion angles, however this can be attributed to anatomical differences and incorporation of additional soft tissue structures of the wrist joint in the 3D wrist model.

While the cadaveric study and the Majors wrist model carried out additional experiments in two further surgical states, these were not replicated in this work. The 3D wrist model's results demonstrate reproducibility between different models and its ability to accurately predict human wrist motion. The addition of soft tissues like the TFCC and retinacular structures to the current wrist model has greatly improved the accuracy of the results. However, lack of representation of cartilage and other soft tissues that structurally may not be as well understood by researchers at this time may contribute to some of the differences observed between the model and cadaveric experiments.

Following validation of the 3D wrist model against the RSL fusion range of motion study, the experimental study by Blankenhorn et al [33] was replicated. This cadaveric study investigated the changes observed in the wrist joint following a proximal row carpectomy (PRC) procedure. PRC is a motion preserving surgical procedure often employed to treat various degenerative diseases of the wrist proximal carpal bones. PRC is favored by many practitioners due to its ease of performance, lack of non-union formation and early patient recovery. [71], [77] For the short term, the procedure has demonstrated positive results in preservation of wrist motion and grip strength within functional ranges as well as providing pain relief. While there have been concerns over the degenerative effects caused by the significant reduction of joint articulation area, long term results have demonstrated dependability and durability without significant functional deterioration of the articular surfaces. [72], [78]

The experimental protocol was replicated with the 3D wrist model as described in Chapter 5 and separate simulations were performed for each test in the intact normal and surgically altered PRC wrist. The results obtained from the model accurately replicated the motion arcs as well as the changes observed due to PRC (Figure 5.4-1). When comparing the

percent decrease in motion between the intact and PRC wrist, it was found to be fairly accurate for flexion (Model 32 % vs. Experimental 29% ± 2%) and comparable for both radial (Model 40 % vs. Experimental 45% ± 8%) and ulnar deviation (Model 22% vs. Experimental 15% ± 5%). In extension, the model did under predict the percent change showing a 9% decrease in extension following PRC, while the cadaveric study reported a total 36% ± 12%decrease. This difference most likely arises from the method of representation of the soft tissues and the assumptions made during the model's development.

Once a human wrist joint undergoes a PRC procedure, most of the radiocarpal ligaments lose at least one, if not both, skeletal attachment sites. However, these ligaments are not removed from the wrist. While they may not provide their primary stabilizing role, most of these ligaments are still integrated with the surrounding soft and capsular structures. These ligaments continue to help maintain the integrity of these soft tissue structures and may even contribute to their functional role. The only radiocarpal ligament that is left intact is the radiocapitate portion of the RSC ligament. However, due to carpal height shortening, this lone palmar ligament was no longer completely taut and could not provide complete support.

The tissue structure in which these radiocarpal ligaments most likely still play a stabilizing role is within the wrist joint capsule. Anatomically, the ligaments integrate and are confluent throughout the tissue. Thus, healthy ligaments not only play their primary role of stabilizing between their two attachments sites, but also support in a three dimensional manner via the capsule. Even with the elimination of an attachment site, the ligament still can contribute to the overall network that surrounds the carpus.

A PRC procedure is normally conducted through a dorsal excision of the wrist. Upon careful bone extraction, an anatomical repair of the extensor reticulum (ER) is carried out. The dorsal capsule is then overlapped and sutured following which the remaining tissue and skin is sutured closed. [79–81] Since a PRC procedure has shown long term positive functional effects [72], [78], [81] without many of ligaments performing their primary stabilizing role, it can be assumed that the surrounding soft tissue structures enhance their support to the deficient wrist. As described in Chapter 2, the FR and ER are bands that span the palmar and dorsal aspect of the wrist securing most of the wrist and finger muscle tendons and maintaining their anatomically correct lines of action. Testing with the 3D wrist model demonstrated that these capsular retinacular structures were essential in maintaining proper function of the wrist joint, especially in a surgically altered state. However, the role played by the modeled capsular structures are most likely functions performed by not only the FR and ER but also the wrist joint capsule and a combination of other soft tissue structures within the region. Currently, the biomechanical role of all these surrounding soft tissue structures in relation to the carpus is not well understood. In terms of the FR and ER, testing on the joint has demonstrated increased tendon excursion, bowstringing and changes in muscular anatomical lines of action upon excision of these structures. [31], [62] Additional investigations will be required to better understand how this group of soft tissue structures directly affect carpal bone kinematics.

In the clinical study conducted by Cohen et al, [71] an average 62% ± 10% preservation of the flexion –extension arc and 51% ± 18% of the radial-ulnar motion arc was reported after a PRC procedure. Likewise, in the study by Wyrick et al which treated eleven wrist joints with a PRC procedure, [77] the average wrist motion angles were measured to be 85^{o} for the flexion-extension arc and 31^{o} for radial-ulnar motion arc. Overall, the study reported a total 64%

(average of all four motions) retention of the wrist motion arc relative to the contralateral healthy wrist. In the clinical study with a minimum ten year follow-up conducted by Jebson et al, [78] the average flexion-extension arc was reported as 84^o pre-op and 77^o post-op and the average radial-ulnar motion arc was 39^o pre-op and 34^o post-op. The total average range of motion arc was found to be 63% of the contralateral wrist. In another long term follow-up clinical study conducted by DiDonna et al, [72] post-operatively the flexion-extension arc was 72^o and the radial-ulnar motion arc was 40^o, a 61% preservation of the total wrist motion arc. With respect to the computationally predicted results, the 3D wrist model demonstrated a total 74% retention of the total intact healthy wrist motion arc post-operatively.

While the 3D wrist model's predicted value was slightly higher than the clinically reported values, the difference is most likely due to the fact that after a surgical procedure, the patient's tissue undergoes healing and may even form scar tissue. The healed and scar tissue would most likely provide additional restrictions and support to the carpal bones. This would lead to a reduced motion arc experienced by the joint. Additionally, clinical studies reported very small post-operative radial deviation angles such as 4^o,[77] 7^o,[71] and 9^o [72]. These small angles were most likely caused by radial styloid impingement with the trapezium. No significant impingement was observed in the 3D wrist model and hence it resulted in a 15^o radial deviation prediction. This difference would also account for the greater motion arc preservation predicted by the 3D wrist model. Since the Blankenhorn experimental study utilized cadaveric specimens which could not undergo healing, the observed 69% ± 17% total motion arc preservation post-operatively is much more comparable to the total percent preservation predicted by the 3D wrist model.

The final study the 3D wrist model was validated against was the cadaveric study conducted by Tang et al. [34] This experiment investigated the changes in contact biomechanics within the bones across the radiocarpal joint following a PRC procedure. The methodology of the study was replicated within SolidWorks as described in Chapter 5. While the general model used for this study was identical to the models used to replicate the previous two experiments, certain features were suppressed to allow accurate physiological simulation. The capsular retinacular structures were included within the model to provide additional stability to the wrist model during kinematic motion in the PRC state. However, due to the nature of this final test, all four of the retinacular structures had to be suppressed to allow for accurate physiological simulation.

In the human wrist joint, the FR and ER wrap around the carpal bones and other soft tissue structures cupping and imparting a stabilizing force on the structures it encapsulates. The capsular structures were modeled to replicate this function of the FR and ER. They were represented as four solid bodies (two on the palmar aspect and two on the dorsal aspect) tethered to each other and the radial and ulnar styloid process. During modeled wrist motion, the carpal bone structures generate contact force against these solid bodies which in turn interact with the radius and ulna. Thus, in the complete model, contact force transmission occurred through an anatomically incorrect pathway. Any contact pressure results obtained from the model in this state would not be comparable to the results observed in an experimental study. However, upon suppression of the solid body retinacular structures, the PRC wrist was found to be too unstable to accurately replicate any biomechanical analysis. Thus to replicate the experimental test methodology employed by Tang et al, a multistep approach was utilized. First the complete wrist model was used to determine the desired testing positions of the joint. Then the joints were

secured in the desired positions with the incorporation of additional restrictions and reference planes (described in detail in Chapter 5). The solid body capsular structures and distal TFCC were then removed from the design space to reduce the amount of artifact contact force within the system. In this manner, the 3D wrist model was able to determine the contact force transmission through the carpus replicating the cadaveric contact pressure test.

Comparing the results predicted by the 3D wrist model with the experimental results, the overall trend in changes observed in total contact force generation was replicated. When looking at the total contact force measured, there was some significant over prediction in extension for both the intact and PRC wrist (Figure 5.4-9). However, when looking at the percent change in force pre- and post-operatively, the greatest difference was found in the flexion position. Percent changes in bone contact forces predicted by the 3D wrist model were as follows: in extension a 28% decrease (experimental = 30% decrease), in neutral a 10% decrease (experimental = 12% decrease), and in flexion a 9% decrease (experimental = 47% increase). Thus, when looking at percent change between the two wrist states, while the results are fairly accurate for both extension and neutral, the flexed wrist experiences a dramatically different response than predicted. It can also be noted that with the exception of the intact wrist in flexion and extension, all the results fall within one standard deviation of the experimentally reported results. When analyzing the predicted force generated between the individual carpal bones (Figure 5.4-6 – Figure 5.4-8), while the scaphoid and lunate predictions follow the experimental observed trends, the capitate appears to respond experimentally in the PRC state in a different manner than as replicated in the model.

The differences in the contact forces observed can be attributed to a number of different factors. In the experimental study, Fuji pressure film was placed within the radiocarpal joint to

measure the pressure generated between the carpal bones and the radial articulating surface, TFCC and ulna. However, the study only reports contact pressure generated by the scaphoid and lunate in the intact wrist and the capitate of the PRC wrist. The study does not explain if no additional contact was detected at the radioulnar articulating surface or if the additional pressures were disregarded from the results. An example image of the Fuji UltraSuperLow film included in the publication does indicate that additional pressures were detected by bones other than just the scaphoid and lunate. However, this fact is not noted or discussed within the text of the publication.

When the study was replicated with the 3D wrist model, the triquetrum was found to bear some force in all three states in the intact wrist. In the PRC wrist, the hamate was found to experience contact force across the radiocarpal joint. The trapezium and the trapezoid were also found to interact with the radius in certain positions in the PRC wrist. If these additional bony contact forces were ignored by the experimental study, this could account for the general over prediction found with the 3D wrist model.

Experimentally measuring the contact forces generated between bones can be difficult and lead to inaccurate results. While one of the most common methods of measuring contact pressure is with Fuji pressure film, these tend be extremely sensitive and can easily form artifacts. [34] Even after extreme care is taken with a complex joint such as the wrist joint, it most likely undergoes unnatural motions until an equilibrium is reached upon application of tendon forces. These motions would express inaccurate results on the pressure film. This fact could also be noted by the very high standard deviations observed in the experimental results (Figure 5.4-9). Additionally, since the test with each specimen was repeated until three constant

pressure films were obtained, the constant distraction of the carpus may also lead to damage and changes resulting anatomically incorrect responses.

Finally, the differences between the model's predicted and experimental results may also be caused by the method utilized for replicating the study. In the experimental study, each position was achieved by loading the tendons with a combined total load of 200N. During the experimental test, the wrist position was manually maintained to prevent out of plane motion. However, the study does not specify how the wrist position was maintained. In the 3D wrist model, constant wrist position was maintained during tests with artificial planes to secure the joint at the desired angles. Since the wrist joint was repositioned to the desired starting positions, the starting point for most of the soft tissue structures were not in its natural resting length. Thus, time was provided prior to application of loads to allow the carpal bones to reach equilibrium at the manually achieved wrist position. Since the simulation starting point for the model was at a set wrist angle instead of neutral, the carpal bones may have responded differently and attained an anatomically different equilibrium state than that achieved by moving the wrist from neutral to the defined joint angle.

The experimental publication did not explain the specific tendon loads applied during the study. While it defined that a total combined load of 200N was applied to tendons, the specific break up between the tendons was not provided. Additionally, it was unclear whether equal loads were applied in each position pre- and post-op. For the purposes of replicating the experiment, this was assumed to be the case. The specific loads applied to each tendon were selected to reflect the ratio of load applied during the kinematic Range of Motion PRC study. Due to the lack of specific information, this method was determined to be the most logical means

of selecting the tendon loads. Variations in individual tendon load would play a large role in some of the differences observed between the experimental and predicted results.

During the incorporation of the additional soft tissue structures within the 3D wrist model, a number of assumptions and simplifications were made. The TFCC was modeled as a two part structure, each of which was represented as a solid body structure. In actuality, the TFCC is a soft tissue structure which probably experiences significant deformation during wrist motion. However, to replicate the functionality that was desired, the solid body assumption was required. Similarly, to recreate the wrapping stabilizing effect of the capsular retinacular structures, a similar assumption was also required. Currently, it is not definitively clear from the literature whether these two groups of tissue play the role that has been assumed within this model. While the model does indicate that these tissues play a major stabilizing role, especially in the deficient wrist, more research will be needed to validate these assumptions.

Additionally, the manner in which the capsular structures are discussed in this text, it is referred to as primarily the flexor and extensor retinaculum. However the functional wrapping stabilizing role discussed is most likely performed by the combination of the retinacular structures, the wrist joint capsule and other surrounding soft tissue structures. Thus, simply associating the modeled capsular bodies as the FR and ER may not be appropriate. Instead, it is more likely that the capsular bodies incorporated in the 3D wrist model represented the combined function of the FR, ER and the wrist joint capsule.

The 3D wrist model was able to replicate and predict the biomechanical response of the joint following different surgical procedures. It also provided some insight into the functions of the various structures the form the overall joint. The TFCC is a not a well understood tissue

structure. Comparing the motions predicted by the Majors wrist model and the current 3D wrist model, it would indicate that the TFCC does play a major stabilizing role on the ulnar aspect of the wrist. Additionally, when a PRC procedure was replicated on the 3D wrist model, the model failed to come to a solution when the TFCC structures were not included. This was due to lack of ulnar side support and rapid and unstable response of the carpus during this motion. Since the TFCC was a critical aspect in stabilizing the surgically altered wrist, this may indicate that this soft tissue structure plays a much more critical role than currently understood.

A similar observation was made in terms of the capsular retinacular structures. These modeled structures were essential in stabilizing the surgically altered PRC wrist to allow the model to determine a solution. They prevented unnatural wrist joint motion. These modeled structures not only replicated the FR and ER, but also all the muscle tendons, ligaments and other tissue that is compacted around the wrist joint. While a good functional understanding on the stabilizing role this group of tissue cannot be found within the literature, the results observed from this work does indicate that it is significant and may justify further investigations.

CHAPTER 7: CONCLUSION

The 3D wrist model was designed to accurately replicate the skeletal and soft tissue anatomy of the human wrist joint. Motion was dictated solely by the articular surfaces and the restraints provided by ligaments and other soft tissue structures. Muscular force was replicated in an anatomically correct orientation. Some assumptions were required to model the function and role played in stabilization by the TFCC and retinacular structures. The material properties of the ligaments and soft tissues incorporated within the model were based on experimentally measured values which were reported within the literature. Overall, the model was designed to respond to perturbations in a forward dynamic manner: based on articular geometry and the defined constraints.

The model was validated against three experimental cadaveric studies which performed two different surgical procedures of the wrist. Both these procedures are often performed by practitioners to treat various injuries and pathologies of the joint. Overall, the results predicted by the model showed good correlation to experimentally reported results. As a RBM wrist model, it demonstrated excellent accuracy in predicting the global kinematic response of the joint pre- and post-operation. It also provided the ability to measure other parameters that normally would not be possible in a live or cadaveric specimen. The contact force results from the model did not demonstrate very high accuracy as compared to the cadaveric study results. However, these parameters are very difficult to measure experimentally and researchers require more efficient tools and a better understanding of the parameter. The model is able to provide some insight and understanding in carpal contact force changes. These values may be advantageous to

surgeons in understanding the effects of corrective procedures on individual components of the joint.

The model has also provided some deep insight into tissue structures that are not well understood by investigators. Tissue structures such as the TFCC and the capsular retinacular structures require further research and experimentation to obtain a deep understanding of their role in wrist joint function. This model has demonstrated the importance of these structures, especially in a deficient and weakened wrist.

While the model did demonstrate high accuracy in terms of predicting the kinematic response in the cadaveric specimens, the model will require more development prior to it becoming a readily used biomechanical investigation tool. First, further work will be required to validate some of the assumptions made during the development of the model. In addition to that, further validation against population data may be required to determine true outcomes of the joint. Additionally, sensitivity studies may also be useful to determine effects of component level differences on the overall joint response.

With further development, the 3D wrist model could be used as a predictive tool to determine the response of the joint prior to a surgical intervention. Individualized models could be formulated using high resolution scans of a patient's appendage which would allow to account for structural and anatomical variations. While further work needs to be performed to overcome some of the assumptions made during its development, the 3D wrist model is a powerful tool that is capable of allowing us to better understand healthy joints, degenerative changes and help plan for corrective interventions.

LITERATURE CITED

[1] S. D. Carrigan, R. A. Whiteside, D. R. Pichora, and C. F. Small, "Development of a three-dimensional finite element model for carpal load transmission in a static neutral posture," *Ann Biomed Eng*, vol. 31, no. 6, pp. 718–725, Jun. 2003.

[2] M. K. Gíslason, B. Stansfield, and D. H. Nash, "Finite element model creation and stability considerations of complex biological articulation: The human wrist joint," *Med Eng Phys*, vol. 32, no. 5, pp. 523–531, Jun. 2010.

[3] P. Ledoux, D. Lamblin, A. Wuilbaut, and F. Schuind, "A finite-element analysis of Kienbock's disease," *J Hand Surg Eur Vol*, vol. 33, no. 3, pp. 286–291, Jun. 2008.

[4] M. K. Gislason, D. H. Nash, A. Nicol, A. Kanellopoulos, M. Bransby-Zachary, T. Hems, B. Condon, and B. Stansfield, "A three-dimensional finite element model of maximal grip loading in the human wrist," *Proc Inst Mech Eng H*, vol. 223, no. 7, pp. 849–861, Oct. 2009.

[5] D. D. Anderson, B. R. Deshpande, T. E. Daniel, and M. E. Baratz, "A three-dimensional finite element model of the radiocarpal joint: distal radius fracture step-off and stress transfer," *Iowa Orthop J*, vol. 25, pp. 108–117, 2005.

[6] S. Boutroy, B. Van Rietbergen, E. Sornay-Rendu, F. Munoz, M. L. Bouxsein, and P. D. Delmas, "Finite element analysis based on in vivo HR-pQCT images of the distal radius is associated with wrist fracture in postmenopausal women," *J. Bone Miner. Res.*, vol. 23, no. 3, pp. 392–399, Mar. 2008.

[7] M. N. Bajuri, M. R. A. Kadir, M. M. Raman, and T. Kamarul, "Mechanical and functional assessment of the wrist affected by rheumatoid arthritis: A finite element analysis," *Medical engineering & physics*, Jan. 2012.

[8] P. Ledoux, D. Lamblin, and R. Targowski, "Modifications to the mechanical behavior of the wrist after fracture of the scaphoid. Modeling by finite element analysis," *Acta Orthopaedica Belgica*, vol. 67, no. 3, pp. 236–241, 2001.

[9] W. B. Edwards and K. L. Troy, "Simulating distal radius fracture strength using biomechanical tests: a modeling study examining the influence of boundary conditions," *J Biomech Eng*, vol. 133, no. 11, p. 114501, Nov. 2011.

[10] E. Horii, M. Garcia-Elias, A. T. Bishop, W. P. Cooney, R. L. Linscheid, and E. Y. Chao, "Effect on force transmission across the carpus in procedures used to treat Kienböck's disease," *J Hand Surg Am*, vol. 15, no. 3, pp. 393–400, May 1990.

[11] X. Guo, Y. Fan, and Z.-M. Li, "Effects of dividing the transverse carpal ligament on the mechanical behavior of the carpal bones under axial compressive load: a finite element study," *Med Eng Phys*, vol. 31, no. 2, pp. 188–194, Mar. 2009.

[12] Y. C. Fung, *First Course in Continuum Mechanics*, 3rd ed. Prentice Hall, 1993.

[13] I. W. Charlton and G. R. Johnson, "Application of spherical and cylindrical wrapping algorithms in a musculoskeletal model of the upper limb," *J Biomech*, vol. 34, no. 9, pp. 1209–1216, Sep. 2001.

[14] F. C. van der Helm, "Analysis of the kinematic and dynamic behavior of the shoulder mechanism," *J Biomech*, vol. 27, no. 5, pp. 527–550, May 1994.

[15] T. M. Barker, C. Kirtley, and J. Ratanapinunchai, "Calculation of multi-segment rigid body joint dynamics using MATLAB," *Proc Inst Mech Eng H*, vol. 211, no. 6, pp. 483–487, 1997.

[16] J. Wismans, F. Veldpaus, J. Janssen, A. Huson, and P. Struben, "A three-dimensional mathematical model of the knee-joint," *J Biomech*, vol. 13, no. 8, pp. 677–685, 1980.

[17] S. D. Kwak, L. Blankevoort, and G. A. Ateshian, "A Mathematical Formulation for 3D Quasi-Static Multibody Models of Diarthrodial Joints," *Comput Methods Biomech Biomed Engin*, vol. 3, no. 1, pp. 41–64, 2000.

[18] F. Schuind, W. P. Cooney, R. L. Linscheid, K. N. An, and E. Y. Chao, "Force and pressure transmission through the normal wrist. A theoretical two-dimensional study in the posteroanterior plane," *J Biomech*, vol. 28, no. 5, pp. 587–601, May 1995.

[19] K. Manal, X. Lu, M. K. Nieuwenhuis, P. J. M. Helders, and T. S. Buchanan, "Force transmission through the juvenile idiopathic arthritic wrist: a novel approach using a sliding rigid body spring model," *J Biomech*, vol. 35, no. 1, pp. 125–133, Jan. 2002.

[20] N. Iwasaki, E. Genda, P. J. Barrance, A. Minami, K. Kaneda, and E. Y. Chao, "Biomechanical analysis of limited intercarpal fusion for the treatment of Kienböck's disease: a three-dimensional theoretical study," *J. Orthop. Res.*, vol. 16, no. 2, pp. 256–263, Mar. 1998.

[21] E. Genda and E. Horii, "Theoretical stress analysis in wrist joint--neutral position and functional position," *J Hand Surg Br*, vol. 25, no. 3, pp. 292–295, Jun. 2000.

[22] M. Majima, E. Horii, H. Matsuki, H. Hirata, and E. Genda, "Load transmission through the wrist in the extended position," *J Hand Surg Am*, vol. 33, no. 2, pp. 182–188, Feb. 2008.

[23] H. Matsuki, E. Horii, M. Majima, E. Genda, S. Koh, and H. Hirata, "Scaphoid nonunion and distal fragment resection: analysis with three-dimensional rigid body spring model," *Journal of Orthopaedic Science*, vol. 14, no. 2, pp. 144–149, Apr. 2009.

[24] S. Fischli, R. Sellens, M. Beek, and D. Pichora, "Simulation of extension, radial and ulnar deviation of the wrist with a rigid body spring model," *Journal of Biomechanics*, vol. 42, no. 9, pp. 1363–1366, 2009.

[25] M. Kobayashi, R. A. Berger, L. Nagy, R. L. Linscheid, S. Uchiyama, M. Ritt, and K. N. An, "Normal kinematics of carpal bones: a three-dimensional analysis of carpal bone motion relative to the radius," *Journal of Biomechanics*, vol. 30, no. 8, pp. 787–793, 1997.

[26] M. Nanno, W. L. Buford Jr, R. M. Patterson, C. R. Andersen, and S. F. Viegas, "Three-dimensional analysis of the ligamentous attachments of the second through fifth carpometacarpal joints," *Clin Anat*, vol. 20, no. 5, pp. 530–544, Jul. 2007.

[27] T. M. Moojen, J. G. Snel, M. J. Ritt, H. W. Venema, G. J. den Heeten, and K. E. Bos, "Pisiform kinematics in vivo," *J Hand Surg Am*, vol. 26, no. 5, pp. 901–907, Sep. 2001.

[28] T. Pevny, G. M. Rayan, and D. Egle, "Ligamentous and tendinous support of the pisiform, anatomic and biomechanical study," *J Hand Surg Am*, vol. 20, no. 2, pp. 299–304, Mar. 1995.

[29] R. A. Berger, "The ligaments of the wrist. A current overview of anatomy with considerations of their potential functions," *Hand Clin*, vol. 13, no. 1, pp. 63–82, Feb. 1997.

[30] B. J. Majors and J. S. Wayne, "Development and validation of a computational model for investigation of wrist biomechanics," *Ann Biomed Eng*, vol. 39, no. 11, pp. 2807–2815, Nov. 2011.

[31] A. K. Palmer, J. R. Skahen, F. W. Werner, and R. R. Glisson, "The extensor retinaculum of the wrist: an anatomical and biomechanical study," *J Hand Surg Br*, vol. 10, no. 1, pp. 11–16, Feb. 1985.

[32] K. Pervaiz, W. H. Bowers, J. E. Isaacs, J. R. Owen, and J. S. Wayne, "Range of motion effects of distal pole scaphoid excision and triquetral excision after radioscapholunate fusion: a cadaver study," *J Hand Surg Am*, vol. 34, no. 5, pp. 832–837, Jun. 2009.

[33] B. D. Blankenhorn, H. J. Pfaeffle, P. Tang, D. Robertson, J. Imbriglia, and R. J. Goitz, "Carpal kinematics after proximal row carpectomy," *J Hand Surg Am*, vol. 32, no. 1, pp. 37–46, Jan. 2007.

[34] P. Tang, J. Gauvin, M. Muriuki, J. H. Pfaeffle, J. E. Imbriglia, and R. J. Goitz, "Comparison of the 'contact biomechanics' of the intact and proximal row carpectomy wrist," *J Hand Surg Am*, vol. 34, no. 4, pp. 660–670, Apr. 2009.

[35] P. K. Levangie and C. C. Norkin, *Joint Structure and Function : A Comprehensive Analysis*, 5th ed.. Philadelphia: FADavis Co, 2011.

[36] R. A. Berger, "The anatomy of the ligaments of the wrist and distal radioulnar joints," *Clin. Orthop. Relat. Res.*, no. 383, pp. 32–40, Feb. 2001.

[37] K. N. An, R. A. Berger, and W. P. Cooney, *Biomechanics of the Wrist Joint*. New York: Springer-Verlag, 1991.

[38] W. P. Cooney, J. H. Dobyns, and R. L. Li, *The Wrist: Diagnosis and Operative Treatment*, 1st Edition. Mosby, 1998.

[39] F. Schuind, K. N. An, L. Berglund, R. Rey, W. P. Cooney 3rd, R. L. Linscheid, and E. Y. Chao, "The distal radioulnar ligaments: a biomechanical study," *J Hand Surg Am*, vol. 16, no. 6, pp. 1106–1114, Nov. 1991.

[40] A. K. Palmer and F. W. Werner, "The triangular fibrocartilage complex of the wrist--anatomy and function," *J Hand Surg Am*, vol. 6, no. 2, pp. 153–162, Mar. 1981.

[41] S. S. Salman and M. Ullah, "The attachments of the lateral and medial ends of the extensor retinaculum of the human wrist," *Acta Anat (Basel)*, vol. 122, no. 3, pp. 185–186, 1985.

[42] S. E. Logan and M. D. Nowak, "Intrinsic and extrinsic wrist ligaments: biomechanical and functional differences," *ISA Trans*, vol. 27, no. 3, pp. 37–41, 1988.

[43] J. K. Mayfield, R. Johnson, and R. Kilcoyne, "The ligaments of the human wrist and their functional significance," *The Anatomical Record*, vol. 186, no. 3, pp. 417–428, 1976.

[44] J. Taleisnik, "The ligaments of the wrist," *J Hand Surg Am*, vol. 1, no. 2, pp. 110–118, Sep. 1976.

[45] G. A. Buijze, S. A. Lozano-Calderon, S. D. Strackee, L. Blankevoort, and J. B. Jupiter, "Osseous and Ligamentous Scaphoid Anatomy: Part I. A Systematic Literature Review Highlighting Controversies," *The Journal of Hand Surgery*, vol. 36, no. 12, pp. 1926–1935, Dec. 2011.

[46] M. D. Nowalk and S. E. Logan, "Distinguishing biomechanical properties of intrinsic and extrinsic human wrist ligaments," *J Biomech Eng*, vol. 113, no. 1, pp. 85–93, Feb. 1991.

[47] R. A. Berger and W. F. Blair, "The radioscapholunate ligament: a gross and histologic description," *Anat. Rec.*, vol. 210, no. 2, pp. 393–405, Oct. 1984.

[48] J. K. Mayfield and W. J. Williams, "Biomechanical properties of human carpal ligaments," *Orthopaedic Research Society*, pp. 143 – 144.

[49] S. F. Viegas, S. Yamaguchi, N. L. Boyd, and R. M. Patterson, "The dorsal ligaments of the wrist: anatomy, mechanical properties, and function," *J Hand Surg Am*, vol. 24, no. 3, pp. 456–468, May 1999.

[50] M. Benjamin, E. J. Evans, and D. J. Pemberton, "Histological studies on the triangular fibrocartilage complex of the wrist," *J. Anat.*, vol. 172, pp. 59–67, Oct. 1990.

[51] H. J. Chiou, C. Y. Chang, Y. H. Chou, C. C. Hsu, Y. F. Jim, C. M. Tiu, and M. M. Teng, "Triangular fibrocartilage of wrist: presentation on high resolution ultrasonography," *J Ultrasound Med*, vol. 17, no. 1, pp. 41–48, Jan. 1998.

[52] R. L. Linscheid, “Biomechanics of the distal radioulnar joint,” *Clin. Orthop. Relat. Res.*, no. 275, pp. 46–55, Feb. 1992.

[53] R. A. Berger and A. C. Weiss, *Hand Surgery*, 1st Edition. Philadelphia: Lippincott Williams & Wilkins, 2004.

[54] A. C. Rettig, “Athletic Injuries of the Wrist and Hand Part I: Traumatic Injuries of the Wrist,” *Am J Sports Med*, vol. 31, no. 6, pp. 1038–1048, Nov. 2003.

[55] J. B. Tang, J. Ryu, and V. Kish, “The triangular fibrocartilage complex: An important component of the pulley for the ulnar wrist extensor*,” *The Journal of Hand Surgery*, vol. 23, no. 6, pp. 986–991, 1998.

[56] F. Netter, *Atlas of Human Anatomy, Professional Edition*, 5th Edition. Saunders, 2010.

[57] R. O. Nigro, “Anatomy of the flexor retinaculum of the wrist and the flexor carpi radialis tunnel,” *Hand Clin*, vol. 17, no. 1, pp. 61–64, vi, Feb. 2001.

[58] C. Stecco, V. Macchi, L. Lancerotto, C. Tiengo, A. Porzionato, and R. De Caro, “Comparison of transverse carpal ligament and flexor retinaculum terminology for the wrist,” *J Hand Surg Am*, vol. 35, no. 5, pp. 746–753, May 2010.

[59] T. K. Cobb, B. K. Dalley, R. H. Posteraro, and R. C. Lewis, “Anatomy of the flexor retinaculum,” *J Hand Surg Am*, vol. 18, no. 1, pp. 91–99, Jan. 1993.

[60] J. Taleisnik, R. H. Gelberman, B. W. Miller, and R. M. Szabo, “The extensor retinaculum of the wrist,” *J Hand Surg Am*, vol. 9, no. 4, pp. 495–501, Jul. 1984.

[61] M. Garcia-Elias, K. N. An, W. P. Cooney 3rd, R. L. Linscheid, and E. Y. Chao, “Stability of the transverse carpal arch: an experimental study,” *J Hand Surg Am*, vol. 14, no. 2 Pt 1, pp. 277–282, Mar. 1989.

[62] F. K. Fuss and T. F. Wagner, “Biomechanical alterations in the carpal arch and hand muscles after carpal tunnel release: A further approach toward understanding the function of the flexor retinaculum and the cause of postoperative grip weakness,” *Clinical Anatomy*, vol. 9, no. 2, pp. 100–108, 1996.

[63] G. Wu, F. C. T. van der Helm, H. E. J. D. Veeger, M. Makhsous, P. Van Roy, C. Anglin, J. Nagels, A. R. Karduna, K. McQuade, X. Wang, F. W. Werner, and B. Buchholz, “ISB recommendation on definitions of joint coordinate systems of various joints for the reporting of human joint motion--Part II: shoulder, elbow, wrist and hand,” *J Biomech*, vol. 38, no. 5, pp. 981–992, May 2005.

[64] P. C. Bettinger, R. L. Linscheid, R. A. Berger, W. P. Cooney 3rd, and K. N. An, “An anatomic study of the stabilizing ligaments of the trapezium and trapeziometacarpal joint,” *J Hand Surg Am*, vol. 24, no. 4, pp. 786–798, Jul. 1999.

[65] Y. Kijima and S. F. Viegas, “Wrist anatomy and biomechanics,” *J Hand Surg Am*, vol. 34, no. 8, pp. 1555–1563, Oct. 2009.

[66] S. F. Viegas, R. M. Patterson, J. A. Hokanson, and J. Davis, “Wrist anatomy: incidence, distribution, and correlation of anatomic variations, tears, and arthrosis,” *J Hand Surg Am*, vol. 18, no. 3, pp. 463–475, May 1993.

[67] A. M. Agur and A. F. Dalley, *Grant’s Atlas of Anatomy, 12th Edition*, Twelfth. Lippincott Williams & Wilkins, 2008.

[68] J. W. Rohen, E. Lutjen-Drecoll, and C. Yokochi, *Color Atlas of Anatomy: A Photographic Study of the Human Body (Point*, Sixth Edition. Lippincott Williams & Wilkins, 2006.

[69] K. L. Moore and A. M. Agur, *Essential Clinical Anatomy (Point*, Third. Lippincott Williams & Wilkins, 2006.

[70] J. K. Mayfield, “Patterns of injury to carpal ligaments. A spectrum,” *Clin. Orthop. Relat. Res.*, no. 187, pp. 36–42, Aug. 1984.

[71] M. S. Cohen and S. H. Kozin, “Degenerative arthritis of the wrist: proximal row carpectomy versus scaphoid excision and four-corner arthrodesis,” *J Hand Surg Am*, vol. 26, no. 1, pp. 94–104, Jan. 2001.

[72] M. L. DiDonna, T. R. Kiefhaber, and P. J. Stern, “Proximal row carpectomy: study with a minimum of ten years of follow-up,” *J Bone Joint Surg Am*, vol. 86-A, no. 11, pp. 2359–2365, Nov. 2004.

[73] J. E. Imbriglia, A. S. Broudy, W. C. Hagberg, and D. McKernan, “Proximal row carpectomy: clinical evaluation,” *J Hand Surg Am*, vol. 15, no. 3, pp. 426–430, May 1990.

[74] J. Pfaeffle, B. Blankenhorn, K. Stabile, J. Imbriglia, R. Goitz, and D. Robertson, “Development and validation of a computed tomography-based methodology to measure carpal kinematics,” *J Biomech Eng*, vol. 127, no. 3, pp. 541–548, Jun. 2005.

[75] M. J. Berkhout, M. N. Shaw, L. J. Berglund, K. N. An, R. A. Berger, and M. J. P. F. Ritt, “The effect of radioscapholunate fusion on wrist movement and the subsequent effects of distal scaphoidectomy and triquetrectomy,” *J Hand Surg Eur Vol*, vol. 35, no. 9, pp. 740–745, Nov. 2010.

[76] D. McCombe, D. C. . Ireland, and I. McNab, “Distal scaphoid excision after radioscaphoid arthrodesis,” *The Journal of Hand Surgery*, vol. 26, no. 5, pp. 877–882, Sep. 2001.

[77] J. D. Wyrick, P. J. Stern, and T. R. Kiefhaber, “Motion-preserving procedures in the treatment of scapholunate advanced collapse wrist: Proximal row carpectomy versus four-corner arthrodesis,” *The Journal of Hand Surgery*, vol. 20, no. 6, pp. 965–970, Nov. 1995.

[78] P. J. . Jebson, E. P. Hayes, and W. D. Engber, “Proximal row carpectomy: a minimum 10-year follow-up study,” *The Journal of Hand Surgery*, vol. 28, no. 4, pp. 561–569, Jul. 2003.

[79] A. Steenwerckx, L. De Smet, B. Zachee, and G. Fabry, “Proximal Row Carpectomy: An Alternative to Wrist Fusion?,” *Acta Orthopaedica Belgica*, vol. 63, no. 1, pp. 1–7, 1997.

[80] T. T. Stamm, “Excision of the Proximal Row of the Carpus,” *Proc R Soc Med*, vol. 38, no. 2, pp. 74–75, Dec. 1944.

[81] E. O. van Kooten, E. Coster, M. J. M. Segers, and M. J. P. F. Ritt, “Early proximal row carpectomy after severe carpal trauma,” *Injury*, vol. 36, no. 10, pp. 1226–1232, Oct. 2005.

VITA

Afsarul Quddus Mir (Afsar) was born in Brussels, Belgium on June 4th, 1986. He has also lived in Bangladesh, Kenya and has been in the Unites States for the last eleven years. Afsar attended T.C. Williams High School in Alexandria, VA where he excelled in the sciences and mathematics. Following high school graduation in 2005, he enrolled in the School of Engineering at Virginia Commonwealth University (VCU). In 2009, Afsar graduated with a Bachelor of Science in Biomedical Engineering with minors in Physics and Chemistry. Post-graduation, he took some time off to travel and visit family in Bangladesh and work within the Richmond area. With his goal for a graduate level degree, Afsar returned to VCU to obtain a Master of Science in Biomedical Engineering. During this time, he was also introduced to the field of innovation systems and business development through two separate internships at the VCU Tech Transfer Office and at the MeadWestvaco Corporation in Richmond, VA. Following completion of his academic goals, Afsar plans to pursue a career within industry in innovation systems.